

Von der Fakultät für Bauingenieurwesen und Geodesie der Leibniz Universität Hannover genehmigte
Habilitationsschrift

On the computational analysis of microbuckling via mesoscale approaches

Über die numerische Berechnung von Faserbeulen durch Mesoskalenansätze

vorgelegt von

Dipl.-Ing. Dr. techn. **Benedikt Daum**

zur Verleihung der Lehrbefugnis für das Fachgebiet

Nichtlineare Statik

Tag der Einreichung

04.01.2022

Tag der Habilitation

31.08.2022

Kommissionsvorsitzender

Prof. Dr.-Ing. **Peter Schaumann**
Leibniz Universität Hannover

Erstbericht

Prof. Dr.-Ing. **Raimund Rolfes**
Leibniz Universität Hannover

Koreferent

Prof. **Olivier Allix**
ENS Paris-Saclay

Koreferent

Prof. Dr.-Ing. **Philipp Junker**
Leibniz Universität Hannover

Abstract

The present treatise is concerned with the application of numerical models to the prediction of compressive strength and associated phenomena in fiber reinforced polymer matrix composites. This topic has received much attention by the scientific community, and the basic mechanisms at microscopic scale are well understood. Even so, microscale models and theories offer no predictive capability at scales relevant for practical application, and the problem of devising suitable approaches for this purpose is still wide open. The main obstacle in this endeavor is that relevant mechanisms are spread over several length scales, hindering their integration.

To address this challenge, the topic is thoroughly reviewed and mesoscale approaches are identified as an essential stepping stone towards an eventual transfer of fundamental scientific research to engineering application. Subsequently, the mesoscopic approach based on a homogenized representation of the fiber/matrix composite is developed further and its application for the prediction of the aforementioned mechanisms is demonstrated: Random flaws in local fiber alignment are the main source of uncertainty with regard to compressive strength and introduce a dependence of compressive strength on domain size. Methods for the proper representation of these flaws and their effect on compressive strength are considered and extended. Compressive failure in the materials under consideration is caused by shear strain localization and features characteristic width and orientation. To make these phenomena amenable to mesoscale modelling as a homogenized solid, the application of an extended solid theory with additional rotational degrees of freedom is considered. The versatility of the approach is demonstrated by predicting phenomena ranging from very small sizes, i.e. the bandwidth, to large sizes via the predicted scale law for compressive strength. Hence, it is argued that the mesoscale approach provides an excellent platform for further work concerned with component scale applications.

Kurzfassung

Die vorliegende Habilitationsschrift befasst sich mit der numerischen Vorhersage der Druckfestigkeit und verwandter Phänomene in langfaserverstärkten Polymermatrixverbunden. Dieses Thema hat über mehrere Dekaden eine umfangreiche Literatur hervorgebracht und ein weitgehend vollständiges Verständnis der grundlegenden Mechanismen auf Mikroskalenebene erreicht. Ungeachtet dessen bleibt das Forschungsproblem der Versagensvorhersage auf anwendungsrelevanten Skalenebenen ungelöst, und die Entwicklung geeigneter Simulationsmethoden ist noch immer ausständig. Die Hauptschwierigkeit dabei ist der Umstand, dass über verschiedene Skalenebenen verstreute Mechanismen zu einem Gesamtmodell integriert werden müssen.

Das oben beschriebene Forschungsproblem wird hier zunächst durch eine umfangreiche Aufarbeitung und Übersicht über die bestehende Literatur angegangen. In dem Zuge werden Mesoskalenansätze mit einer homogenisierten Beschreibung des Verbundmaterials als geeignet identifiziert. Deren Vorhersagekraft und vielseitige Anwendungsmöglichkeit wird anschließend im Zusammenhang mit mehreren konkreten anwendungsrelevanten Aufgabenstellungen demonstriert: Die Druckfestigkeit einer Einzelschicht ist sehr sensitiv auf geringfügige, zufällig verteilte lokale Abweichungen in der Faserausrichtung von der nominellen 0° -Richtung und ist daher mit erheblicher Unsicherheit behaftet. Durch geeignete Methoden können die statistischen Eigenschaften der Faserfehlausrichtung abgebildet werden und mit einem probabilistischen Simulationsansatz zur Vorhersage der Druckfestigkeitsverteilung eingesetzt werden. Die Druckfestigkeit selbst wird durch das Einsetzen von lokalisierten Schubverformung begrenzt. Diese Schublokalisierung entsteht in einem Band von charakteristischer Orientierung und Breite. Um diesen Vorgang einer Simulation durch einen homogenisierten Mesoskalenansatz zugänglich zu machen, wird eine Regularisierung durch den Einsatz einer erweiterten Kontinuumstheorie vorgenommen. Auf Grundlage der vielseitigen Anwendungsmöglichkeit wird argumentiert, dass homogenisierten Mesoskalenansätze eine geeignete Grundlage für weitergehende Modelle auf Komponentenebene darstellen.

Contents

I. Introduction:	
The problem and its context	4
I.1. Scope and structure	4
I.1.1. Microbuckling as a mode of compressive failure	4
I.1.2. The research question	4
I.1.3. Document structure	5
I.2. Microscale analysis, history and limits	5
I.2.1. Microscale	5
I.2.2. 0d-analysis, size $\approx 1d_f$	6
I.2.3. 3d models, size $\approx 1d_f$	6
I.2.4. 1d-models, size $\approx 10d_f$	7
I.2.5. 2d/3d-models, size $\approx 10d_f$	7
I.3. Beyond microscale, misalignment topologies	8
I.3.1. Misalignment measurements	8
I.3.2. Misalignment topology, mesoscale	8
I.3.3. Statistically informed microscale models	9
I.3.4. The sampling point problem	10
I.3.5. The spectral representation method	10
I.4. Mesoscale analysis, efficient and versatile	14
I.4.1. Material models at mesoscale	14
I.4.2. Regularization in the softening regime	15
I.4.3. Stochastic analysis, size effects	16
I.5. Motivation	16
I.5.1. Versatility	16
I.5.2. Overarching objective	17
II. Article:	
A review of computational modelling approaches to compressive failure in laminates	18
III. Article:	
A numerical investigation of the statistical size-effect in non-crimp fabric laminates under homogeneous compressive loads	36
IV. Article:	
A micropolar approach to microbuckling problems in unidirectionally reinforced polymer composites	56
V. Conclusion:	
Towards component scale, an outlook	71
V.1. Measurement and image processing techniques	71
V.2. Surrogate modelling	73
Bibliography of Chapters I and V	75

Chapter I.

The problem and its context

I.1. Scope and structure

I.1.1. Microbuckling as a mode of compressive failure

The longitudinal compressive strength of a wide class of anisotropic materials is in many situations limited by internal buckling and subsequent strain localization. Glass or carbon long fiber reinforced polymer matrix materials with unidirectional or non-crimp-fabric fiber architecture are of particular interest in this work, but similar phenomena can be observed in carbon or metal matrix composites and even in some natural materials like wood. The terminology used in the literature to refer to this phenomenon is somewhat inconsistent, and the names *microbuckling* or *fiber kinking* are sometimes used interchangeably and sometimes with a more narrow definition assigned to one or the other. To avoid confusion, the term *microbuckling*, abbreviated by MB, is used here almost universally, with a few exceptions when discussing the literature, see the discussion of *kinking*- vs. *bending*-theories in Chapter II, Sec. 2.2, paragraph 6 further down. MB is one of many distinct and competing failure mechanisms in the considered class of materials, and which mode takes precedence depends on material properties and loading conditions [Piggott, 1981]. Other notable failure mechanisms include fiber crushing and longitudinal splitting, see Ref. [Fleck, 1997], Fig. 9 for a diagram associating different failure modes with regions in a material parameter space. A more detailed discussion of failure modes is provided in Chapter II, Sec. 2.1, at this point it suffices to state that MB is the most prevalent failure mechanism in a wide range of materials and loading conditions and is the most relevant compressive failure mode in many engineering applications. Contrary to what the name *microbuckling* might suggest, the phenomenon arises not from a bifurcation of equilibrium, but rather from a limit load problem resulting from locally imperfect fiber alignment and shear nonlinearity, an extensive discussion of the basic mechanism is included further down in Chapter II, Sec. 2.2. Nevertheless, MB shares some traits with shell buckling, i.e. the macroscopic response of a homogeneously loaded coupon is essentially linear until failure and strength is very sensitive to small imperfections. This imperfection sensitivity causes a large scatter of results in physical compression tests on coupon shaped specimens. It is almost universally accepted, that fiber strength is insignificant for MB and is associated with a separate fiber crushing failure mechanism instead, see Chapter II, Sec. 4.3, paragraph 2. As a result, compressive strength may be less than 60% of the corresponding tensile strength in unidirectional carbon-epoxy laminates [Budiansky and Fleck, 1993, Fleck, 1997].

I.1.2. The research question

Theories and models regarding the onset and progression of compressive failure in long fiber reinforced materials are a long-standing research subject that has received substantial attention of the research community in the past and continues to do so in the present. Over several decades this effort rendered profound insights into many aspects of the problem, and in some regards the basic theory of MB may be considered mature. However, despite significant progress in the understanding of the basic principles, most existing approaches remain limited in scope and are tailored to specific purposes and/or are subject to limitations that render them unsuitable to reliably predict the outcome of a physical test. Among the main causes for the intractability of the problem is the strong sensitivity of the response to minute

imperfections in the local alignment of the fiber reinforcement. Further relevant mechanisms are spread over several length scales, all much smaller than the macroscopic size of a coupon or engineering component. Hence, though most aspects of the problem are well understood in isolation, their interaction is often not. Moreover, the integration of the relevant aspects over their respective length scales into a sufficiently general simulation approach suitable to the prediction of the initiation and evolution of compressive failure in typical composite components is still open. The present work is motivated by this lack of predictive capability at scales relevant to engineering application, and aims to address it by extending the integration and consolidation of relevant mechanisms. The intent is to overcome the difficulties that have been hinted at above, and to contribute towards a more general approach to the problem. The remainder of Chapter I will provide a profound motivation for the application of modelling approaches based on a mesoscopic scale, i.e. in between the scales defined by the microstructure and the macroscopic component.

I.1.3. Document structure

Survey and interpretation of the substantial body of knowledge that has been accumulated by the research community of about five decades is not a trivial endeavor. Hence, the purpose of this brief introductory survey here is limited to the substantiation of the claims made in Subsec. I.1.2, scope and structure are set accordingly. An extensive discussion of the literature is not intended here in Chapter I and a comprehensive literature survey is deferred to Chapter II. In this spirit, an overview of the main developments in the field is exposed here in a structure that lends itself to provide a consistent line of argumentation that conveys the motivation for mesoscale approaches in general, and this work in particular. In contrast, the review in Chapter II takes a more general standpoint and covers also the wider scope of the problem. The versatility of the mesoscale approach is utilized in Chapter III to predict MB-strength, and in Chapter IV to predict band morphology. It is hoped that this effort will eventually fulfill the long term goal of reliably predicting component strength via a computational model derived from the extensive theory on the subject. Prospective concepts to this end are discussed in Chapter V.

As a starting point, Sec. I.2 briefly summarizes the merits and limitations of the vast amount of literature concerned with microscale modelling. A definition of this, and other scales, will be given further down. Subsequently, it will be argued that the main benefit of the mesoscale approach is the proper representation given to the fiber misalignment, and prior work relevant to the characterization of misalignment is reviewed in Sec. I.3. At the end of this introductory chapter, advantages and challenges of mesoscale models are discussed in Sec. I.4 and the research question formulated in Subsec. I.1.2 will be revisited in Sec. I.5 for an informed discussion of the motivation of this work.

I.2. Microscale analysis, history and limits

I.2.1. Microscale

As will be elaborated below, many prior approaches to the subject consider a spatial domain that is pertinently defined in terms of the fiber diameter as an intrinsic length scale. For convenience, the symbol d_f shall denote the fiber diameter, typical sizes are between $\approx 5 \mu\text{m}$ (carbon) and $\approx 20 \mu\text{m}$ (glass), and the attribute *microscale* is assigned to approaches covering domain sizes on the order of ≈ 1 to ≈ 10 times d_f . To structure the survey, microscale approaches are further classified into categories based on the dimensionality and extent of the domain they consider. Further down, it will be argued that microscale analysis is not well suited to address the research question formulated in Subsec. I.1.2. Nevertheless, a brief discussion of this approach seems necessary in order to point out key differences to mesoscale approaches. Moreover, theoretical and computational approaches at microscale are the most common kind in the literature.

1.2.2. 0d-analysis, size $\approx 1d_f$

The historically oldest theories [Rosen, 1965, Schuerch, 1966, Argon, 1972] on the subject considered compressive failure of long fiber reinforced composites via an internal instability of a material point. Such 0d-approaches are sometimes referred to as *kinking*-theory models. The point-domain lacks any structure and implies uniformity of parameters and displacements in all directions, therefore, it may seem debatable to which length scale such approaches might refer. However, the assumed uniformity is consistent with the notion that the material point represents only one elementary cell of the fiber/matrix-microstructure with a spatial extent much smaller than the distance over which a gradient in parameters or displacement might become noticeable. Thus, approaches of this category may be considered to refer to a size on the order of $1 d_f$ and, hence, they are classified as microscale approaches here.

The first attempts to explain the compressive strength of long fiber reinforced composites were based on the application of a theory for elastic instabilities in an anisotropic material point put forward by B. W. Rosen [Rosen, 1965]. For composites with a fiber volume content of about 50% or more, the theory predicts the elastic bifurcation of stiff reinforcements perfectly aligned with the loading direction at a compressive load equal to the elastic matrix shear modulus. However, it was soon realized that for polymer matrix composites this approach overestimates strength by about a factor of 4 [Budiansky and Fleck, 1993, Naik and Kumar, 1999] and the elastic instability is preempted by a different failure mechanism. Subsequent theories [Argon, 1972, Evans and Adler, 1978, Budiansky, 1983, Budiansky and Fleck, 1993] accounted for the effect of initial misalignment of the direction of compression to the principal direction of the reinforcement, and the effect of nonlinear matrix stiffness. Equilibrium considerations rendered relatively simple analytical expressions for a critical far field stress that will initiate unstable rotation of the local fiber direction, given some initial misaligned value of the fiber direction and the nonlinear matrix shear response. More modern approaches of this category [Jensen and Christoffersen, 1997, Niu and Talreja, 2000, Basu et al., 2006, Wadee et al., 2012] are typically concerned with more complex constitutive models, complex load states, and details of the unstable response. Both the elastic and the refined models predict a salient characteristic of MB induced compressive failure, that is, an essentially linear stress/strain relation in the pre-failure regime that is terminated by a subsequent regime of sudden softening due to local rotation of the fiber direction. However, only the models accounting for the imperfect fiber alignment and matrix nonlinearity predict plausible strength levels. Moreover, only these models are consistent to the large scatter of strength observed in experiments, due to their strong sensibility to the initial misalignment angle. Thus, only the latter class of theories, e.g. Ref. [Budiansky and Fleck, 1993], pertains to MB as defined in Subsec. 1.1.1.

A significant finding resulting from these theories is that they clearly identify fiber misalignment and matrix nonlinearity as essential ingredients of any accurate model of MB. As a tool to predict compressive strength against MB, however, they are ill-suited due to the simplicity in the representation of the fiber misalignment. In this class of approaches one particular material point is considered without regard for its environment, thus, the misalignment is quantified in terms of a single local misalignment angle. It will be argued further down in Sec. 1.3 that proper account must be given to the random fluctuation of preexisting alignment imperfections over a finite domain. A more in depth review of approaches based on the equilibrium analysis of material points is included in Chapter II, Sec. 2.2.

1.2.3. 3d models, size $\approx 1d_f$

Closed form analysis is possible only on the basis of simplifying assumptions regarding the microstructural kinematics, typically based on the classical Voigt/Reuss assumptions. To overcome this limitation, several investigations [Balacó De Morais, 1996, Bednarczyk et al., 2014, Skovsgaard and Jensen, 2018b, Camarena et al., 2021] regarded a fully 3d micromechanical representation where fiber and matrix are resolved as separate solids. Hexagonal or quadratic periodic fiber packing is typically assumed, since the domain covers only an elementary cell of the composite. Similar to 0d-theories, fiber misalignment is assumed to be uniform within this domain. Hence, this class of approach may be considered as an extension of the closed form analysis theory discussed above, where the numerical framework allows

for a more accurate representation of the microstructure and more complex constitutive models. This results in an improved qualitative assessment of the effect of the microstructure and complex constitutive relations for fiber matrix and interface. However, the representation of the misalignment is still the same and this class of approach offers little benefit with regard to the prediction of compressive strength at coupon or component size.

1.2.4. 1d-models, size $\approx 10d_f$

Another distinct class of approaches accounts for gradients only along the longitudinal direction by representing the fiber as a beam bedded on a foundation formed by the matrix [Xu and Reifsnider, 1993, Schapery, 1995, Fleck et al., 1995, Feld et al., 2011]. The assumption of uniformity in transversal direction is occasionally called the *infinite band* assumption and is inherent to this class. This class of investigations was typically motivated by questions regarding the band morphology, rather than strength considerations, and with few exceptions [Feld et al., 2011], no consideration is given to the statistical nature of the misalignment. The typical longitudinal extent of such models is on the order of a few tens of d_f and chosen so that the width of the band is covered. Bandwidth and orientation are governed by mechanisms known as *band broadening* and *lock-up* resulting from the condition of near incompressibility and kinematic considerations, see Chapter II, Sec. 2.3. Inclusion of a fiber fracture condition allows for the prediction of the *post-mortem* bandwidth, see Chapter II, Sec. 2.4. An important finding that was derived from this class is that fiber bending stiffness has little effect on MB-strength for typical fiber undulations [Fleck et al., 1995].

1.2.5. 2d/3d-models, size $\approx 10d_f$

The final category of microscale models again considers a micromechanical discretization of fiber and matrix, but over a larger domain size. Discretization size is bound to some fraction of d_f , hence, such an approach becomes computationally inefficient at domain sizes approaching about 100 d_f . As a consequence, 2d-models tend to be limited to about 100 fibers and somewhat fewer in a 3d model. This allows for the accommodation of some degree of variation for the misalignment within the confinement stipulated by the domain size. Several such approaches considered inhomogeneous misalignments, e.g.: sinusoidal patches of correlated misalignment [Kyriakides et al., 1995, Romanowicz, 2014], eigenmodes [Yerramalli and Waas, 2004], and uncorrelated, individually random fiber misalignments [Varandas et al., 2020]; The infinite band assumption is also frequently adopted in this context, e.g. in Refs. [Pimenta et al., 2009, Wind et al., 2014]. To reduce the computational effort some investigations introduced some additional assumptions, e.g. in Refs. [Gutkin et al., 2010, Skovsgaard and Jensen, 2018a] a 2d-discretization of a single fiber/matrix-stripe was used with the infinite band assumption and periodicity constraints rendering these models similar to the class of 1d-models reviewed in the previous Subsec. 1.2.4. Other approaches simply disregarded the physical fiber diameter size and scaled it up to sizes on the order of the ply thickness [Prabhakar and Waas, 2013, Bishara et al., 2017].

In summary, microscale approaches rendered many useful insights, but they are limited to exemplary layouts of fiber misalignment in a domain of typically less than $100d_f$ in size. It will be discussed in the next Sec. 1.3, that measurements indicate that even in unidirectional plies nearby fibers have similar, i.e. correlated, alignment and the locally predominant alignment changes over a distance of about 200 d_f [Lemanski and Sutcliffe, 2012] to 400 d_f [Fleck and Shu, 1995]. Hence, microscale approaches necessarily struggle to capture even a single region of correlated fiber alignment, and a representative volume element containing several such regions remains out of reach. This is not only due to the excessive numerical effort, but also due to the delicate pre- and post-processing required by the fully resolved fiber/matrix microstructure. The extreme sensitivity of MB-strength on the magnitude and spatial distribution of misalignment, in turn, implies that microscale approaches seem ill-suited for meaningful strength predictions, in general.

1.3. Beyond microscale, misalignment topologies

1.3.1. Misalignment measurements

The previous Subsec. 1.2.5 led to the conclusion that the local fiber misalignment and the nonlinear shear stiffness are of paramount importance for MB-strength. Shear nonlinearity results from a variety of causes including various microscopic mechanisms like: matrix plasticity [Vogler et al., 2001], viscous effects [Hsu et al., 1999], and interface debonding [Camarena et al., 2021]; Microscale models are well suited to represent the interplay of constitutive nonlinearity with the microstructure, but it has been claimed in the previous section that they are not suitable to provide a representative volume element, since the spatial domain is too small to reflect the spatial allocation of fiber misalignment. This assertion is substantiated in this section by the means of a brief review of empirical investigations and a summary of the most essential findings.

Early measurements of fiber misalignment were based on labor-intensive optical microscopy and micrographs [Yurgartis, 1987, Clarke et al., 1995, Paluch, 1996]. These investigations inferred the in-plane or out-of-plane misalignment angle from the semi-major axes of fiber cross-sections observed in micrographs at some plane inclined to the longitudinal, or tracked the variable position of individual fiber cross-sections over several micrographs in subsequent transversal section planes. More recent investigations take advantage of the increasing proliferation of lab-sized x-ray computer tomography apparatus, see e.g. Ref. [Sutcliffe et al., 2012]. The working principle of computer tomography is based on measurement of local density at a given point within a measurement volume, which is subsequently mapped to a gray scale value in a 3d-voxel matrix. The automated processing of digital images obtained from micrographs or tomography in order to extract the local fiber alignment with a high degree of precision has also become a very active field, see e.g. [Kratmann et al., 2009, Wilhelmsson and Asp, 2018] or the numerous contributions referenced in [Safdar et al., 2022b].

1.3.2. Misalignment topology, mesoscale

The empirical knowledge gathered by the investigations cited above in Subsec. 1.3.1 indicates that, despite its random appearance, the magnitude and spatial allocation of misalignment features certain characteristics:

In unidirectional plies, e.g. manufactured from prepregs, fibers are nominally straight, but local deviations from the nominal longitudinal are present as imperfections caused by manufacturing or handling. In longitudinal direction the curvature resulting from these deviations is resisted by the fiber bending stiffness, hence, typical undulation wavelengths fall in between $\approx 200d_f$ and $\approx 400d_f$. Transversally, contact and friction during compaction restrict the magnitude of deviation and enforce a local correlation of nearby fiber (mis-)alignment. The attribute correlated indicates that the misalignment of nearby fibers is not independent, in the statistical sense, but tends to be the similar. A more precise definition of this property will be given further down in Subsec. 1.3.5. The longitudinal and transversal extent of the region of correlated fiber (mis-)alignment are somewhat different, but on the same order of magnitude of about 1 mm [Sutcliffe et al., 2012]. Several of these regions randomly appear in succession, giving the impression of a randomly fluctuating fiber misalignment over a distance of a few mm. This motivates the introduction of a new lengthscale referred to as *mesoscale* to represent features of characteristic lengths on the order of a few 1 mm. The term *misalignment topology* is used here to refer to such a mesoscale domain comprising several correlated regions of misalignment. Graphical depictions of measured misalignment topologies can be found in Ref. [Sutcliffe et al., 2012] and in [Safdar et al., 2022a]. Over much larger distances approaching the component size, the nominal direction itself may be variable due to draping or discontinuous due to ply drops etc.

In materials with a mesoscale fiber architecture, the characteristics of the misalignment topology are somewhat different from unidirectional materials. This applies e.g. to non-crimp fabric materials where rovings are held together by a stitching yarn periodically piercing through the ply plane, see Chapter III, Fig. 1 for an example. There, the local fiber alignment is, in a first order approximation, determined by

periodic roving undulations resulting from the stitching yarn. Random imperfections are superimposed on the inherent roving undulation due to the architecture, thus the magnitude of misalignment and its spatial correlation are stronger than in unidirectional plies. The spatial extent of the correlation is predominantly determined by the mesoscale architecture, e.g. on the order of 10 mm for the material considered in Chapter III. Random deviations in roving alignment result from manufacturing flaws, undefined offsets during lay up, nesting and contact of neighboring plies during compaction, and viscous or capillary forces during infiltration. A limitation of computer tomography is its high cost, and only small volumes can be scanned economically with a sufficient resolution, typically on the order of a few 1 mm. This is sufficient for unidirectional materials, but too small for materials with mesoscale fiber architecture with larger correlation length due to the architecture. Hence, in Ref. [Wilhelmsson et al., 2018] misalignment topologies in various noncrimp fabric materials were measured via micrographs over a length of 20 mm. An alternative low-cost/large-volume measurement approach based on optical imagery of dry fiber material was used in Chapter III. A discussion of this technique is presented in Chapter III, Sec. 2.1.

1.3.3. Statistically informed microscale models

To harness the data obtained from measurements for the purposes of numerical modelling, a mathematical quantification of the random misalignment must be determined first. A quantification in terms of a statistic seems natural, and several investigations provide empirical histograms of the misalignment angle or a fitted statistical distribution [Yurgartis, 1987, Paluch, 1996, Sutcliffe et al., 2012]. The distribution of in-plane and out-of-plane misalignment are similar [Yurgartis, 1987] and approximately normal, although it has been noticed that the tails of the normal distribution are somewhat inconsistent with physical limits to the magnitude of misalignment [Sutcliffe et al., 2012]. In the mean, fiber alignment follows the nominal direction, hence, the distribution of the misalignment is, by definition, centered around zero. Standard deviations of misalignment are small and depend on materials and conditions, e.g. between 0.6° and 1.9° [Yurgartis, 1987, Sutcliffe et al., 2012] for unidirectional carbon fibers.

A shortcoming of statistical distributions is that they merely quantify the frequency of occurrence of a given misalignment angle and do not contain any information regarding its spatial allocation. Hence, the misalignment topology, as defined above, cannot be recovered from a statistical distribution alone, see also Subsec. 1.3.4 below. Nevertheless, with distribution data at hand, it may seem tempting to attempt an integration of the misalignment as a statistical property into micromechanical models or theories. The lack of topology information is of no concern in this case, because misalignment is reduced to a single local fiber angle anyway. To effect such a statistically informed micromechanical theory, two additional assumptions have to be introduced:

The first assumption is the neglect of any interaction between nearby regions of correlated misalignment. In a micromechanical setting, this is necessary because the microscale domain is either a single point or otherwise too small to represent the spatial correlation of fiber misalignment. This disregards the possibility of constructive or destructive interaction of nearby misalignment, i.e. nearby misalignment in the same direction are more detrimental to strength than if they were in opposite directions.

The second simplification in this context is the assumption of a *weakest link*-type behavior, i.e. that the overall MB-strength of a homogeneously stressed panel is limited by the most severe misalignment it contains. The topic will be revisited in Chapter III to evaluate the relation of component strength to component size. The weakest link assumption is common for brittle materials like ceramics, but also applies, to some extent, to compressive failure by MB, since there exist very little capacity for load redistribution once deformation localizes and local softening begins. Localization occurs at the point of least local strength which coincides with the position of the most severe misalignment, i.e. the weakest link of a metaphorical chain.

On the basis of these assumptions, a known statistical distribution of misalignment may be combined with a micromechanical theory to obtain a simple estimate for the MB-strength. A substantial difficulty, however, is the problem of finding a suitable way to estimate the expected maximal magnitude of im-

perfection, i.e. the weakest link, from the known distribution. In [Wilhelmsson et al., 2018] the problem was resolved by defining the 99th-percentile of an empirically determined misalignment distribution as the maximal imperfection. This threshold seems somewhat arbitrary, and for a similar situation contemplated in Chapter III, Sec. 3.1 the 90th-percentile was found to produce acceptable results. Thus, it may be summarized that the approach has merit in its elegant simplicity, but suffers from more (first assumption) or less (second assumption) crude simplifications, and depends on a seemingly arbitrary tuning parameter (the threshold percentile), see also the discussion in Chapter III, Sec. 3.1, last paragraph. As an improvement, it seems particularly worthwhile to overcome the first simplification by choosing an approach based on a length scale that allows the accommodation of an entire misalignment topology. For this purpose a mathematical quantification including spatial information must be found, which will be the topic of Subsec. 1.3.5 further down.

1.3.4. The sampling point problem

As stated before, the statistical distribution alone does not comprise a complete quantification of a realistic misalignment topology. A demonstration of this shortcoming may be obtained from a practical consideration: To generate a 2d-mesh for some numerical model, the local misalignment at the integration points of the mesh may be defined in terms of a m by n matrix $f[k, l]$ specifying the local misalignment angle for a grid of evenly spaced points at positions X_k, Y_l . For clearer notation, indices k, l of matrix components are specified in square brackets, i.e. $f[k, l] \equiv f_{kl}$, and grid point indices are taken from the range $0 \leq k \leq m-1$ and $0 \leq l \leq n-1$. In a naive approach, $f[k, l]$ may be determined by independently drawing random samples from a known statistical distribution. Thus, in a finer mesh more sampling points would be drawn than in a coarse one, hence, the finer mesh is likely to contain more extreme misalignment, see Fig. 1.1 for an example. By accepting the weakest link hypothesis introduced in the previous Subsec. 1.3.3, it follows that the finer meshes are likely to render a lower strength than coarse meshes. This is not the result of a convergence with finer refinements towards a true strength, since in the limit case of an infinitely fine mesh the most extreme misalignment permitted by its statistical distribution is bound to be present, rendering an implausibly low deterministic strength. The procedure of independently sampling the misalignment at each integration point leads to artificially "noisy" misalignment topologies in fine meshes, and a regularization is required to obtain a natural topology independent of the discretization size. In nature, this regularization is provided by the autocorrelation property, i.e. a relation between the distance of two points in the topology to the degree of statistical (in-)dependence of the misalignment angle at the same points. In other words, in natural misalignment topologies there is a minimum distance from one sampling point to the next that must be traversed before the sampling at both points can be performed independently, thus, regularizing the problem. The physical mechanisms enforcing this constraint are lateral contact and fiber bending stiffness, as reviewed above.

1.3.5. The spectral representation method

The concepts of auto- and cross-correlation are common in the analysis of signals and random vibrations [Newland, 2012] and closely related to Fourier analysis. There, the quantities under consideration are 1d-time series representing signals, but the concepts can be generalized to higher dimensional data sets with little difficulty. For discrete data, e.g. pointwise measurements or element-wise properties in a finite element mesh, the discrete Fourier transformation applies. Different conventions for the normalization and the sign in the argument of the exponential function in the discrete Fourier transformation are in use. The variant used here applies normalization on the forward transformation, see (I.1) below. The forward transformation of $f[k, l]$ is $F[r, s] = \mathcal{F}(f[k, l])$, \mathcal{F} and \mathcal{F}^{-1} indicate forward and backward transformations, respectively.

$$F[r, s] = \frac{1}{mn} \sum_{k=0}^{m-1} \sum_{l=0}^{n-1} f[k, l] \exp\left(-2\pi i\left(\frac{rk}{m} + \frac{sl}{n}\right)\right) \quad (\text{I.1})$$

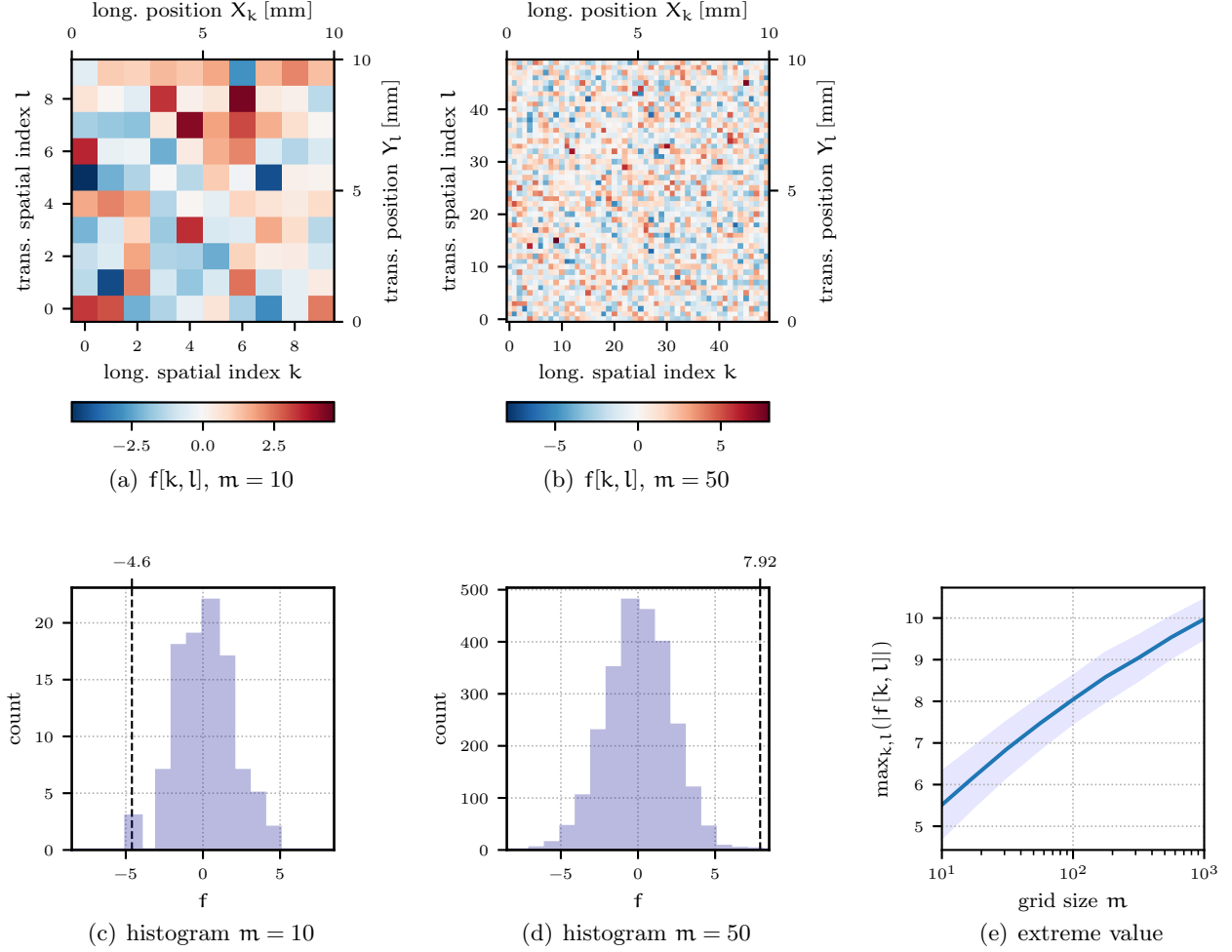


Figure I.1.: A demonstration of the sampling point problem considering a square domain of size $a = b = 10$ mm with variable amount of $m = n$ evenly spaced grid points. The misalignment $f[k, l]$ at each grid point k, l is independently sampled from a normal distribution with zero mean and standard deviation $\text{Std}(f) = 2^\circ$. The top row shows two randomly generated grids of sizes $m = 10$ and $m = 50$, respectively. Directly below are their corresponding histograms. The dashed vertical line in the histograms marks the weakest link, i.e. the maximum misalignment magnitude $\max_{k,l}(f[k, l])$ in the given grid realization. Note that the magnitude of $\max_{k,l}(f[k, l])$ increases with the number of grid points. The lower right log-plot shows how $\max_{k,l}(f[k, l])$ increases with the grid size m in a numerical experiment with 1000 realizations for each grid size. The blue line marks the mean and the shaded band the extent of the standard deviation of $\max_{k,l}(f[k, l])$.

$$f[k, l] = \sum_{r=0}^{m-1} \sum_{s=0}^{n-1} F[r, s] \exp\left(+2\pi i\left(\frac{rk}{m} + \frac{sl}{n}\right)\right) \quad (\text{I.1}_2)$$

Modelling techniques derived from Fourier analysis were first applied to represent misalignment in Ref. [Slaughter and Fleck, 1994] in a 1d-model and subsequently extended to 2d in [Liu et al., 2004]. The same approach was applied in Chapter III and [Safdar et al., 2022a], the essential concepts are briefly outlined here, further details can be found in [Safdar et al., 2020]. The overarching motivation for including this discussion here is to elaborate the need for a sophisticated misalignment representation that is beyond the means of micro-models and will motivate the mesoscale approach introduced in the next Section Sec. I.4.

The misalignment topology of some numerical model may be given in terms of a set of discrete local misalignment angles over a corresponding set of 1d, 2d or 3d-grid points. If the numerical model is intended for unit cell analysis, the misalignment field will be periodic, and this situation is assumed for the sake of the demonstration. If the misalignment was obtained from measurements, the assumption

of periodicity is not appropriate, and some extra precautions must be taken, see e.g. [Newland, 2012]. Moreover, only a 2d-topology shall be considered where a m by n matrix of discrete angle values $f[k, l]$ represents either the in-plane or out-of-plane angle. More sophisticated constellations are conceivable, e.g. a fully 3d-topology embedded in 3d space given in terms of 2 separate data sets for in-plane and out-of-plane angles [Safdar et al., 2022a].

The objective is to overcome the sampling point problem, by finding a technique to generate a matrix of discrete misalignment values $f[k, l]$ of defined standard deviation and auto-correlation. To facilitate the explanation, it is pertinent to start with the desired outcome and to trace the steps that were taken during its creation in reverse. The matrix $f[k, l]$ contains real valued, i.e. $\text{Im}(f[k, l]) = 0$, misalignment angles at evenly spaced spatial position coordinates X_k, Y_l covering a rectangular unit cell of length and width a, b . Because $f[k, l]$ is periodic it can be repeated in a cyclic manner $f[k, l] = f[k - um, l - vn]$ where u, v are positive or negative integers. It is recalled that the mean of $f[k, l]$ is zero, by definition, and this property is exploited in the following without further comment. The example data for $f[k, l]$ shown in Fig. 1.2 features the desired properties and shows some degree of smoothness, i.e. the values f of nearby points tend to be similar, unlike in Fig. 1.1 above. A mathematical quantification of this property is given by the so called auto-correlation matrix $A[k, l]$, see (I.2₁). An alternative more tangible measure for the same is the auto-correlation coefficient $\rho[k, l]$ that contains a normalization by $\text{Var}(f)$, i.e. the variance of the random angle values $f[k, l]$, see (I.2₂). The latter field is plotted in the second row, first column of Fig. 1.2. The absolute value of $\rho[k, l]$ provides a measure for the probability of a point shifted by k, l from the current location having the same magnitude of misalignment. Its sign indicates if the misalignment is expected to be in the same ($\rho > 0$) or opposite ($\rho < 0$) direction. Since there is no shift at the origin $k = l = 0$, $\rho[0, 0]$ is always one. Towards the border of the diagram the shift k, l increases and the auto-correlation coefficient tapers off towards the mean value which is zero.

$$A[k, l] = \frac{1}{mn} \sum_{p=0}^{m-1} \sum_{q=0}^{n-1} f[p, q] f[p + k, q + l] \quad (\text{I.2}_1)$$

$$\rho[k, l] = \frac{A[k, l]}{\text{Var}(f)} \quad (\text{I.2}_2)$$

The forward Fourier transform of the auto-correlation renders the power spectral density $S[r, s] = \mathcal{F}(A[k, l])$ of the field $f[k, l]$. It is defined in frequency domain and $S[r, s]$ quantifies the participation of harmonic frequencies $\omega_r = r \frac{2\pi}{a}, \nu_s = s \frac{2\pi}{b}$ in $f[k, l]$. In the present case it is more convenient, however, to work with a derived property $\tilde{S}[r, s] = \frac{4\pi^2}{ab} S[r, s]$. Inspecting the second row, second column of Fig. 1.2, shows that the power spectral density, or rather $\tilde{S}[r, s]$, has a peculiar form, i.e. it is a combination of rectangular step functions, and is nonzero only for low frequencies. This is by design and ensures the desired properties of $f[k, l]$. By eliminating very high frequency oscillations, the gradient in $f[k, l]$ is limited and the noise in $f[k, l]$ is suppressed. The extent of the rectangular range of nonzero $S[r, s]$ can be used to control the auto-correlation property. The spectral density at the origin $\tilde{S}[0, 0]$ is zero, which results in a zero mean of $f[k, l]$. The functional form of $S[r, s]$ is often assumed as a 1d/2d/3d-step function, but other forms lead to similar results [Liu et al., 2004] and it is not considered of major importance. The spectral density $S[r, s]$ of $f[k, l]$ can also be obtained by an alternative route from the forward discrete Fourier transform $F[r, s] = \mathcal{F}(f[k, l])$, see (I.3) where the superscript asterisk indicates the complex conjugate.

$$\tilde{S}[r, s] = F[r, s] F^*[r, s] \quad (\text{I.3})$$

A proper model generation procedure rendering a defined standard deviation and auto-correlation starts with $\tilde{S}[r, s]$, recovery of $F[r, s]$, and subsequent backward discrete Fourier transform to arrive at $f[k, l]$. Parseval's theorem relates the sum over $\tilde{S}[r, s]$ to the standard deviation of the misalignment angle $f[k, l]$, see (I.4), and can be exploited to adjust the magnitude of the step function to the desired value, e.g. known from measurement. The Fourier coefficients $F[r, s]$ are not uniquely related to $\tilde{S}[r, s]$ since

the latter contains no information regarding the phase angle. However, one particular matrix $F[r, s]$ consistent with $\tilde{S}[r, s]$ can be obtained by randomly sampling phase angles $0 \leq \theta[r, s] < 2\pi$ from a uniform distribution.

$$\text{Var}(f) := \frac{1}{mn} \sum_{k=0}^{m-1} \sum_{l=0}^{n-1} (f[k, l])^2 \stackrel{\text{Parseval}}{=} \sum_{r=0}^{m-1} \sum_{s=0}^{n-1} F[r, s] F^*[r, s] = \sum_{r=0}^{m-1} \sum_{s=0}^{n-1} \tilde{S}[r, s] \quad (\text{I.4})$$

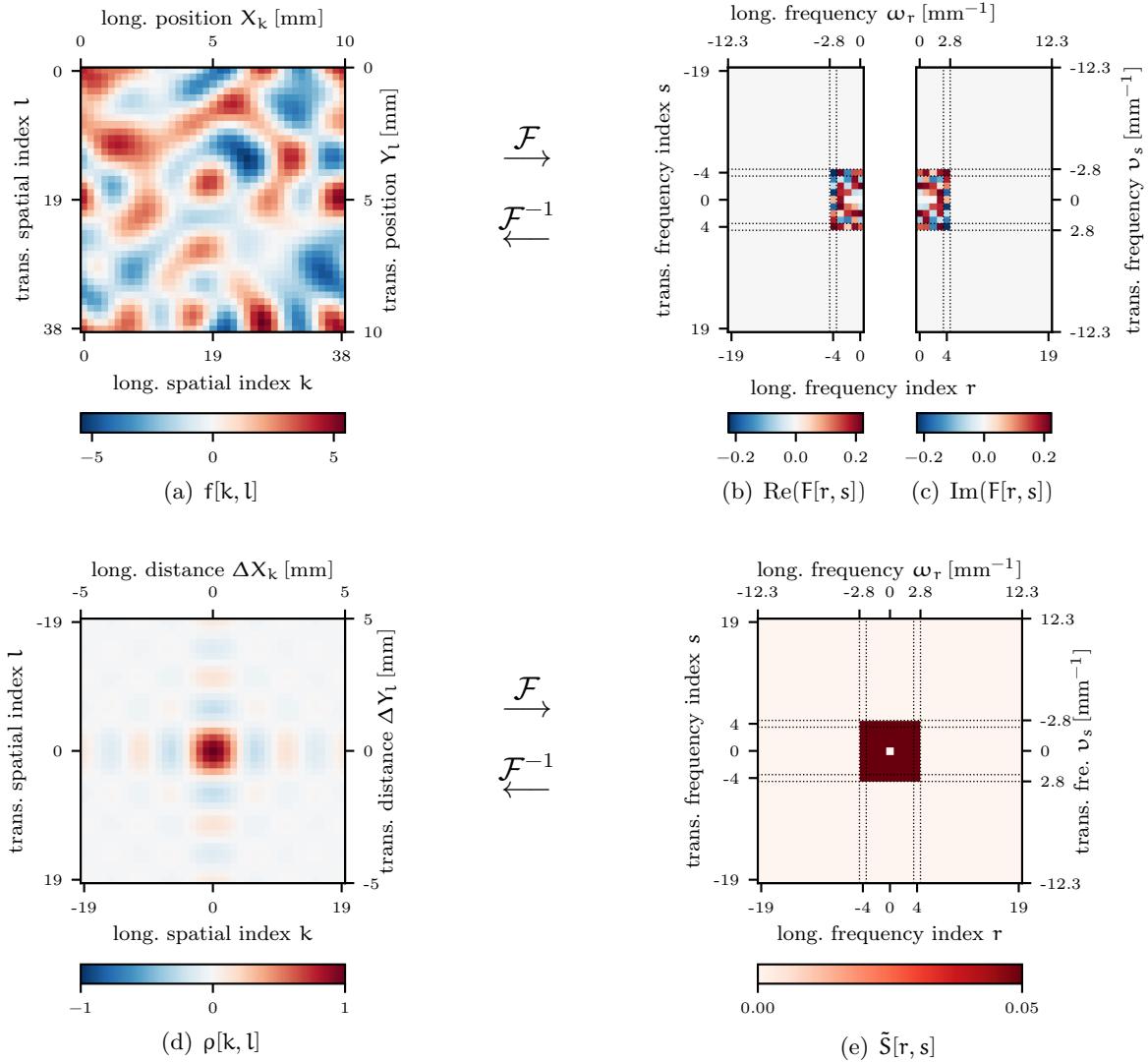


Figure I.2.: The first row shows a discrete misalignment field $f[k, l]$ and its discrete Fourier transformation $F[r, s]$. The auto-correlation coefficient $\rho[k, l]$ and the property $\tilde{S}[r, s]$ are shown in the bottom row. Fields in the left column refer to the spatial domain, while fields shown in the right column are defined in frequency domain. In both rows, the field on the left column is related to the field on the right column via the discrete Fourier transform \mathcal{F} and its inverse \mathcal{F}^{-1} for the reversed direction. In the second row this property does not apply to $\rho[k, l]$, but rather to $A[k, l]$. The matrix $f[k, l]$ represents a periodic field of discrete misalignment angles, e.g. measured in degrees, over a set of $m = 39$ by $n = 39$ grid points over a spatial domain of $a = 100 \mu\text{m}$ by $b = 100 \mu\text{m}$. The standard deviation of all plots is $\text{Std}(f) = 2$. Matrices $\rho[k, l]$, $F[k, l]$ and $S[r, s]$ were shifted so to show index $[0, 0]$ at the center for a clearer representation. Negative indices can be converted to positive ones by adding integer multiples of the matrix size m or n . $F[r, s]$ is complex valued, and obeys $\text{Re}(F[-r, -s]) = \text{Re}(F[r, s])$ and $\text{Im}(F[-r, -s]) = -\text{Im}(F[r, s])$. Matrix elements made redundant by this relation are not shown. The dotted lines outline the last row/column before cutoff.

The procedure is also applicable to non-square domains, either in spatial or frequency domain, see Fig. I.3 for an example. Moreover, the noise pattern shown in Fig. I.1 can be recovered by extending the

step function for $\tilde{S}[r, s]$ over the entire frequency domain, see Fig. 1.4. The resulting field is pointwise independently random and the auto-correlation coefficient is zero everywhere except for $\rho[0, 0] = 1$.

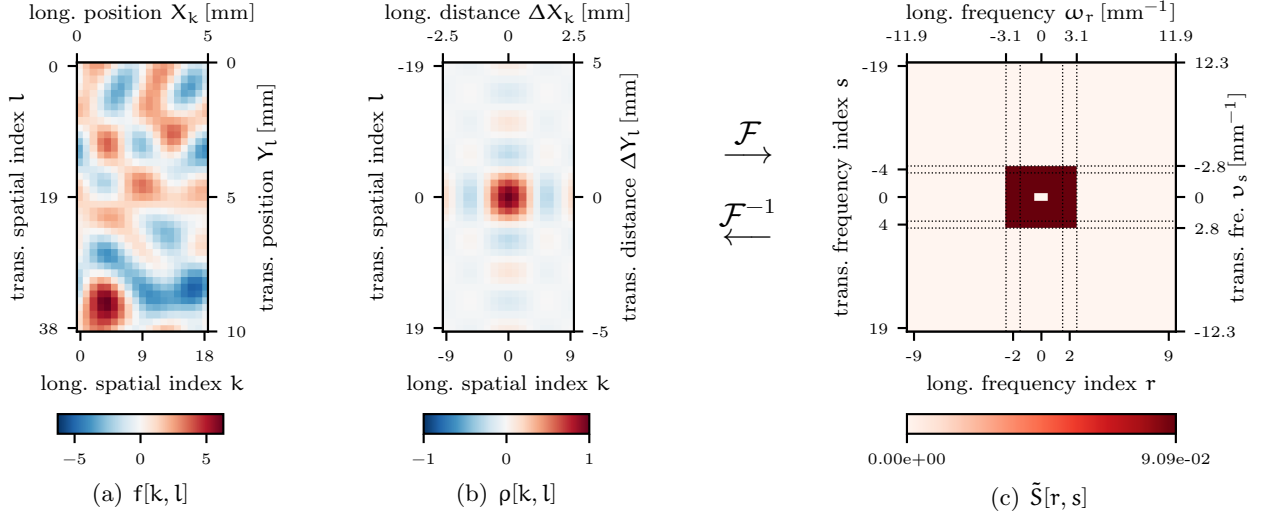


Figure I.3.: A space domain of smaller size with $a = 50 \mu\text{m}$, $b = 100 \mu\text{m}$ and fewer sampling points $m = 19$, $n = 39$. The axis scale in the frequency domain is approximately the same as in Fig. 1.2 above, hence, the width of the matrix columns in $\tilde{S}[r, s]$ is stretched horizontally. The standard deviation of all plots is $\text{Std}(f) = 2$.

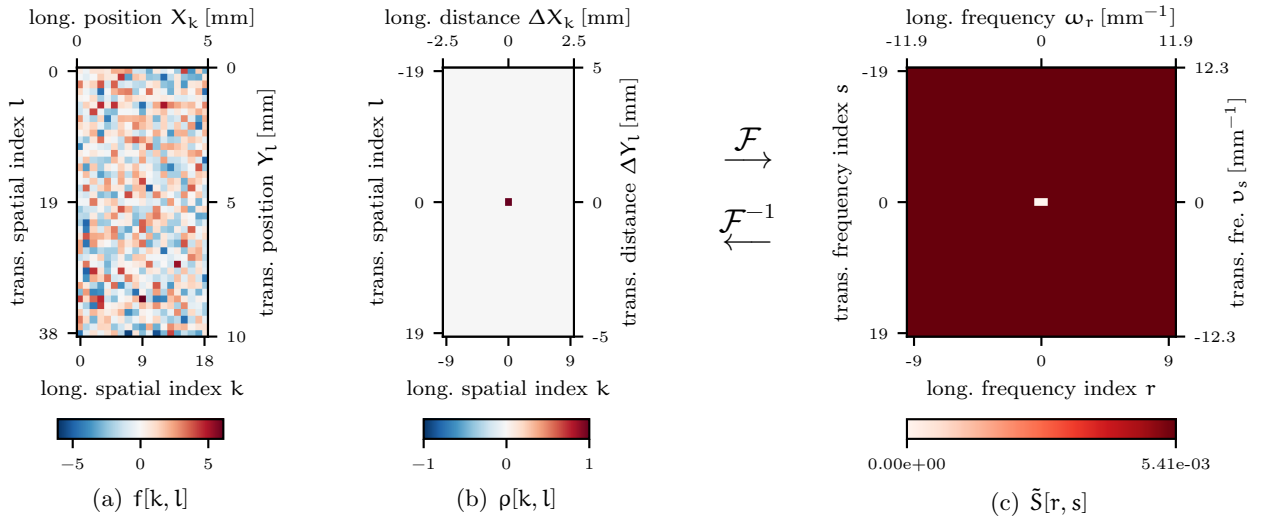


Figure I.4.: The same domain as in Fig. 1.3, but without cutoff in $\tilde{S}[r, s]$. The standard deviation of all plots is $\text{Std}(f) = 2$.

I.4. Mesoscale analysis, efficient and versatile

I.4.1. Material models at mesoscale

In Sec. 1.2 the fiber misalignment was identified as one of the two foremost aspects that determine MB-strength, the other being the shear nonlinearity. While microscale theories clearly indicate that MB-strength is very sensitive to misalignment, they struggle to represent misalignment topology and statistics, recall the discussion in Subsec. 1.3.3. This provides a clear motivation for approaches at a higher, mesoscopic length scale to capture the misalignment topology, and a definition of mesoscale has

already been given in Subsec. 1.3.2. At mesoscale, it is not feasible to resolve the fiber/matrix constituents and their microstructure, so the composite has to be represented via an equivalent anisotropic homogeneous solid. The misalignment field can then be accounted for by applying a small preexisting rotation of the local preferential direction of the material given by a field similar to $f[\mathbf{k}, \mathbf{l}]$, see e.g. Fig. 1.2 or Fig. 7(a) in Chapter III.

With the misalignment accounted for, it is time to shift the attention to the second crucial aspect, the shear nonlinearity. From a microscopic vantage point, shear nonlinearity results from a combination of matrix permanent deformation, cracking, and fiber/matrix-interface debonding, and in a microscale model all of these mechanisms can be represented directly. At mesoscale, the nonlinear effect of these mechanisms must be accounted for indirectly, a very challenging task, in general. However, if the application of the material model is restricted to the simulation of MB until incipient failure, the requirements can be relaxed: In many applications, the effect of transversal direct stress may be neglected, since it is often of small magnitude and has little to no impact on MB-strength. Moreover, MB-strength is to a large extent independent of fiber strength and fiber fracture occurs some time after the initiation of softening, see Chapter II, Sec. 2.4. Hence, it is appropriate to model the material response for longitudinal and transversal direct stress components as linear, if the simulation is to predict only the initiation of softening, and not the full range of the subsequent collapse. The shear nonlinearity, on the other hand, is crucial for MB-strength predictions and must be reflected accurately. However, a substantial simplification results from the observation that if the external load is increased monotonously, the same is true for the shear stress within the band of localized shear deformation. Hence, for monotonic loading to failure it is not necessary to separately account for matrix permanent deformation, cracking, and fiber/matrix-interface debonding via individual state variables, and all of these effects can be covered by one single non-linear mechanism, e.g. via shear plasticity. The shear plasticity model then encapsulates all microscale mechanisms into a single blanket mechanism with one state variable that can be calibrated by an ordinary shear test, where the aforementioned microscale mechanisms may or may not actually occur.

1.4.2. Regularization in the softening regime

The investigation that will be discussed in Chapter III is concerned with MB-strength only, hence the simplifications above are applicable there. Even though strength is probably the most interesting property in practical application, in some situations it may be desirable to extend the simulation beyond the peak compressive load into the softening collapse regime, e.g. in a crash simulation. There are, however, two obstacles associated with this task: The first aspect is that in most situations the model size is significantly larger than the width of the band undergoing softening, and hence the compressive load and the compressive displacements decrease simultaneously for quasi-static loading in the softening regime, see Chapter IV Figs. 9 and 11 for an illustration. Hence, the equilibrium path can only be followed via an arc length scheme, and the actual response in a physical test under load control will be a highly transient dynamic one. Another more profound challenge is that the equations of conventional (Cauchy) solid theory are rendered ill posed in the softening regime, i.e. a shear strain tending to infinity is predicted over a band of width tending to zero. This artefact appears in homogenized models based on conventional solid theory, but not in nature or micromechanical models, since there the bending resistance of the still intact fibers enforces a finite extent of the shear band. Conventionally homogenized approaches lack the notion of local (pointwise) bending and cannot impose any resistance to it. This deficiency can be rectified by applying either a higher order theory accounting for second gradients of displacement or a higher grade theory introducing further unknown variables, see the discussion in Chapter IV, Sec. 2.3. The problem will be addressed in Chapter IV by formulating a material model suitable for MB applications in the context of a Total-Lagrangian *micropolar* (Cosserat) solid theory. The approach presented there overcomes the spurious mesh dependence of conventional solid theory in the softening regime and is able to predict the finite size of the shear band. This and similar approaches [Fleck and Shu, 1995, Hasanyan and Waas, 2018a, Hasanyan and Waas, 2018b] make the analysis of band morphology, e.g. angle and

width, amenable to mesoscale approaches.

1.4.3. Stochastic analysis, size effects

For a given domain size, homogenized mesoscale approaches offer a vast advantage in numerical efficiency over a microscale approach. Due to this numerical efficiency, mesoscale approaches lend themselves well to repeated analysis with stochastic properties, e.g. in a Monte Carlo approach. The most significant source of uncertainty and the main motivation for stochastic analysis is the random misalignment topology. The spectral representation method discussed in Subsec. 1.3.5 allows for easy and robust generation of particular instances of misalignment topologies. The first application of the spectral representation method for a stochastic analysis of MB-strength was presented in Ref. [Slaughter and Fleck, 1994]. That approach considered a 1d-model, however, it differs from the ones discussed in Subsec. 1.2.4 with regard to the considered length scale and the circumstance that a 1d-misalignment topology was considered. Subsequent extensions combined the spectral representation method with a 2d-homogenized approach [Liu et al., 2004]. Other approaches pursued stochastic analysis via a 2d-homogenized medium, but did not employ the spectral representation method [Sutcliffe, 2013]. Instead, they avoided the sampling point problem discussed in Subsec. 1.3.4 by starting with independently sampled misalignment and subsequently applying smoothing filters until the desired auto-correlation properties were attained. Stochastic analysis provides an adequate means to address the scatter in MB-strength, which is a quintessential property of MB and is well documented in experimental observations [Jelf and Fleck, 1994, Schultheisz and Waas, 1996]. Hence, MB-strength is typically quantified in terms of a statistical distribution of strength, rather than a single deterministic value.

Another important insight is that the statistical distribution of strength is subject to a size effect, i.e. average strength diminishes with increasing coupon/component size. This is due to the increase in the expected maximal misalignment flaw in larger domain sizes. Via the weakest link assumption introduced in Subsec. 1.3.3 this leads to an overall reduced strength. This topic will be revisited in Chapter III in more detail, where it will be shown that the weakest link model applies either approximately or not at all, depending on how the coupon/component size is scaled.

1.5. Motivation

1.5.1. Versatility

In the subsequent chapters it will be shown that mesoscale approaches proved to be versatile, and are applicable to predict a variety of phenomena associated with different characteristic lengths, see Table I.1. The literature review in Chapter II, Sec. 2.3 will show that microscale models are often the preferred instrument for the investigation of band morphology, since they offer a direct representation of the microstructure and the constitutive properties of fiber, matrix and interface. As discussed in Subsec. 1.4.1 mesoscale approaches require more abstraction, but also offer much better numerical efficiency. It will be shown in Chapter IV, that mesoscale approaches can capture phenomena associated with the band morphology as well, provided proper regularization in the softening regime is applied. The misalignment topology has been covered in Subsec. 1.3.2 and the topic reappears in Chapter III Misalignment topologies have been so far treated as 2d-in-plane field in the literature [Liu et al., 2004, Sutcliffe, 2013], and a 3d-extension covering in-plane and out-of-plane misalignment is still open. In Chapter III it will be shown that in a 3d volumetric representation of a laminate, another mechanism arises that leads to a substantial mitigation of misalignment severity. Another topic covered in the same chapter are size effects, and the scaling laws required to bridge the gap from meso- to macroscale. In this context, the numerical efficiency of the mesoscale approach is exploited, making it an ideal tool for stochastic investigations.

phenomenon	governing mechanism(s)	characteristic length for mechanism
band morphology	band broadening → II.2.3 , IV.5.2	band width $\approx 20d_f \approx 10^{-1}$ mm
MB-strength at mesoscale	misalignment topology → I.3 , II.3.4 , III.2	char. wavelength in UD $\approx 10^0$ mm char. wavelength in NCF $\approx 10^1$ mm
	laminade mitigation → III.3.2	ply thickness $\approx 10^0$ mm
MB-strength at macroscale	size effect → III.1	coupon size $\approx 10^1$ mm
		component size $\gg 10^1$ mm

Table I.1.: Overview of phenomena and their associated mechanisms and length scales. The listed mechanisms are elaborated further at the specified cross-references. Abbreviations UD and NCF stand for unidirectional and non-crimp fabric, respectively. The numeric values in the third column specify the order of magnitude.

I.5.2. Overarching objective

To conclude the introduction, the research question formulated in Subsec. [1.1.2](#) is recalled. There, the prediction of the response at component scale was formulated as the long term objective in order to transfer results from research to engineering application. The circumstance that essential mechanisms are spread over different length scales was cited as the main obstacle to this endeavor. The subsequent discussion has shown that an approach at mesoscale can account for the essential mechanisms controlling the response, and that results can be transferred to macroscale via suitable scale-laws. This motivates the present work to contemplate mesoscale approaches as a contribution towards this long term objective. The efforts towards this objective presented here are complemented by further investigations performed in cooperation with Safdar et al. [[Safdar et al., 2022b](#), [Safdar et al., 2022a](#)].

Chapter II.

A review of computational modelling approaches to compressive failure in laminates

As apparent from the introduction, compressive failure in general and MB in particular is a wide field, and a comprehensive review of computational approaches to MB is presented in this chapter. This survey establishes an overview of existing work on the subject, and is thus a prerequisite for a meaningful extension of the state of the art. Homogenized models are of the foremost interest in this work, but it is useful to consider the problem within its wider context, hence, the survey is extended to cover microscale, fracture mechanical and multiscale models. Some main characteristics of these complementary approaches were briefly summarized in Sec. 1.2 to motivate the current approach.

This chapter was published as an article and the respective reference is stated below. The first author performed the majority of the survey, worked out the structure and wrote the majority of the manuscript.

B. Daum, N. Feld, O. Allix, and R. Rolfes.

A review of computational modelling approaches to compressive failure in laminates.

Composites Science and Technology, 181:107663, 2019.

<https://doi.org/10.1016/j.compscitech.2019.05.020>



Contents lists available at ScienceDirect

Composites Science and Technology

journal homepage: www.elsevier.com/locate/compscitech

A review of computational modelling approaches to compressive failure in laminates

B. Daum^{a,*}, N. Feld^b, O. Allix^c, R. Rolfes^a^a Institute of Structural Analysis, Leibniz Universität Hannover, Appelstr. 9A, 30167, Hannover, Germany^b Safran Tech / Modeling & Simulation Établissement Paris Saclay, Rue des Jeunes Bois - Châteaufort, 78114, Magny-les-Hameaux, France^c LMT, ENS Paris-Saclay, CNRS, Université Paris-Saclay, 61 av. du Président Wilson, 94235, Cachan, France

ARTICLE INFO

Keywords:

A polymer-matrix composites (PMCs)
 B strength
 B non-linear behaviour
 C computational mechanics
 C modelling

ABSTRACT

Microbuckling is an important failure mode for fibre reinforced composites loaded under compression and the topic has received substantial attention of the research community. This effort led to a good understanding of the basic mechanisms behind the microbuckling phenomenon. However in spite of the well-developed theory, the ability to accurately predict failure loads and other related properties based on available data has not been attained yet. This may be attributed to a number of factors, arising at different scales. Consequently, numerous computational models and methods were put forward in the literature to approach this objective and this survey attempts to provide an overview of these developments. A concise reminder of the phenomenology and theoretical basis is also included to make the present survey self-contained.

1. Motivation and scope

The failure of high volume fraction, continuous fibre reinforced polymer matrix composites under compressive loading is a complex multi-staged process involving many different mechanisms spanning over several scales. This complexity, and the high relevance of the failure mode for many industrial applications, led to a significant research interest in this field over the past five decades. As a result of this effort, most individual theoretical aspects of the problem became well understood by the end of the 20th century and several literature surveys focusing on theoretical and experimental investigations were published in the mid-nineties. Budiansky and Fleck compiled an overview of the theoretical results in Ref. [1]. Piggott [2] reviewed several articles on the effect of fibre waviness on static and fatigue strength. Schultheisz and Waas [3,4] published a popular review on the subject with particular emphasis on experimental techniques; however the state of the art of micromechanical theories at that time is also presented there. Soutis [5] reviewed the compressive strength of fibre reinforced laminates with regard to fracture mechanics approaches. Fleck comprehensively reports the state of the art at the mid-nineties in Ref. [6]. In particular, the work discusses different modes of compressive failure and relates them to certain parameter ranges. Furthermore conditions for kink band propagation are discussed there. Naik and Kumar [7] compared several analytical micromechanical theories to experimental data. More recently, a short review was published by Pinho and coworkers [8].

These past surveys testify that a satisfactory theoretical basis was available for most micromechanical aspects of the problem by the turn of the century. However classical microbuckling theories depend on very specific data at the microscopic scale and are, thus, inapplicable for engineering purposes without further modelling abstractions. For instance, classical theories typically make reference to an *a priori* known misalignment angle, that is often implicitly assumed constant in space. As such, predictions for panels or components based on micromechanical theories are problematic, from a conceptual point of view, since the spatial distribution and the stochastic properties of imperfections are essential. The importance of imperfect fibre alignment was recognized early and investigations into the stochastic properties of its magnitude and distribution were conducted, but its integration into micromechanical theories is computationally very expensive. Further complications arise from the fact that material properties referenced to by micromechanical models are often difficult to obtain experimentally, due to the small length scales and multi-axial loading conditions involved. Notorious examples include the ‘true’ fibre compressive strength, fibre-matrix interfacial strength, interface toughness, and *in situ* inelastic matrix hardening behaviour under multi-axial loads. The fact that, in industrial applications, the relevant mechanisms exist at different length-scales, causes further complications as the scale of the structure under consideration is typically very different from, e.g. the characteristic wavelength of an undulation imperfection.

Any approach aiming at overcoming these limitations inherent to

* Corresponding author.

E-mail address: b.daum@isd.uni-hannover.de (B. Daum).<https://doi.org/10.1016/j.compscitech.2019.05.020>

Received 29 November 2018; Received in revised form 15 May 2019; Accepted 20 May 2019

Available online 23 May 2019

0266-3538/ © 2019 Elsevier Ltd. All rights reserved.

the classical micromechanical theories for microbuckling requires further modelling, typically in a numerical setting. This task received substantial attention from the research community and a vast amount of such *computational models* concerned with the different aspects of microbuckling were put forward. For the sake of clarity, let us define how the term computational model is understood here: For the purposes of this work, a computational model comprises the set of mathematical abstractions of selected physical mechanisms calibrated by reasonably obtainable data, implemented within a numerical solution scheme. A key property of a computational model lies in its extensibility, *i.e.* its ability to predict mechanical responses in situations that differ from the ones used in its calibration. Unlike the theoretical basis, the variety of computational modelling approaches to microbuckling has not yet been comprehensively surveyed.

The motivations and scopes of the approaches surveyed here are diverse. For instance, some models reviewed hereafter aim mostly at understanding the small scale physics and therefore are mostly concerned with the prediction of some local features such as buckling onset or kink-band morphology. Other models however intend predictions of the structural response, particularly for values such as strength and toughness. Also the different aspects of microbuckling and their consequences at higher scales are modelled with varying degrees of complexity, as pertinent for each intended purpose. The resulting diversity of approaches makes the identification of a clear taxonomy of models difficult. Indeed, no unified approach covering every aspect of the problem has emerged, and proper experimental validation of the results is challenging due to the random nature of misalignment. Furthermore, material combinations for which numerical results were obtained are rarely similar, and therefore hardly comparable. Hence, this review does *not* intend to provide a quantitative assessment of the predictive capabilities of the surveyed approaches.

To make this article sufficiently self-contained and to provide reference for sections further down, a very brief summary of the phenomenology and theoretical bases is given in §2. Detailed information about topics discussed briefly or omitted is available in the classical surveys listed above. The survey of recent computational models begins with §3, where semi-analytical micro models extending classical theories by accounting for more general load states, nonlinear kinematics, and more complex constitutive models are discussed. The following §4 reviews explicit micromodels which attempt to achieve a clearer understanding of non-idealized fibre misalignments, edge and notch effects, and small-scale interactions between damage mechanisms, using a distinct resolution of fibres and matrix in a 2D or 3D setting. Finally all approaches bridging the gap between fibre scale and ply scale, either for the prediction of structural quantities or the study of couplings between kinematics or damage mechanisms at different scales, are covered in §5. This survey is concluded in §6 and some directions for open research challenges are proposed.

2. Phenomenology and failure mechanisms

Before reviewing more recent advances, the phenomenology and the classical theoretical basis are presented. The most essential findings on this topic were available by the end of the last century and, for a more in-depth review of the topic, the reader is referred to the literature [6]. Nevertheless, this section provides the motivation and reference for the discussion of the computational approaches presented from §3 onward.

2.1. Failure modes

Continuous fibre reinforced composites typically display a compressive strength that is substantially lower than their tensile strength. Thus resistance against compressive failure is often a critical design criterion. The umbrella term ‘compressive failure’ covers a variety of failure modes that are observed in fibre composites, *cf.* [6] for a

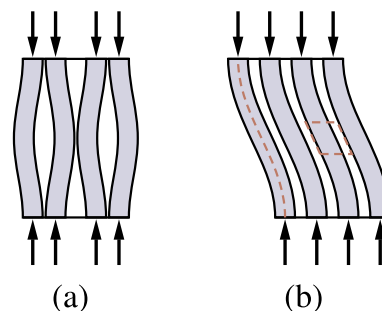


Fig. 1. Fibre buckling modes as considered by Rosen. In (a) the ‘extensional’ or ‘symmetrical’ mode, is only of theoretical interest. In (b) the ‘shear’ mode is shown. The dashed rhomboid outlines the location of the free body diagram assumed in ‘kinking’ theory shown in Fig. 2(a). The dashed sine wave indicates the axis of the beam model used in ‘bending’ theory, see Fig. 2(b).

detailed classification of different modes.

The most common failure mode for stiff fibres embedded in a compliant matrix is known as microbuckling. It can, in principle, occur along two competing modes: with a phase shift of half a wavelength (transverse extensional mode, Fig. 1(a)) or without phase shift (shear mode, Fig. 1(b)) [9]. The extensional mode is typically not relevant for commonly employed high fibre volume fraction composites. Shear mode microbuckling, however, is common and manifests itself as a concentration of inelastic shear deformation in a narrow band, which can be interpreted as a localization of the shear mode. This band of localized shear is oriented at a certain angle which is sensitive to material properties and loading conditions. For a given loading, *e.g.* uniaxial, the band angle is a characteristic of the composite. The occurrence of microbuckling induces a sharp softening in the band, causing an unstable structural response in structures where load redistribution cannot compensate for the decreased stiffness in the band, as *e.g.* in homogeneously loaded, unnotched plates. Under these circumstances strain localizes within the band and strain energy is released by elastic unloading of neighbouring regions. The unloaded volume is typically much larger than the band so that a snap-back-type structural response would be expected under quasi-static conditions. In practice, however, the unstable regime is normally traversed in an instationary, dynamic manner, making the softening phase difficult to observe in experiments. The eventual outcome of the microbuckling process is a narrow band of rotated fibres between two fracture planes: the kink band. In homogeneously loaded plates, the transition from an essentially linear pre-microbuckling response to dynamic collapse occurs suddenly and with a sharp peak in the compressive load-compressive displacement relation.

Although (shear mode) microbuckling is the most prevalent failure mode for commonly employed glass or carbon fibre composites, other failure modes can be observed for particular composites or loading conditions. Failure modes competing with microbuckling in compressed plies are, amongst others, fibre fracture and longitudinal splitting. Piggott [10] observed fibre crushing for strong matrices in combination with weak fibres and longitudinal debonding of fibre and matrix. Oguni and coworkers [11] tested 50% E-glass/vinylester laminates and found a failure mode transition from splitting to microbuckling upon change from uniaxial to multi-axial loading. They also found that splitting in turn can induce microbuckling. At a higher scale, microbuckling and delamination are susceptible to compete or combine, leading to the ultimate failure of a laminated structure, as was reported in *e.g.* Ref. [12]. Lee and coworkers [13] performed a series of experiments on glass and carbon fibre vinyl ester resin composites with different volume contents. In these experiments, it was observed that the glass fibre composites failed due to splitting until a fibre volume fraction of about 30% and a combination of splitting and microbuckling for higher fibre contents. With carbon fibres, no splitting was observed. In the same

work an analysis was presented: Assuming a preexisting microscopic fibre-matrix debonding, the energy release rate for the propagation of a cylindrical debonding was calculated for perfectly straight and misaligned fibres. The resulting model gave predictions in-line with experimental results, *i.e.* predicting splitting for glass fibre composites but not for carbon fibre composites, on account of the much smaller diameter and higher stiffness of the carbon fibres. Yerramalli and coworkers [14] later extended the experimental and analytical investigations to combined compression-torsion loading. Using a special test fixture to induce multi-axial compression, Oguni and coworkers [11] also observed a failure mode transition from splitting to microbuckling under multi-axial compression for 50% E-glass vinylester.

In summary, these investigations showed that, for glass fibre composites of medium to low fibre volume contents and predominantly uniaxial compressive loading, splitting must be taken into account as a possible failure mode in the bulk material. For non homogeneous samples splitting is also frequently observed in carbon fibre composites, but rather as a competing mechanism. Soutis and Fleck have observed splitting as a secondary failure mode accompanying microbuckling in samples with an open hole [15].

2.2. Closed-form peak load prediction

Rosen [9] is usually credited with the first theoretical treatment of microbuckling. He considered the bifurcation from equilibrium of perfectly aligned fibres embedded in an elastic matrix by the transverse extensional or shear modes, as defined above. For the shear mode, this approach estimates peak loads according to (1), where G^m represents the elastic matrix shear modulus and $\hat{\tau}_{11}^\infty$ longitudinal far field compressive stress at peak load.

$$\hat{\tau}_{11}^\infty = G^m \quad (1)$$

Magnitudes predicted by this approach overestimate the peak load by about a factor of 4 [16]. Moreover, its deterministic nature is inconsistent with the large scatter observed in experiments. In subsequent theories, the consideration of initial misalignments and of the nonlinear shear response [17] in the matrix resulted in peak load predictions more closely in line with experimental results. Theories of this kind generally consider the equilibrium of a volume element taken inside a band of shear deformation, under the assumption that it is representative for every location within the band, see Fig. 2(a).

Assuming an initial misalignment of fibres with respect to the direction of applied compression, θ_0 , the compressive stress was related to the matrix shear stress by equilibrium analysis by Argon [18]. Further assuming a rigid-ideal plastic shear response, with yield stress τ_y , and inextensible fibres without bending stiffness, peak loads of reasonable

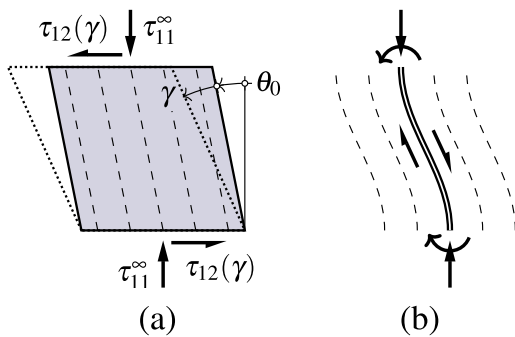


Fig. 2. Closed form analysis considers equilibrium in a deflected state. Nominal fibre direction is vertical, the actual direction is rotated by the (small) initial misalignment angle θ_0 . Further shear deformation due to loading is indicated by γ . The stresses τ_{11}^∞ and $\tau_{12}(\gamma)$ are the compressive far field loading and the shear response, respectively. Sub-figure (a) shows a free-body diagram for a typical ‘kinking’ theory. Bending theory models feature a finite extend in fibre longitudinal direction and a non-zero bending stiffness, see (b).

magnitude are obtained for typical matrix yield strengths and fibre misalignments from (2a). Further refinements of this model were published *e.g.* in Ref. [16], where the effect of the elastic shear response and inelastic hardening were included. The quintessence of this extension is reflected in (2b) with: matrix shear stress $\tau_{12}(\gamma)$ as a function of the shear angle γ , linearized initial misalignment θ_0 , and linearized shear deformation γ . The total fibre rotation is given by the sum of the initial misalignment and matrix shear deformation and max-function indicates maximization with respect to γ . The matrix shear response, $\tau_{12}(\gamma)$, is typically modelled by ideal plasticity or a Ramberg-Osgood plasticity model.

$$\hat{\tau}_{11}^\infty = \frac{\tau_y}{\theta_0} \quad (2a)$$

$$\hat{\tau}_{11}^\infty = \max_{\gamma} \left(\frac{\tau_{12}(\gamma)}{\theta_0 + \gamma} \right) \quad (2b)$$

At peak load $\hat{\tau}_{11}^\infty$, the expression in parentheses attains a maximum and geometrical softening caused by increasing γ can no longer be offset by shear hardening in the matrix, *i.e.* an increase in $\tau_{12}(\gamma)$. In case of a rigid-ideal-plastic shear response, *i.e.* $|\tau_{12}| \leq \tau_y$, (2b) reverts to (2a). In the hypothetical case of very small initial misalignments θ_0 , elastic buckling according to (1) still limits the far field peak stress $\hat{\tau}_{11}^\infty$. Thus, contrary to what the name ‘microbuckling’ might suggest, the phenomenon is not the result of a bifurcation, as assumed by Rosen, but rather the result of a combination of structural and material instabilities driven by the nonlinear matrix response. As a matter of fact, the macroscopic peak load corresponding to a loss of ellipticity in global equilibrium might occur at or after this microscopic instability [19], *i.e.* microbuckling might not cause macroscopic softening if loads can redistribute.

The considerable variation in the peak load observed in experiments is consistent with (2a) and (2b) due to the strong sensitivity of $\hat{\tau}_{11}^\infty$ to the misalignment angle. Variants of (2b) account for the effect of applied in-plane far-field shear stress τ_{12}^∞ by adding it to the numerator. Furthermore, the contribution of transverse stresses to yielding in the matrix can be accounted for by a suitable multiaxial yield criterion. In (2b) and many similar approaches, fibres are assumed to possess infinite stiffness against shortening, thus neglecting the effect of longitudinal matrix stress on matrix nonlinearity.

Even though fibre shortening is usually not considered important, neglecting or considering a finite fibre bending stiffness has been used as a basis to classify theories in two categories. The terms ‘kinking theory’ and ‘bending theory’ are occasionally used to refer to these theories, respectively. The bending-type theory was proposed by Fleck and coworkers, where they accounted for the fibre bending stiffness via an adapted beam theory [20], see Fig. 2(b) for a schematic. Considering the equilibrium of a material element where the fibre and matrix were smeared into a homogeneous composite, the corresponding governing equations were obtained. The consideration of the bending moment transmitted by the fibres introduces the fibre diameter as an intrinsic length scale and gives rise to couple stresses. From further considerations, it was then found that fibre bending stiffness has little effect on the peak stress for typical undulation wavelengths in the millimeter range, but it is still an essential parameter for the kink bandwidth and other properties.

2.3. Kink band morphology

The theories outlined above allow a description of the mechanisms controlling the peak load based on stress components in fibre axial direction alone, *i.e.* longitudinal stress and in-plane shear. The transversal component, although insignificant for the peak load, plays an important role after the kink band is initiated. A common feature of peak load theories surveyed in §2.2 is that the kink band is predicted to initiate perpendicularly to the fibre direction at a band angle of zero.

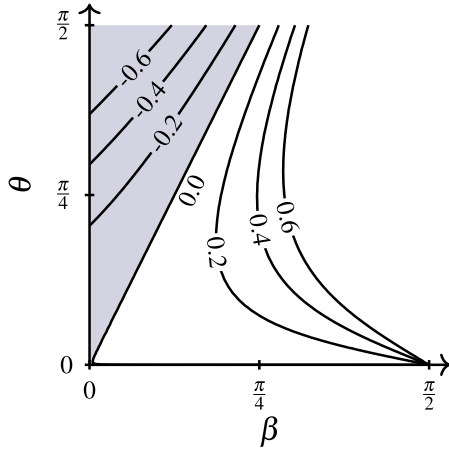


Fig. 3. Contour-plot of ϵ_{vol} over the band angle β and the fibre rotation θ via (3). The shaded area above $\theta = 2\beta$ is essentially blocked off due to volumetric compression.

Attempts to derive a theory with an explicitly non-zero band angle overestimate the peak load [16,21]. This seems to be contradicted by numerous experiments that showed a characteristic band angle in the range of 20° to 30°. See Fig. 4 for the geometric definition of the band angle. A typical experimental observation of the band angle formation is given in Fig. 6 in Ref. [22]. Theory and experiments were reconciled by the observation that the band realigns after initiation to the orientation observed *post-mortem* [23]. The realignment of the band from its initial orientation, perpendicular to the fibres, to the final *kink* band angle occurs in an instationary, dynamic manner during the softening and is, thus, difficult to observe.

Assuming plane strain and inextensible fibres, the volumetric strain ϵ_{vol} is directly equal to the transversal strain. Within a band inclined to the transversal by the band angle β and containing fibres rotated by the fibre rotation angle θ the volumetric (or transversal) strain is given by (3) [24,25] and shown in Fig. 3.

$$\epsilon_{vol} = \frac{\cos(\beta - \theta)}{\cos \beta} - 1 \quad (3)$$

Volumetric dilation can be accommodated by the formation of matrix cracks or voids, but under volumetric compression a very stiff behaviour is to be expected. Allowing volumetric dilation, but assuming complete volumetric incompressibility implies that the fibre rotation angle may not exceed twice the band angle. Fleck et al. [26] coined the

expression ‘lock-up’ to describe a state of maximal fibre rotation, see Fig. 4(c). Since after lock-up, further fibre rotation is insignificant, compressive shortening of the sample can only emanate from an elongation of the rotated segment of the fibres, i.e. an extension of the band in the longitudinal direction, Fig. 4(d). Bending theory also predicts a successive increase in bandwidth with increasing fibre rotation, but without reference to volumetric lock-up [20]. In any case, the widening of the band is known as ‘band broadening’ in the literature.

The compressive stress transferred over the band of rotated fibres during band broadening was identified as a characteristic property [23] for a given composite and is robust to imperfections. Band broadening can be observed experimentally for both fractured [27] and intact fibres [28]. Furthermore, it was shown to remain constant as the band widens [25]. It was also argued that even if fibres fracture, see Fig. 4(e), the principal characteristics still persist due to volumetric lock-up [25]. In recognition of these peculiar features, the stress transferred across the band was assigned the name ‘band broadening stress’. It plays an important role for considerations regarding the lateral propagation of kink bands and energy absorption. In sources referenced above, no theoretical argument to determine the band angle was put forward and the band angle is generally treated as an input parameter [25].

2.4. Fibre fracture after peak load

Theories that consider fibre misalignment in conjunction with matrix shear nonlinearity as the initiation mechanism for microbuckling, as discussed so far (§2.2), generally assume that fibre fracture has no effect on the peak load, and predominantly occurs in the softening regime. However, differing arguments were presented regarding the mechanism that ultimately leads to fibre fracture in the post-peak load regime. The band broadening mechanism keeps the rotated fibres in the interior of the forming kink band rather straight, therefore bending curvature is concentrated at the transition to the region of unrotated fibres, see Fig. 4(d).

In these locations of concentrated curvature, the bending stress is substantial and can induce tensile stress in parts of the fibre cross-section. Because the mechanism of fibre failure, and hence strength, may be different for compression and tension, both cases must be considered. This holds true, even though compressive stress in the cross-section is generally larger, by about a factor of 2, than the tensile stress. A possible failure mode in the part of the cross-section loaded in tension is, for instance, crack opening, and strength values can be obtained from tensile test on fibres. On the contrary, the mechanism for compressive fibre failure is less apparent. Budiansky and coworkers [16] name longitudinal splitting for glass fibres and buckling of fibrils within

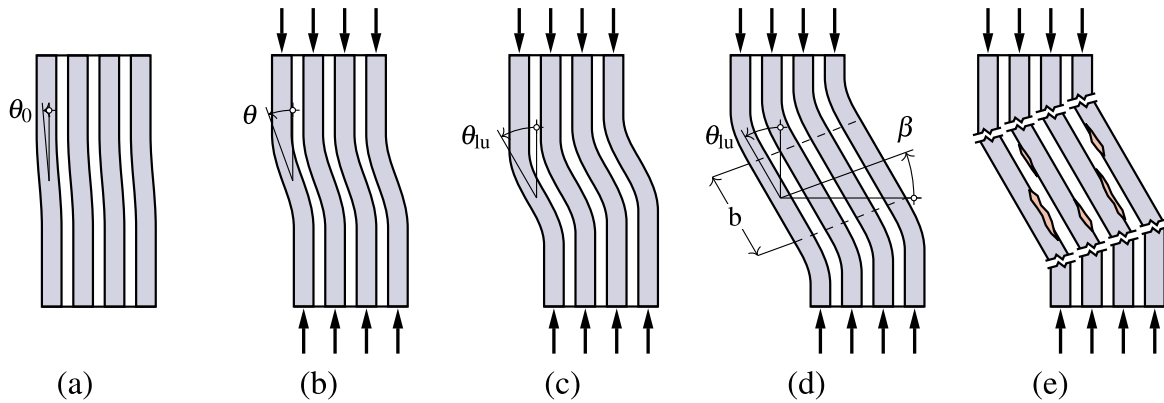


Fig. 4. Schematic representation of key stages in the progression of microbuckling: Some preexisting small misalignment θ_0 (a) induces matrix shear and eventually causes matrix nonlinearity. Soon after this point, fibre rotation θ starts (b). When rotation becomes locked-up (c) at $\theta_{lu} \approx 2\beta$ bending theory predicts the formation of a straight fibre segment b in the middle of the band (d). Eventually, or concurrently, matrix degradation, debonding and/or fibre fracture occurs (e). Degradation may also occur between (b) and (c), in particular, to accommodate volumetric expansion if $\theta < 2\beta$. Complex material nonlinearity cannot be accounted for in closed form analysis and typically only matrix yielding is considered.

carbon fibres as possible failure modes determining the apparent fibre strength. Gutkin and coworkers [29] observed shear fracture oriented at 45° to the fibre axis in carbon fibres. Vinçon and coworkers [30] performed tests on individual filaments embedded in resin for different fibre types. They observed a ratio of compressive failure strain to tensile failure strain of about 3 and 1 for high strength and high modulus carbon fibres, respectively. Otherwise, data for the compressive fibre strength associated with these modes is rare as the exact loading conditions seen by the fibre are hard to evaluate in an experimental setup. Hence, opposing standpoints were taken in the literature, with some assuming tensile failure, e.g. Refs. [20,31,32], while others argue in favor of compressive failure [8,33].

Fibre fracture is generally understood as the event terminating band broadening and, hence, defines the kink bandwidth observed *post-mortem*. Thus, a better understanding of fibre failure modes and strength under tension and compression would lead to more accurate predictions regarding the kink band morphology. Furthermore, shear stress might also affect fibre failure in addition to normal stress due to fibre bending. These issues may warrant some new investigations. Besides the two groups of researchers arguing either for tensile or compressive fibre failure in the post peak load regime, a third group stresses that early localized fibres breaks may have a significant influence on the peak load [34]. This latter class of theories are discussed separately in §2.5.

Even though the peak load is very sensitive to imperfections, some other characteristics were found to be quite robust. In particular, the energy absorbed in a structure undergoing microbuckling is quite insensitive to misalignments as a relatively constant residual strength remains after the snap back phase. This property was exploited to find e.g. the conditions under which an incipient kink band, emanating from a stress concentration, can propagate transversally [25]. A schematic of the propagation and the associated load reduction is given in Fig. 6 of [25]. Based on the consideration that the stress transferred over the band of microbuckled fibres is the band broadening stress, the critical stress for steady-state transversal propagation was obtained. The reasoning employed for this purpose is similar to Maxwell's criterion used to describe phase transitions, cf. also [35]. The attribute 'steady-state' refers to the circumstance that, at this stress, the propagation can occur in a quasi-static manner, without a net energy release.

2.5. Fibre failure as initiation mechanism

The attainment of maximal fibre stress in an essentially unrotated state is a compressive failure mode distinct from microbuckling as discussed in §2.2 and §2.3. Fleck [6] uses the name 'fibre crushing' for this mode and notes that it might occur if the matrix is particularly stiff and strong with respect to the fibres. A fibre strength-dominated failure mode was also noticed early on in specimens with very high fibre volume fractions and well bonded fibres [36,37]. Still, for conventionally employed glass or carbon composites, large scale fibre crushing is generally not considered as the strength-limiting failure mode and the basic assumption of the classical microbuckling theories is that fibre misalignment is the essential factor for the initiation of microbuckling.

However, some authors argued in favor of fibre failure as an initiation mechanism for kink band formation. Lankford [38] argued that stable pre-peak load fibre failure, due to e.g. inhomogeneous fibre strength or local defects, and the resulting damage act as the nucleus for kink band formation. He further pointed out the role of fibre-matrix interface properties, insofar that the stress redistribution in the vicinity of individual failed fibres strongly depends on fibre-matrix interface properties. Narayanan and Schadler [34] used micro-Raman spectroscopy to measure strain in the neighbourhood of individual broken fibres. They argued that kink bands originate from stable local damage events that occur before the peak load is attained. During the growth-phase, the band angle of the subsequent microbuckling is determined by a shear-lag mechanism governed by matrix and interface properties.

The authors reasoned that a stiff, elastic matrix and stiff, intact interface will cause high stress concentration near the fracture. This would cause neighbouring fibres to fail at locations very close to the first fracture and so on, thus a small or zero band angle will ensue. If the matrix is yielding, however, it tends to deform at 45° to the load axis and thus is more likely to initiate fracture in neighbouring fibres axially offset from the first fracture. Similar arguments were brought forward for the effect of the interface properties on the band angle concluding that weak interfaces bring the band angle closer to 90°. This was developed further in Refs. [39,40].

Shear fracture of fibres and a resulting fracture plane oriented at 45° to the longitudinal direction was observed for notched specimens in Refs. [29,41]. At some distance from the notch, the failure mode transitioned to microbuckling. Furthermore, Gutkin and coworkers used a numerical model discussed further in §4.3 to identify the circumstances that cause a transition from classical microbuckling to fibre failure, but no reference to a theory similar to the one by Narayanan and Schadler was made.

Attempting a connection between these results and those of [34], it could be argued that experiments indicate fibre fracture as a competing failure mode in locations of high stress concentrations. Fibre fracture as an initiation mechanism seems relevant in situations where local stresses are high enough to cause fibre failure, but for some reason microbuckling cannot initiate. In Ref. [29] the effect of 90°-plies in a laminate is cited as delaying microbuckling in the notch. The stress gradient in the notch also seems to be an important factor, as kinking theories (§2.2) are applicable only for homogeneous compression loads where the whole structure, or at least a wide enough part, can participate in the kink band formation. Conversely, inhomogeneous stress distribution might inhibit and delay the development of the kink band beyond the peak far field stress predicted by kinking theories. In such a case, a conventional crystallographic failure mode of the carbon fibres, likely driven by shear (or deviatoric) stresses, might act as a complementary mechanism. The observed crack angle of 45° near the notch is consistent with the prediction of [34] for a yielding matrix and, at some distance, the failure mode transitions back to kink banding at a much shallower angle.

2.6. Fracture mechanics interpretation

The theoretical considerations discussed so far considered a small material element representative of an unnotched structure under homogeneous loading. For the reasons elaborated there, an essentially reversible, quasi-linear behaviour can be expected before the peak load, followed by sudden collapse, i.e. brittle failure. While this behaviour is generally observed for homogeneous samples, other samples featuring stress concentrations due to cut-outs, notches or similar geometric details, fail more gradually. Notched samples also do not show as strong a scatter in strength compared to homogeneous samples [15]. In these structures, microbuckling starts at the stress concentration and subsequently spreads. Although the stress transferred over the microbuckled sections is much lower than the peak stress, stress redistribution can allow for stable propagation of the kink band, i.e. accompanied by an increasing total load on the structure.

Guynn and coworkers and Soutis and Fleck [15,42] pointed out similarities in the propagation behaviour of kink bands and cracks. This correspondence exists only in an abstract sense, i.e. the strain localization in the kink band is treated as a negative crack opening. Via this abstraction, the application of the well-developed instruments of fracture mechanics is made available to the problem of kink band propagation. Guynn and coworkers and Soutis and coworkers adapted the Dugdale model for elastic-plastic fracture in thin plates to model the problem at hand in several variants [6,15,42,43]. These approaches generally assign some residual strength to the kinked length of the component, corresponding in analogy to a traction bridging the crack. In accordance with Dugdale's theory, it is postulated that the

singularities from the far field loading and residual tractions cancel out at the crack tip, allowing the kinked length to be calculated. In more refined versions of these models some traction-negative separation law is adopted, thus defining a quantity corresponding to a fracture toughness, *i.e.* the energy that has to be expended to propagate the kink band by a unit length. This propagation energy or ‘fracture’ toughness acts as a blanket term for all dissipative effects covering yielding, fracture and friction. Measurements of this quantity for particular layups were presented *e.g.* in Refs. [44,45], although in the latter reference it was pointed out that it is not a constant and depends on the length of the kink band as is the case in fracture mechanics of finite media. An inherent limitation of fracture-mechanics-type approaches is that they only apply to the propagation phase and cannot predict the initiation in itself.

2.7. Size effects and statistics

Bažant and coworkers [46] argued that notched fibre reinforced composites suffer from a size effect, curtailing the strength of larger structures. In essence, the argument is based on the different scaling laws for microbuckling ‘fracture’ toughness, which is supposedly a constant for a given laminate, and the energy released by propagating kink bands from proportionally scaled notches, cut-outs or similar features. Experimental investigations concerned with this type of size effect can be found in *e.g.* Ref. [47]. There, the size effect due to notches and an additional size effect due to layer thickness were studied. The same effect of absolute scale on the maximum load also arises in conventional linear elastic fracture mechanics [48], and it is generally referred to as the ‘deterministic size effect’, to distinguish this mechanism from other size effects. The size effect also applies to cases where the finite extent of the fracture process zone is relevant. In this case, however, the scaling law is more complex [46].

Another mechanism by which absolute component size affects its strength is via the statistical nature of the misalignments. The assumption that the overall strength is controlled by the weakest, *i.e.* most misaligned, region implies a decrease in strength with size, as larger size increases the likelihood of a critical flaw. This argumentation is consistent with a weakest link theory and motivates the assumption of a Weibull-distribution of strength under random imperfections [49,50]. The general principle holds, although the applicability of Weibull theory has been critically assessed *e.g.* in Ref. [51]. Several investigations linking the statistical distribution of fibre misalignments are discussed in §3.4.

The circumstance that the infinite band assumption is inherent to most theoretical considerations also provides motivation for more sophisticated representation of the misalignment statistics in computational approaches. The infinite band assumption is typically not well-founded, as micrographical investigation showed that the misalignments of nearby fibres are correlated and the wavelength of misalignment fluctuations can be rather short [52], *i.e.* 10 fibre diameters, see

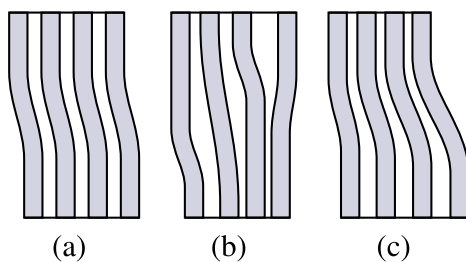


Fig. 5. Different modelling conceptions of fibre misalignment: Under the infinite band assumption (a) no change in transversal direction is considered and the misalignment is perfectly correlated. Conversely, for independently random misalignment no correlation exists (b). More realistically, misalignment of neighbouring fibres may be thought of as correlated to a certain extent (c).

Fig. 5. Even worse, the amplitude of the misalignment angle is subject to significant variation [53] within a given UD-ply, and it is not apparent how the single input value can be extracted from the distribution obtained from measurements. For this purpose, occasionally *ad hoc* assumptions are introduced to produce an ‘effective’ misalignment angle. Wilhelmsson [54] and coworkers performed experiments on a number of unidirectional non-crimp fabric samples and obtained a satisfactory agreement with predictions by (2a) and (2b) by using the 99th-percentile of the measured fibre misalignment distribution as effective angle.

2.8. Motivation for computational models

The approaches discussed so far led to a qualitative understanding of the main phenomena and mechanisms controlling the peak load and kink band morphology. These efforts provide a sound modelling of the involved physics, but generally do not enable quantitative predictions. Given the restrictions of closed-form analysis, several important factors cannot be incorporated in such a model, including: edge effects and stress gradients, complex constitutive responses, inhomogeneous misalignment distributions, among others. The open challenge of providing quantitative predictions for the multitude of phenomena that go along with compressive failure prompted a variety of new approaches published in the last 20 years, generally in a computational setting. The remainder of this article is dedicated to the discussion of these advances, starting with semi-analytical models. As a graphical aid for navigating this diverse collection of approaches, a chart that links and discriminates their most characteristic attributes is provided where appropriate. The model of these flowcharts and a description of each attribute is given in the appendix, Fig. 16.

3. Semi-analytical models

A large class of computational models derive from the historic, closed-form micromechanical methods, preserving a simplified representation of the microstructure. They however perform numerical integration which allows for incremental solution procedures. Such models are hereafter referred to as semi-analytical. A typical characteristic of this class is that the medium is partly modelled using homogenized – or smeared – properties. Occasionally, specific analytical homogenization schemes are invoked. The resulting equations are then integrated over a point, beam, or planar domain.

Peak load predictions by means of semi-analytical extensions of the ‘beam theory taking into account bending stiffness, as defined in §2.2, are discussed first in §3.1. Compressive failure criteria of the plies using approaches corresponding to an extension of the ‘kinking theory’ by Mohr-Coulomb failure theory are presented in §3.2. Approaches dedicated to the prediction of the band angle, which was postulated until then, are discussed in §3.3. The final subsection §3.4 is concerned with models tackling inhomogeneous misalignment distribution and edge effects. An overview of typical model attributes is given in Figs. 6, 7 and 8.

3.1. Behaviour predictions up to and beyond peak load

Morais and Marques [59] developed a uniaxial model based on analytical micromechanics to predict the peak load. Both a 2D and a 3D formulation were presented, each working with a unit cell consisting of a single fibre and the surrounding matrix. The authors assumed kinematics similar to Rosen’s in-phase mode, *i.e.* an initiation band angle of zero. The fibre in the unit cell featured an initial sinusoidal imperfection that would be gradually amplified by longitudinal loads until the peak load was reached. Effective shear-stiffness of the 2D model was obtained from Reuss’ constant stress-model, while a concentric cylinder approach was used for the 3D formulation. Finite strain measures and a Drucker-Prager matrix plasticity model introduced nonlinearities. fibre

Domain	Fiber/matrix	Continuum th.	Material model	Misalignment	Region
lumped parameter Wadee et al. [56–58]				uniform	infinte band
beam Morais and Marques [59]	[smeared, 2d smeared, 3d]		Drucker-Prager	harmonic	infinite band
beam Pimenta et al. [60]	smeared, 2d		perfect plasticity	harmonic	infinite band
beam Davidson and Waas [61]	smeared		fitted shear curve	hyperbolic	infinite band
beam Feld et al. [62]	smeared		[plasticity only plasticity+damage]	harmonic	infinite band

Fig. 6. Typical model attributes in §3.1.

bending stiffness was considered and numerical minimization of the potential energy rendered equilibrium states and peak loads. The predicted peak loads closely matched reference results obtained for analogous FEM unit cell models presented in Ref. [63]. In a separate publication [64] a simplified closed form solution resembling (2b) was presented.

A closed form, 1D bending theory model was developed by Pimenta and coworkers [60] for predicting the deflection profile of fibres within the kink band in the softening regime. This was accomplished by separately considering an elastic and a perfectly plastic domain in the kink band, each with respective governing equations, and appropriate transitions. The evolution of the boundary between the elastic and plastic domains was tracked.

Davidson and Waas [61] used an approach similar to the 2D model by Morais and Marques with a nonlinear stress-strain curve for the matrix shear behaviour. In accordance with (2b) their model demonstrated that sufficient shear hardening can offset geometrical softening due to fibre rotation and delay microbuckling. Unlike in Ref. [60], when the evolution of fibre deflection profile and the evolution of the plastic zone was tracked, the authors noted that the peak load did not correspond to first yielding of the matrix in contrast to the assumptions made in Ref. [60]. Instead, the maximum load occurred after the first yielding and when a sufficiently large volume of matrix has yielded to allow the fibre bending to overcome the decreasing tangent stiffness of the matrix. Davidson and Waas have illustrated the fundamental mechanisms by which a kink band forms, see Fig. 10 of [61]. These findings were in close agreement with refined FE models of the kink band formation [12,65,66] that show that the maximum load does not correspond to first yielding of the matrix.

Feld and coworkers [62] studied the energy dissipated during microbuckling. The representation of material nonlinearity by either plasticity or damage is decisive for this purpose, and the authors showed that the assumption of a purely plastic response without some sort of softening, ensuring finite dissipated energy, overestimates dissipation by orders of magnitude. To obtain accurate results, a matrix material model with damage variables for transversal tension and matrix shear was employed in this investigation. fibre fracture was considered via a separate criterion. In extension of earlier investigations by Guimard and coworkers [32], the micromodel was employed to study the effect of applied far field shear stress and fibre misalignment on the peak load failure envelope and the energy dissipated during micro buckling. Far field shear had the effect of linearly decreasing peak stress, its value reaching zero when the shear field equals the composite's shear strength. However, it did not have any significant effect on dissipated energies for low shear values, since the widening of the shear band appears to compensate the decreasing strength. The linear decrease of peak compressive stress with applied shear was experimentally verified e.g. in Ref. [67]. Furthermore, Eyer and coworkers [68] found a linear decrease of peak compressive strain with the damage variable associated with shear, also linearly dependent on shear stress for low values.

Wadee and coworkers [56] presented an adaptation of an earlier approach, initially intended to predict the band angle for layered materials sliding under friction, to the problem of compressive failure of fibre composites. The model is based on a somewhat abstract representation of the composite via a set of rheological elements. These elements represented the shortening and bending stiffness of the fibres as well as the shear and transverse stiffness of the matrix. For the matrix shear stiffness, a bilinear relation was used, with initially positive stiffness followed by either hardening at reduced stiffness or softening. fibre bending was abstracted to a discrete rotational spring. For this discrete set of rheological elements, the total potential energy was formulated in terms of the degrees of freedom: longitudinal shortening, fibre rotation, and bandwidth. Subsequently, closed form expressions for longitudinal load and bandwidth in terms of band angle and fibre rotation were obtained from the condition of stationary potential energy. Unlike in the precursor model, however, the adaption does not attempt to predict the band angle, but rather uses it as an input parameter. The model also does not feature an initial misalignment angle, thus the peak load results correspond to Rosen's. However, matrix nonlinearity is reflected in the bilinear shear stiffness, hence post-peak load behaviour of the model is representative for fibre composites. Adjusting the material properties to match the same AS4/PEEK composite as used in Ref. [66] the authors performed parametric studies. Notable findings were that, beyond a certain (fixed) band angle, the bandwidth no longer increased monotonically with respect to increasing fibre rotation. Also, the residual load bearing capacity at lock-up showed a local minimum for some particular band angle.

A more comprehensive investigation of the effect of various material nonlinearities in the same model was performed by Zidek and Völlmecke [57]. For this purpose, the authors replaced the bilinear shear nonlinearity model with a power law hardening response and considered additional material nonlinearities in other, previously linear, elements. Out of these refinements, the nonlinear shear law was found to have the highest impact, while nonlinearity of matrix transversal stiffness, *i.e.* due to cracking, was found to be innocuous. The results for the residual load at lock-up were in good agreement with the predictions of the micromechanical model by Kyriakides and coworkers [66]. A further development of this model was presented in Ref. [58] where it was combined with a Ritz approach to model structural effects in laminates.

3.2. Ply failure criteria

The essentially linear response of composite plies until approaching the peak load and the following unstable collapse motivated the development of simple, ply-based failure criteria for compressive failure. This is done in the context of physically founded failure theories that have become common in the last years. In general, inter-fibre failure is the foremost concern of these theories and failure in the fibre direction is often modelled simply by non-interacting maximum stress criteria. However, Davila and coworkers and Pinho and coworkers have

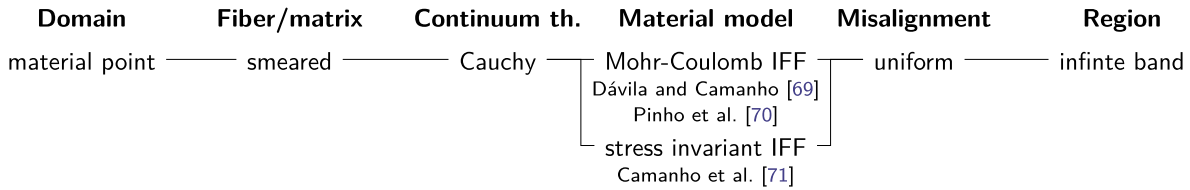


Fig. 7. Typical model attributes in §3.2.

developed theories that predict the compressive strength in nominal fibre direction based on inter-fibre fracture caused by shear in misaligned regions. The classical Mohr-Coulomb model for brittle fracture is the underlying hypothesis for several variants of inter-fibre failure theories. A non-exhaustive listing of notable publications on this topic includes Puck and Schürmann [72], Davila and Camanho [69], and Pinho and coworkers [70].

In Mohr-Coulomb-type theories, fracture is assumed to occur in an *a priori* unknown fracture plane which is characterized by the stress acting in this plane attaining a critical value. The *effective* shear on the fracture plane, however, is reduced by a friction-like mechanism caused by normal stress on the fracture plane, *cf. e.g.* Puck and Schürmann [72]. Shear and normal stress on the fracture plane are related to the far field stress by the appropriate coordinate transformation. Potential inter-fibre fracture planes are rotated by an unknown angle about the longitudinal direction and, in general, the critical plane has to be found iteratively. For plane stress, however, the fracture plane can be estimated analytically and three modes are distinguished based on the far field stress state: (a) transverse tensile, (b) predominantly in-plane shear, and (c) predominantly transverse compression, *cf.* [73] for further details.

Although strength in nominal fibre direction is typically not the focus of these theories, Davila and coworkers [69] applied an inter-fibre failure criterion in the coordinate frame of misaligned fibres to deduce the compressive strength of homogenized UD-ply. More precisely, the authors considered the stress state in a coordinate frame aligned with fibres rotated from the nominal longitudinal direction, either due to misalignment alone or misalignment plus additional pre-failure rotation. In this publication a pure in-plane fibre rotation was considered. In the case where only initial misalignments exist, an analogon to the expression (2a) derived by Argon for a rigid-ideally plastic matrix was obtained, with shear fracture strength substituted for shear yield strength. Furthermore, the extension by Davila and coworkers deviates from (2a) by a modification accounting for the frictional parameters arising from the Mohr-Coulomb model. In a similar manner, a strength prediction analogous to (2b) was obtained by considering an elastic shear response up to failure.

In Ref. [70] Pinho and coworkers extended these investigations by considering a generic nonlinear matrix shear response and finite fibre rotations. In this context, the authors also contemplate the possibility of the compressive strength being controlled by a shear instability rather than material failure under shear. In an effort to more accurately predict the strength under plane stress loading, an out-of-plane misalignment was considered in addition to the purely in-plane misalignments considered before.

The same principle of using an inter-fibre failure criterion in a misaligned coordinate frame to find the compressive strength was also

employed by Camanho and coworkers [71]. There, the Mohr-Coulomb based criterion was substituted with a failure surface formulation in terms of stress invariants, *cf. e.g. Refs.* [74,75].

3.3. Band angle prediction

The inability of simple, closed form models to predict the band angle has been noted in §2.3. This lack of knowledge regarding the mechanisms controlling the kink band angle was cited as a motivation in an investigation by Schapery [76]. In contrast to earlier approaches employing deformation theory to represent material nonlinearity, Schapery used a thermodynamically consistent formulation based on a single internal damage variable to represent shear and transverse matrix nonlinearity. The evolution of the respective engineering constants with the internal variable was calibrated from coupon tests of a carbon/epoxy composite. Another particular feature of the approach is the usage a finite strain formulation specialized for plane strain/plane stress. Only in-plane microbuckling was considered, but under a generic far field stress state. The resulting governing equations were solved numerically and, with some simplifications, analytically. In the investigation, the pre-existence of infinite band misalignments was assumed with the band angle treated as a parameter. Results for models including a nonlinear hardening behaviour predicted the smallest peak load for a band angle of zero, similar to the approaches discussed in §2.3. These results, however, were obtained without any provisions to account for matrix fracture and the peak load for experimentally reasonable band angles was found to be only marginally higher. Moreover, upon adopting a simple matrix fracture criterion featuring a linear interaction of shear and transversal stress, the results predicted matrix fracture for realistic band angles, but not for unrealistically low ones. It was then argued that realistic imperfections are not infinite bands, thus the peak load calculated for the zero band angle can be exceeded somewhat and matrix fracture is triggered. Further it was stated that the experimental band angle matches the lowest band angle for which matrix fracture occurs. The numerical results presented were for carbon/epoxy AS4/3502 for which a band angle of 17° was predicted. The band angle was found to be sensitive to the transversal strength, but relatively insensitive to the misalignment angle and, in consequence, the peak load.

Later Basu and coworkers [77] also approached the band angle problem. Unlike Schapery's, their approach considered both fibre rotation and the band angle as evolving quantities. The strain arising from the evolution of fibre rotation and band angle was considered via nonlinear kinematics, thus representing the effect of the band angle on shear and transversal strain. The strain in the band was composed of the strain due to the band kinematics and the far field strain via the appropriate coordinate transformation. The customary deformation

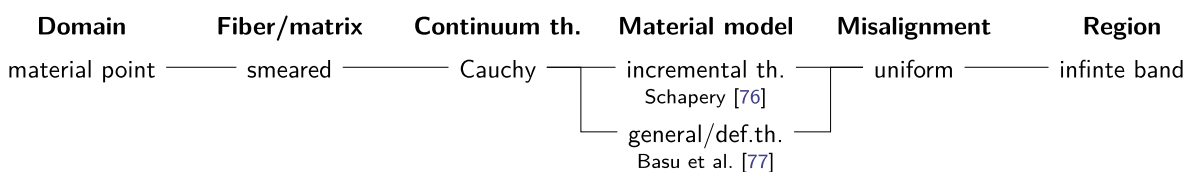


Fig. 8. Typical model attributes in §3.3.

theory plasticity model with power law hardening was then used to model the material response within the band. This led to a set of non-linear relations of far field stress components to local stress components in a coordinate frame aligned with the band containing the rotated fibres. In the special case of a vanishing band angle and uniaxial longitudinal compression, the classical equilibrium relations in (2) were recovered from the extension. Employing a numerical solution scheme, the evolution of the band angle under an applied far field stress state was calculated. The material data used was representative for AS4/3501-6. For a uniaxial far field loading, the authors found a steady increase in the band angle to 7.75° at peak load. Repeating the calculation for simultaneous far field shear and transverse stresses rendered failure envelopes in the respective section of stress space. The set of governing equations was also used in a perturbation analysis to derive a criterion for stability of an equilibrium state with respect to perturbations of the band angle and the fibre rotation. The developed stability criterion predicted bifurcation for cases of large transversal compression, but not for any other investigated load combination.

A synthesis of this approach and the thermodynamically consistent material model for matrix damage from Ref. [76] led to a 2D progressive damage model presented in Ref. [78]. It was applied to predict in-plane microbuckling of thick laminates via a FE-model.

3.4. Misalignment distribution and edge effects

Peak load predictions of all models discussed so far make explicit reference to a single initial misalignment angle. However, the inability to account for the actual statistics of imperfect fibre alignments in this manner was pointed out in §2.8. To shed some light on the probabilistic aspect of the problem a series of successively generalized investigations were published by Slaughter and Fleck [79], Fleck and Shu [80] and finally Liu and coworkers [82]. In all models a bending type theory was employed to consider the wavelength of misalignments in addition to their magnitude (see Fig. 8).

An early approach to the problem was made by Slaughter and Fleck [79] using a 1D bending theory model. In the 1D model, the infinite band assumption is inherent, but in the longitudinal direction, a stochastic distribution of the misalignment amplitude and wavelength was considered. The ability to model both wavelength and amplitude of the initial misalignment, rather than just their ratio given by the misalignment angle, is particular to bending theory models. To quantify the random initial misalignment, the authors argued that the misalignment profile along the longitudinal direction can be characterized by its Fourier transform. This technique accounts for the statistical distribution and the autocorrelation of the misalignment in terms of spectral densities. At that time no measurements of characteristic spectra of misalignments in fibre composites were available, so the spectrum had to be assumed. Later Clarke and coworkers [83] tracked individual fibres in glass fibre/epoxy composites and used that information to calculate the misalignment spectrum. Random fibre misalignment profiles

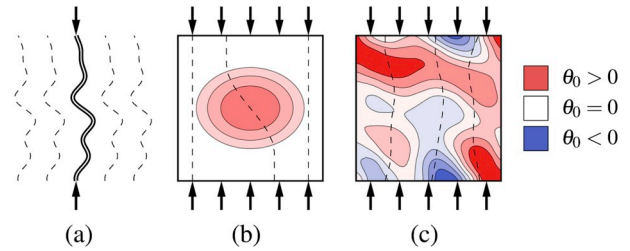


Fig. 10. Schematic of initial misalignment distributions as referred to in Fig. 9: (a) ‘random-infinite band’, (b) ‘harmonic-single patch’, and (c) ‘random-distributed’. Dashed lines represent implied, but not explicitly modelled, fibre paths. Contours in (b) and (c) are curves of constant misalignment angle θ_0 .

along the longitudinal direction were generated as random realizations consistent with the assumed spectral density, see Fig. 10(a) for a schematic. These random realizations were then used in a Monte Carlo simulation solving the governing equations of the 1D couple stress problem. The obtained peak load distribution for a large number of realizations with equal length was found to closely match a 2-parameter Weibull distribution. Based on this result, the conclusion was drawn that the peak load of the 1D infinite imperfection model is controlled by its weakest link, i.e. the segment with the largest fibre misalignment. For the same reason it was argued that the peak load tends towards zero as the model length is increased to infinity under the modelling assumptions used there. It was reported that the results were insensitive to the shape of the spectrum but sensitive to the highest included frequency and mean square value of misalignment. Accounting for fibre bending provides a noticeable mitigation of the effect of misalignment angles associated with small wavelengths. Hence, kinking theory models give lower bounds for the peak load compared to bending theory models. Since then, this finding has been corroborated by several other investigations, cf. e.g. Ref. [66] discussed in §4.1.

Fleck and Shu [80] abandoned the infinite band assumption by considering a 2D model of an ellipsoidal region of misalignment embedded in a domain of straight fibres, see Fig. 10(b). For this purpose they applied the smeared Cosserat material model in a finite element formulation. Investigating the effect of the transversal extent of the misaligned region, they found it falling between two limit cases: For vanishingly narrow ellipses, only a few fibre diameters wide, the peak load approached Rosen’s result (1). Conversely, the peak load approached the predictions based on the infinite band assumption within 20% for ellipses as wide as 400 fibre diameters.

Liu and coworkers [82] produced a synthesis of the previous approaches by integrating the stochastic misalignment generation procedure from Ref. [79] into the 2D finite element model of [80], see Fig. 10(c). Like before, the statistical misalignment properties were accounted for via their respective power spectrum. The conclusions drawn from this investigation largely coincide with the ones

Domain	Fiber/matrix	Continuum th.	Material model	Misalignment	Region
beam	smeared			random	infinite band
Slaughter and Fleck [79]					
plane	smeared	Cosserat Fleck and Shu [80] Cauchy+rebar Lemanski and Sutcliffe [81]		harmonic	single patch
plane	smeared		Cosserat Liu et al. [82] Cauchy+rebar Sutcliffe [55]		random

Fig. 9. Typical model attributes in §3.4.

summarized above for the 1D case in Ref. [79].

Lemanski and Sutcliffe [81] also used a smeared description of the composite, but devised a somewhat different technique to implement it in FE models. Instead of employing a Cosserat continuum with additional degrees of freedom, the fibre and matrix constituents were represented by separate element types. For plane stress models, planar shell elements were assigned isotropic matrix properties and coupled with beam elements. For 3D models, the shell and beam elements were replaced by solid and rebar elements for matrix and fibre, as appropriate. Due to this modelling approach, shear and transverse effective material properties are determined by the matrix alone and the contribution of the fibres is neglected. A J_2 -plasticity model was used to model matrix nonlinearity. A preliminary study of the effect of fibre bending stiffness on peak load confirmed the conclusions, drawn in Refs. [79,82], that it can be safely neglected for undulation wavelengths of 200 times the fibre diameter. Further considerations regarded the interaction of misalignment regions with their surrounding, by comparing differently sized and shaped patches of misaligned fibres embedded in otherwise perfectly straight plies. Also the effect of positioning the misaligned patch at the specimen center or near the free edges was considered. Overall, their findings confirmed and extended previous results by Liu and coworkers [82]. A similar model featuring a defined autocorrelation of fibre misalignments was used in Ref. [55] to study the statistical size effect *cf.* §2.7. The approach considered a homogeneous sample with a misalignment pattern of defined autocorrelation properties. For given statistical distribution and autocorrelation of misalignments, more detrimental flaws occurred, on average, in larger models than in smaller ones, thus reflecting the statistical size effect. This approach, however, ruled out misalignment wavelengths below 200 fibre diameters, so that fibre bending stiffness could be neglected.

3.5. Preliminary conclusions and motivation for explicit micromechanics

The approaches discussed, heretofore, all rested on a simplified representation of the micro-structure, thanks to homogenized or smeared mechanical properties. Semi-analytical developments allowed more accurate prediction of the overall nonlinear response, peak load, post-peak behaviour, band angle, and a variety of effects such as continuum damage mechanics, misalignment statistics, and edge effects. However a number of influences remain out of reach, among which are fibre-scale stress gradient effects and fibre-scale misalignment distributions, discrete failure mechanism combination between microbuckling, fibre debonding, splitting, and fibre failure - as an initiation mechanism. Taking advantage of increasing computational power and refined measurement techniques, explicit micromechanical models, presented in the next section, aim at answering those open questions.

4. Explicit micromechanical models

The approaches described previously require substantial simplification of the microstructure and its properties, which prevents an accurate modelling of the underlying micromechanical behaviour at the scale of the fibre diameter. A direct micromechanical representation of the involved mechanics at the microscale, however, was desired by several researchers. Finite element models featuring a separate resolution of fibre, matrix and possibly interphase constituents appear well suited for this purpose. They allow, in principle, an accurate representation of microbuckling, splitting, and fibre failure. A typical challenge in such approaches, however, is the determination material parameters at a microscopic scale.

In its classical incarnation, micromechanical models consist of a 2D or 3D slice of alternating fibre and matrix segments representing a single UD-ply, see Fig. 11. This modelling approach offers some innate advantages: The fibre stripe thickness endows the fibres with bending stiffness which is a requirement for a well defined bandwidth. The

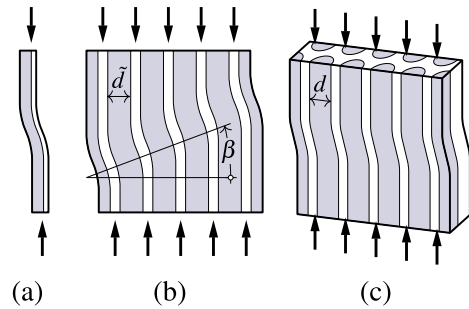


Fig. 11. Schematic of typical micromechanical models. Areas assigned fibre properties are shaded, matrix is left white. Single-stripe models (a) are used with periodic boundary conditions left to right. This enforces a band angle β to zero. Other plane models (b) use zero traction boundary conditions to allow a nonzero band angle, but the model needs to be sufficiently large to mitigate boundary effects. Models (a) and (b) are generally plane strain or plane stress. Plane models can respect either the actual fibre diameter or the actual fibre volume content. (c) Volume slice models may restrict out-of-plane motion, effectively enforcing plane strain. The number of fibres in (b) and (c) is typically much larger than shown here.

width of the stripes is typically adjusted to match either the fibre volume content of the composite or the fibre bending stiffness. If a more accurate representation of the complex triaxial stress state that results from the fibre geometry is desired, 3D volume slices are an option. The separate resolution of the constituents allows to use separate material models for failure and degradation as well as interface elements to model fibre-matrix debonding. A disadvantage is that the fibre- or matrix-stripe thickness controls the mesh size, which can result in significant numerical effort, in particular for 3D models. See Fig. 12 for an overview of approaches covered in §4.1.

Some care is required with regard to the interpretation of results of finite element ‘unit cell’ models due to the strain localizing nature of microbuckling. In the softening regime, the response of the micromodel depends on its own size and does not constitute a representative volume element (RVE) for the bulk composite [84]. Another aspect is the definition of suitable boundary conditions at the transverse edges of the model. Periodic boundary conditions constrain the band angle *a priori*, but the band angle is, in general, not known in advance and reorients in the post-peak regime. As an alternative, zero traction boundary conditions are typically used and free edges are marginalized by choosing a sufficiently large model. A comparative study of micromodels with periodic and zero traction boundary conditions was performed by Romanowicz [85].

The high resolution of the discretization required for micromodels leads to substantial numerical cost, in particular for 3D models. Therefore, many micromechanical analyses are limited to either 2D plane strain models or effectively plane strain 3D models. Another difficulty is the proper representation of the spatial distribution of the misalignment angle, whose importance was discussed in §3.4. The limitation to model sizes of a few tens of fibre diameters generally allows only the representation of a local distribution of misalignments.

4.1. Discrete microbuckling and microstructural effects

The archetype of micromechanical models was used by Kyriakides and coworkers to simulate microbuckling in UD plies manufactured from AS4/PEEK. The model progressed through several stages. In its initial iteration [65,66] it started as a simple 2D plane strain finite element model where the composite was represented by a regular arrangement of alternating fibre and matrix stripes with thicknesses adjusted to match the desired volume content. The plane strain assumption was motivated by accompanying experiments that employed a confinement fixture. Zero traction conditions were applied on the transversal boundary, and a suitable model size was identified via a

Domain	Fiber/matrix	Continuum th.	Material model	Misalignment	Region
plane strain	discrete Kyriakides et al. [66]	Cauchy	J_2 -plasticity	variable	single patch
plane strain	discrete Hsu et al. [86]	Cauchy	J_2 -plasticity	variable	single patch
volume slice					
plane strain	discrete Vogler et al. [87]	Cauchy	Drucker-Prager	variable	single patch
volume slice					
volume slice	discrete Hsu et al. [88]	Cauchy	visco-plasticity	variable	infinite band
volume cylinder	discrete Yerramalli and Waas [89]	Cauchy	J_2 -plasticity	eigenmode	infinite band

Fig. 12. Typical model attributes in §4.1.

convergence study.

In Ref. [66], a nonlinear material behaviour was considered for both fibre and matrix. The mildly nonlinear elastic constitutive behaviour of the fibres was soon found to be of little significance, but the matrix nonlinearity was confirmed to be a crucial parameter, as expected. Matrix nonlinearity was represented by incompressible J_2 -plasticity [66,86] in earlier approaches. The considerations discussed in §2.3, however, imply a relation between band angle and volumetric strain. Therefore, the plasticity model was later changed to a dilatant Drucker-Prager model in order to study the effect of compressibility [87]. As a result, the band inclination, although robust to most parameters, was confirmed to be sensitive to the dilatancy of the matrix in the finite element studies also. Furthermore, it was pointed out that the hardening curves of pure matrix resin do not coincide with the hardening behaviour of the *in situ* matrix, which was argued to be due to the multi-axial stress state induced by the fibre inclusions. For this reason, the matrix hardening curve used in the 2D model was not taken from shear tests on pure matrix, but was adjusted to match the in-plane shear hardening of a test on the composite. In Refs. [65,66] the suitable matrix properties were found from a separate 3D fibre-matrix RVE where the matrix hardening was calibrated so that the RVE response matched shear tests on the composite.

The same group [86] also investigated the applicability of a 2D model by exchanging the plane cross-section with a 3D volume slice containing cylindrical fibres. A regular hexagonal fibre arrangement was assumed for this purpose. As before, out-of-plane motion was suppressed in this type of model by applying appropriate boundary conditions at the section planes of the slice and effectively enforcing plane strain. In comparison to the 2D models, some quantitative differences in bandwidth and angle were reported, which were attributed to the differences in fibre bending stiffness. Later publications, e.g. Ref. [87], by the same research group employed the 3D model.

In Ref. [66] the initial implementation of the 2D model was subjected to an extensive parametric study considering several model quantities. In particular, the effect of imperfect fibre alignment was studied. To investigate if the misalignment angle alone is a sufficient characterization of the imperfect alignment, an infinite band fibre undulation of sinusoidal shape with a defined wavelength and amplitude was applied. It was confirmed that the misalignment angle, *i.e.* the quotient of amplitude over wavelength, is the most influential parameter on the peak load and that the direct effect of the magnitude of amplitude and wavelength is relatively minor. Specifically, it was found that, for long wavelengths, *ca.* beyond 150 fibre diameters, only the maximal misalignment angle, as derived from amplitude and wavelength, is essential. In addition to infinite band imperfections, the effect of the transverse distribution of the alignment imperfections was studied. Sinusoidal imperfections with exponential amplitude decay in the transversal direction showed a significantly higher peak load than the infinite band imperfection, further highlighting the importance of an accurate representation of the distribution of misalignments. In

summary, the findings regarding the effect of the misalignment distribution were similar to corresponding results obtained from homogenized bending theory approaches discussed in §3.4. The model also replicated the course of events predicted by the analytical considerations. After peak load, the inclination of the band noticeably increased, and band broadening was observed as well. Band orientation and width were found to be relatively insensitive to imperfections in a parametric study.

A 3D plane strain volume slice micromodel was used in Ref. [88] to investigate band broadening during softening featuring visco-plastic effects. The matrix was modelled by an elastic-visco-plastic material with J_2 -plasticity and power law viscosity. Contrary to previous approaches, periodic boundary conditions were used with the periodicity in transversal direction adjusted in order to control the band angle in a parametric study. Simulations were sustained beyond the peak load and, after the softening phase, the far field applied stress remained relatively constant. The stress level in this load regime was dubbed the 'plateau stress'. At the plateau stress, the maximal fibre rotation remained stationary and the bandwidth increased by forming, and subsequently elongating, a virtually straight segment of fibres in the band. This behaviour was related to the band broadening mechanisms inherent to bending theory, *i.e.* that a fixed band angle and the volumetric incompressibility provoked an arrest of the fibre rotation. General aspects of bending theory were already discussed in §2.3 and §3.1, and the specifics of the band broadening mechanism and plateau stress itself were investigated in Refs. [20,23,25]. Furthermore, it was demonstrated that, with changing band angle, the model shows the trend in the magnitude of the band broadening stress as predicted by bending theory, although quantitative differences remained. It was concluded that the accuracy of the model could be improved by a better representation of the mechanism arresting the fibre rotation.

In further analyses on the same basis, the effect of a superimposed far field shear was investigated in Ref. [67]. Peak loads of numerical models with an infinite band imperfection under both longitudinal compression and in-plane shear were found to be in good agreement with a modified version of (2b), where the far field shear stress was added to the numerator. Normal and shear far field loadings were applied sequentially, but the loading history was found to be insignificant.

The transversal propagation of the band from a local imperfection at a free edge was investigated in Refs. [22,87]. The model and accompanying experiments exploited the circumstance that the snap-back response under normal loading with shear preload can be transformed to a snap-through response under shear loading with a normal preload. As a result, compression-torsion test were stable in rotation despite being unstable in displacement. By controlling the shear angle, a quasi-static deformation was achieved. The plasticity model was changed to a dilatant Drucker-Prager model to study the effect of compressibility. Band inclination was found robust to most parameters, but sensitive to the dilatancy of the matrix.

Wind and coworkers [90] used the finite strain constitutive model

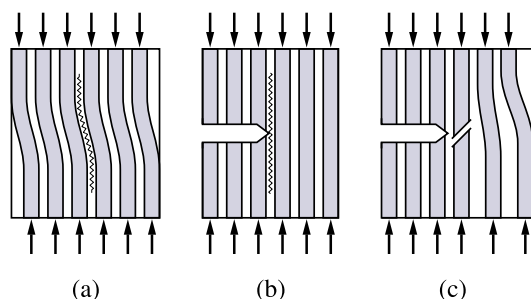


Fig. 13. Possible interaction of failure modes: microbuckling may trigger longitudinal splits (a). On the other hand, longitudinal splits emanating from a crack tip may also shield nearby fibres from microbuckling (b). In other cases, microbuckling may also be initiated by fibre fracture in a region of stress concentration like the tip of a notch as shown in (c).

from Ref. [91] in a 2D micromechanical model to investigate the relation of kink band angle with fibre rotation. They noticed a certain dependence of the band angle on the width of the band of initial misalignment. Furthermore, the results from the micromechanical model were in approximate agreement with the condition of volumetric incompressibility, *i.e.* the band inclination was observed to follow about half the fibre rotation angle.

Most micromodelling approaches do not attempt to represent an actual fibre topology and assume a regular arrangement. To verify this modelling technique, Lee and Waas [13] considered non-uniform fibre spacing and found that it had little impact on the peak load. Yerramalli and Waas [89] also compared the peak load obtained from a 3D model of a cylindrical specimen to results from 2D plane strain models. The peak load obtained from the 3D model was substantially lower. The model consisted of a matrix cylinder with 37 embedded fibres which was deemed a representative microsection. Orthotropic fibre properties were considered and the matrix response was modelled by J_2 -plasticity with the hardening curves calibrated so that the torsion response on the cylinder matched test data of a macroscopic specimen.

Lapusta and coworkers [92,93] compared several 3D unit cell models via a linear buckling analysis. Although linear buckling analysis cannot predict microbuckling in Argon's sense, *i.e.* due to initial misalignment and matrix nonlinearity, it yields bifurcation loads consistent with Rosen's theory. The authors studied the bifurcation loads of several 3D models comparing isotropic and anisotropic fibre elasticity, square and circular fibre cross-sections, dense and dilute fibre arrangements.

4.2. Interactions with debonding and matrix damage

Although micromechanical models with an abstract representation of matrix nonlinearity via plasticity are most prevalent in the literature, some authors strived for a more accurate depiction of fibre-matrix interface debonding and matrix damage. Debonding and matrix damage can be observed as diffuse microscopic events distributed over a damaged region or as localized, discrete longitudinal splits.

Prabhakar and Waas [12] conducted a parametric study of the effect of fibre-matrix debonding. They used a 2D stripe model with cohesive interface elements allowing for mode I and mode II debonding and repeated simulations with different strength and toughness for both modes. Other aspects were modelled simply, using a J_2 -plasticity model and a uniform imperfection angle. They found that, for sufficiently low mode II strength, debonding failure can compete with microbuckling due to matrix shear nonlinearity. In models that failed by debonding, the inelastic shear strain localization, distinctive for a kink band, was not observed.

Several 2D plane strain models were considered by Pimenta and coworkers in a computational analysis accompanying experimental and analytical methods [33]. One model allowed for cohesive fibre-matrix

debonding and a separate model featured a continuum damage model for the matrix.

Bishara and coworkers [94,95] performed a progressive failure analysis with degrading material models for fibre and matrix in a micromechanical 3D slice model. The fibre failure model assumed that high *in situ* strength prevents failure under compression and fibre fracture occurs under tension. A parametric variation of the fibre tensile strength showed a strong correlation with the band angle, with higher fibre strength causing steeper angles. This correlation was anticipated by analytical considerations in Ref. [25].

4.3. fibre failure as initiation mechanism

Although much evidence has been gathered linking microbuckling to imperfect fibre alignment, an alternative (or complementary) initiation mechanism considering fibre failure and subsequent matrix damage as the decisive element was discussed in §2.5. Fracture planes oriented at 45° to the longitudinal direction indicating compressive fibre failure were experimentally observed in notched samples by Gutkin and coworkers [29]. At some distance from the notch, the fracture plane transitioned to a regular kink band at a more shallow angle, as the sliding of fibre fracture surfaces apparently induced sufficient misalignment to initiate microbuckling, see Fig. 13(c).

These observations motivated further investigations to clarify the role of fibre strength which were presented in Ref. [96]. The micromechanical model developed for this purpose consisted of a single fibre-matrix stripe under plane stress with applied periodic boundary conditions. The periodicity enforced a band angle of zero and the initial misalignments constituted, in effect, an infinite band imperfection. To model fibre fracture, a simplified continuum damage model based only on longitudinal stress was used, neglecting any interaction with other stress components. This model was then employed to search the longitudinal compression/in-plane shear far-field stress plane to identify the respective domains for fibre fracture and microbuckling as strength-limiting failure modes. The search was repeated for different initial misalignments and fibre strengths. The outcome of the investigations was that, for very small misalignment angles and moderate fibre strength, the failure envelope defined by microbuckling is truncated by the fibre fracture mode in the compression-dominated region of stress space. For larger misalignments, the fibre strength-controlled failure region vanished and peak load is exclusively limited by the microbuckling strength.

An investigation by Yerramalli and Waas [89] studied fibre diameter size effects. A description of their model is given at the end of §4.1. They found that smaller fibre diameters led to larger fibre strains and interpreted this result as an affirmation of the hypothesis that fibre fracture does affect the peak load, by precipitating micro-buckling, as formulated by Narayanan and Schadler [34].

4.4. Preliminary conclusions and motivation for multiscale approaches

All the approaches discussed so far rested on a strictly micromechanical description of both morphology and loading. Explicit description of the microstructure allowed authors to explore local microscopic effects and also confirming some theoretical foundations of semi-analytical models. For instance, the role of fibre fracture as a possible catalyst for micro-buckling and the kinematics of kink-band initiation and propagation were illustrated. However, upscaling these results into ply-scale behaviour, beyond simple failure criteria (*e.g.* as in §3.1), is no easy task. Further, uncertainty models and their propagation across scales must be addressed in order to design engineering-scale structures. This prompted the development of multiscale approaches to establish a direct link between micro- and macro-mechanics.

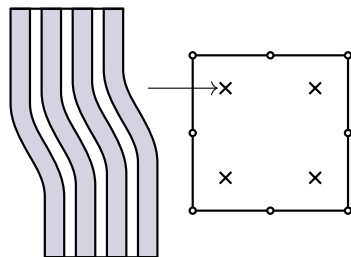


Fig. 14. Identification of a mesoscopic constitutive model for a homogenized model at a larger length scale.

5. Multiscale models

The models described up until now have been used with notable success to predict peak stress, kink-band morphology and other microscopic characteristics. However achieving convincing predictions at the structural scale, e.g. macroscopic behaviour and failure, requires taking into the interactions between the micro and macro scales.

At the risk of over-simplifying, two main considerations motivate these investigations: The identification of a physically sound ply-scale constitutive model to analyze complex geometries, or the study of ply-scale effects – size, gradients, damage mechanisms – and their interaction with microbuckling. Both of these motivations will be addressed in turn in the following.

5.1. Identification of a mesoscopic constitutive model

Considering the meso-scale as the scale of the homogeneous plies, a mesoscopic constitutive model represents the equivalent response of each elementary ply as a homogeneous anisotropic material. The process of extracting such a behaviour from micromechanics is called homogenization, see schematic in Fig. 14. Elastic properties have long been predicted with various levels of accuracy with a variety of schemes (e.g. Ref. [59]), together with elastic limits and other brittle failure criteria (e.g. Ref. [97]). However progressive failure and more generally nonlinear responses often lack theoretical foundations which prevent simpler schemes from offering reliable results. Therefore, so-called numerical homogenization approaches, relying on refined micromodels of the kind described previously, are predominantly employed [98].

Perhaps the first significant step in this direction is due to Fleck and Shu [80], who identified a Cosserat-continuum elastic-plastic behaviour based on the unit-cell response of the underlying fibrous composite. This homogenization analysis relied on a principle of virtual work equivalence, which allowed the authors to relate the independent Cosserat rotation with the rotation of the fibres.

In the same spirit but considering a Cauchy macroscopic continuum, Feld and coworkers proceeded to upscale the response of their previous micromodel [62] at the meso-scale [99]. In order to reproduce the fibre waviness-induced elastic nonlinearity both in compression and tension without a Cosserat medium, an *a priori* reduced model schematized as a truss structure with an additional rotating degree of freedom was introduced. The mechanical properties of the composite were assumed identical to a regular meso-scale model in all directions, except in the fibres, where the truss structure allowed reaction thanks to a nonlinear spring resisting its transverse displacement. The initial offset of the truss was linearly related to the fibre waviness and the far field shear strain. It was shown that the stiffness, damage, and plasticity parameters of the transverse spring, coupled with the rest of the multiaxial meso-model, could then be easily identified thanks to a principle of virtual work equivalence with the response of the bending theory model.

Bednarczyk and coworkers [100] employed a homogenization scheme based on a variant of the generalized method-of-cells [101] to determine a stochastic homogenized model. Using this method,

effective stiffness and stress concentration tensors were calculated for a repeating unit cell micromodel containing a single fibre in a cubic arrangement. The obtained tensor quantities were subjected to a transformation implementing the misalignment. The availability of the stress concentration tensor allowed the examination of yield- or failure-criteria in each matrix cell for given macroscopic stress states. This result was exploited to generate surfaces of failure initiation in macroscopic stress space. Furthermore, effective stiffness properties were determined by assuming a probability distribution of fibre misalignment angles and performing suitable averaging techniques.

Some authors used a combined micromechanical/homogenized model to take advantage of the efficiency of the homogenized description for the off-axis plies, while maintaining a micromechanical resolution in the plies subject to microbuckling. This generally requires the modification of the fibre-diameter-to-ply-thickness ratio to avoid excessive numerical effort. Prabhakar and Waas [102] employed the concentric cylinder method to find homogenized properties for off-axis plies in a laminate, i.e. plies not oriented in the loading direction. For the elastic regime, the concentric cylinder method provided the effective moduli directly from the elastic moduli of the constituents and the volume fraction. Beyond the elastic regime, the incompressible Hill's plasticity model was used to represent the effective material response of the homogenized material. The hardening behaviour of Hill's potential was then calibrated via a series of secant moduli obtained from the concentric cylinder approach. No plasticity was assumed for the longitudinal direction for this purpose, but a nonlinear stress-strain relation was used for the matrix contribution.

In order not to postulate any form of macroscopic behaviour, homogenization schemes may also be used to iteratively provide the tangent response for every integration point at every increment in time. This computationally intensive variant is usually called multiscale homogenization or FE² [103]. Nezambadi and coworkers used such an approach in Ref. [104], combined with a higher order solution scheme, cf. [105], and limited to plane stress problems. The authors used this type of model to show that macroscopic loss of ellipticity is connected to microbuckling. They argued in favor of using loss of ellipticity as a condition to have a well-posed problem as it does not assume a specific mode and does not imply a specific constitutive law. Furthermore it was demonstrated that a first gradient homogenization in conjunction with a classical Cauchy continuum at the macro scale cannot preserve the intrinsic length scale of the problem given by the fibre bending stiffness. As a result the macroscopic response becomes mesh-dependent after loss of ellipticity.

5.2. Structural effects and competition between damage mechanisms

Although a consistent constitutive model is necessary to perform meso- and higher-scale finite element analyses, it is not entirely sufficient. Actual composite structures exhibit a variety of effects that cannot easily be modelled at the constitutive level, including scale effects [46], unusually higher bending strength [106], and often a combination of microbuckling with ply-scale failure models such as transverse cracking and delamination [11]. In recent years, a number of multiscale approaches have been developed to tackle these challenges, although at an ever-increasing computational cost.

After an earlier micromechanical study of the through-the-thickness stress distribution in Ref. [107], Drapier and coworkers successively developed a dedicated multi-scale approach in Ref. [108]. Displacements were split into a slow component at a macroscopic FE length scale and a fast component at a smaller length scale. The latter relied on a very simple elastic-plastic microbuckling model and was discretized using Ritz shape functions. fibre misalignment was represented as an inhomogeneous field. This multiscale model was then used for a sensitivity analysis of material and structural properties in Ref. [109]. For a material corresponding to T300/914 carbon/epoxy, it was found that the peak load is sensitive to the initial misalignment wavelength, and

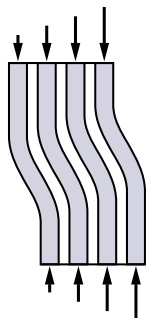


Fig. 15. Structural properties like bending loads, cut-outs, and similar cause stress gradients which have an effect on the microbuckling response.

not just the misalignment angle, outside a range of 0.3 – 0.6 mm. Regarding the misalignment angle, two failure scenarios were distinguished. For small initial misalignments, matrix plasticity develops evenly over the thickness due to stress redistributions, rapidly causing an instability. For larger misalignments, plasticity develops more heterogeneously and the fibre waviness progresses more smoothly up to a critical point. The authors also studied the influence of load gradients (Fig. 15), thickness effects, and stacking effects, confirming several earlier experimental findings. Concerning load gradients, bending was found to play a critical role in the predicted strength of the laminate. Indeed the strain at failure in pure bending was found quite higher – typically 50–100% – than in compression. This effect was actually found to dependent on ply thickness: The thinner the ply, the higher the bending failure strain. Conversely, compressive failure strain remains unaffected. Finally, this combined effect is also the most striking result of the stacking influence study: The key parameters for each unique stacking sequence is the total thickness of consecutive 0° plies and their load gradient through the thickness.

Using the same baseline micromodel as in Ref. [102], Prabhakar and Waas also studied the interaction of microbuckling with the two most frequent ply-scale failure modes: delamination and splitting [110]. Both these studies were therefore based on a plane strain 2D model and additionally featured cohesive zones at the discrete interfaces where the damage mechanisms of interest could occur. The authors studied size and stacking effects, although never under bending loading and therefore observed minimal influences. More significant was the sensitivity to the *laminate* waviness angle, considered in this study in addition to microscopic waviness, and to the cohesive parameters, departing from their experimental values. It was found that mode I (opening) strength and toughness had little influence on the mechanical response in compression, unlike mode II (shear) strength and toughness which could drastically change the response of the laminate. Further, laminate waviness appeared to have quite a similar effect to fibre waviness in microbuckling analyses, which was to be expected given the similarities between the two modelling approaches.

Following the identification of a ply-scale homogenized response in Ref. [99], Allix and coworkers implemented it in the framework of a hybrid discrete/continuous model [111], where micro-buckling could compete with transverse cracking and delamination in the response of complex samples [112]. The hybrid model used for this purpose discretizes the laminate in microscopic unit cells about as wide as the ply thickness, separated by potential failure interfaces on all sides. Discrete failure mechanisms are activated on these interfaces based on a finite fracture mechanics approach featuring a mixed strength-toughness criterion [113], while diffuse failure mechanisms – and plasticity – are considered homogeneous per unit cell. The width of these unit cells must therefore be small enough to represent transverse cracking saturation when all potential surfaces fail. The width of a kink-band being slightly smaller than such a value, it was possible to model compressive failure in such a model with minimal interference with the existing

design. The authors used it to show that the interactions between kinking and transverse cracking appear naturally thanks to the strain and stress distributions: e.g. fully failed kink-bands were always found saturated with transverse cracks, while localized transverse cracks (splitting) caused by notches or holes could act as a shielding mechanism, see Fig. 13(a), effectively delaying the initiation of microbuckling – and increasing strength – in some cases.

Going a step further, Bishara and coworkers [95] combined micro-mechanical and meso-mechanical models to study the interaction of microbuckling in 0° plies with other failure modes in neighbouring plies. The micro-mechanical model used for 0° plies [94] has already been discussed in §4, therefore the problem is technically three-dimensional but remains largely constrained in a 2D plane. The meso-mechanical model, representing neighbouring (*i.e.* non-microbuckling-prone plies), is a conventional elastic-plastic damage model that allows a significant reduction of the overall computational cost. With the combination of these models, separated by delaminating interfaces, the authors could analyze the response of balanced 5-ply and 16-ply laminates to compression loading. They observed the expected interaction of microbuckling with delamination and splitting, but also the ability of a kink-band to propagate through-the-thickness, by activating inter-fibre failure mechanisms in neighbouring plies through stress redistributions. Again, the combination between different failure modes appears naturally and preferably around kink-band initiation and stress concentration regions, as long as all mechanisms are explicitly described.

6. Summary and outlook

The purpose of this survey was to provide an overview of modelling approaches based on micromechanics to the problem of compressive failure in laminated composites. As reminded in §2, the theoretical understanding of the basic phenomena has been well developed for some time. However, theories considering individual mechanisms in isolation generally do not allow for predictive assessments, for the reasons elaborated in §2.8. Hence, the formulation of computational models drawing from these original micromechanics prompted a variety of approaches, generally purpose-made, depending of the specific aspect or question at hand. Some of which remain challenges up to this day. Three main categories of models, with their own sets of shared characteristics, have been investigated.

Semi-analytical models, based on uniaxial developments of formerly analytical equations, allowed the modelling of complex material nonlinearities while keeping the morphological description of the microstructure simple (*i.e.* the initial fibre misalignment and the ultimate kink-band). Most aimed at and allowed to produce strength envelopes and energy dissipation estimates in better accordance with experimental results, for reasonable values of fibre misalignment. The role of fibre – or composite – bending stiffness and issues pertaining to stability were also highlighted. Others offered a better understanding and predictability of the kink-band angle, which was an input parameter of earlier theories. The influence of the variability and associated spatial correlation of fibre misalignment on kink-band initiation was explored via smeared continuum models and suitably generated misalignment fields [55,81,82]. The smeared approach continues to receive attention [114], in particular to represent fibre waviness [54,115].

Explicit micro-models allowed to better understand effects associated with boundary conditions and damage mechanisms competing at the microscale – particularly compressive fibre failure [116] and fibre-matrix debonding. With the advancement of computational power and the increased availability and precision of X-ray tomography measurements, “image-based” models, *i.e.* models based on numerically reconstructed experimental morphologies, sometimes combined with *in-situ* measurements, are becoming a strong trend for a variety of applications including bone, porous metals, and woven composites. Their extension to fibre-scale microbuckling is likely to improve our

understanding of these intricate phenomena even more in the very near future.

Multiscale models bridge the ultimate gap between component-scale computations and micromechanics. Their generalization over the past twenty years has finally allowed structure-scale predictions, taking into account the influence of evolving multiaxiality, nonlinear stress redistributions, size effects, and the coupling of microbuckling with splitting and delamination. Their significant computational costs limits however their usage to small centimetric samples. But this should be enough to confront recent experiments which support the importance of structure-scale effects [117–120], thanks to complex geometries or loading cases, usually instrumented with full-field measurements.

As a final outlook, the reader should keep in mind that most if not all of these developments were considered in the framework of quasi-

static compression. Industrial reality usually involves repeated, cycled loadings, possibly leading to fatigue failure [121], as well as fast, up to shock wave loadings, in case of structural crash or high energy impact [122,123]. These domains of study and the multiscale problematics they raise, including the effects of fatigue damage mechanisms, associated stress redistributions, strain rate strengthening, couple stresses with microinertia, and the saturation of crack propagation at high speed, remain to be assessed for microbuckling. A notable exception is the question of creep, which has received significant attention over the years [124–126]. With the current level of predictions offered by quasi-static theories and supported by the generalization of high resolution and high frequency full field measurements, these open questions now appear within reach.

A Appendix

Fig. 16 shows a web-structure linking attributes frequently appearing together. Attributes are taken from 6 categories listed in the column heading: *Domain* specifies the geometrical extent of the model. *fibre/matrix* is one of: *smearred*, to indicate an anisotropic homogeneous medium, or *discrete*, for separate resolution of the constituents. *Continuum theory* is one of: *Cauchy*, for a standard medium, *Cosserat*, to indicate that the medium is enriched with rotational degrees of freedom, or *Cauchy + rebar*, to indicate embedded stiffening elements. *Material model* is one of: *deformation theory*, i.e. no internal variables, *incremental theory*, for plasticity and/or damage with state variables, and *IFF criterion*, for the failure envelope theories reviewed in §3.2. The initial *Misalignment* can be modelled as *uniform*, by *harmonic* functions, or *random*. The last category specifies the *Region* over which the misalignment extends, see also Fig. 10. Attributes not applicable to a category are omitted.

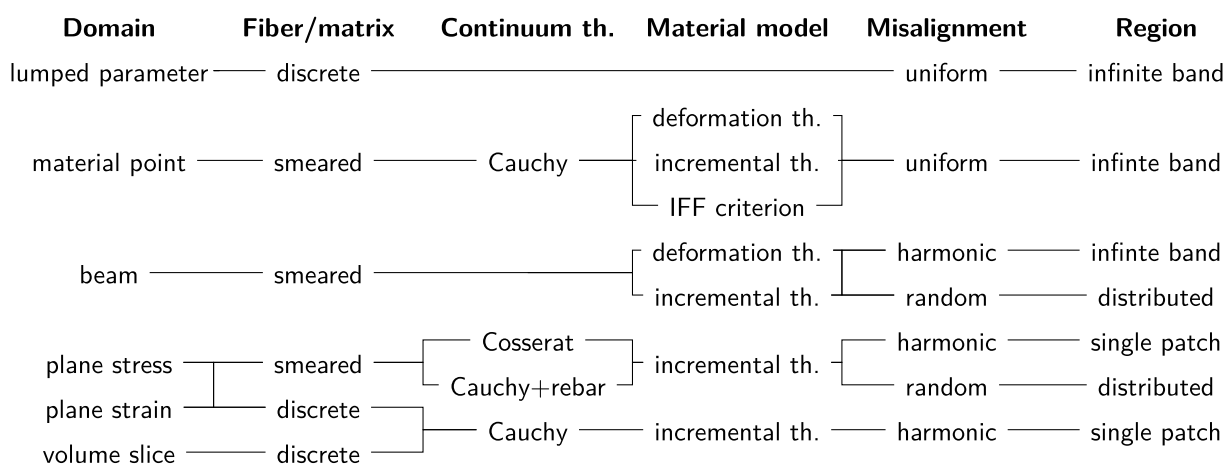


Fig. 16. Schematic overview of typically linked model attributes as a web-structure.

References

1. *Motivation and scope*

[1] B. Budiansky, N.A. Fleck, Compressive kinking of fibre composites: a topical review, *Appl. Mech. Rev.* 47 (6) (1994) S246–S270.
 [2] M.R. Piggott, The effect of fibre waviness on the mechanical properties of unidirectional fibre composites: a review, *Compos. Sci. Technol.* 53 (2) (1995) 201–205. *Mesostructures and Mesomechanics in Fibre Composites.*
 [3] C.R. Schultheisz, A.M. Waas, Compressive failure of composites, part i: testing and micromechanical theories, *Prog. Aero. Sci.* 32 (1) (1996) 1–42.
 [4] A.M. Waas, C.R. Schultheisz, Compressive failure of composites, part ii: experimental studies, *Prog. Aero. Sci.* 32 (1) (1996) 43–78.
 [5] C. Soutis, Failure of notched cfrp laminates due to fibre microbuckling: a topical review, *J. Mech. Behav. Mater.* 6 (August 1996) 309–330.

2. *Phenomenology and failure mechanisms*

[6] N.A. Fleck, Compressive failure of fibre composites, in: J.W. Hutchinson, T.Y. Wu (Eds.), *Advances in Applied Mechanics*, Academic Press, New York, NY, 1997, pp. 43–117 1948.
 [7] N.K. Naik, R.S. Kumar, Compressive strength of unidirectional composites: evaluation and comparison of prediction models, *Compos. Struct.* 46 (3) (1999) 299–308.

[8] S.T. Pinho, R. Gutkin, S. Pimenta, N.V. De Carvalho, P. Robinson, On longitudinal compressive failure of carbon-fibre-reinforced polymer: from unidirectional to woven, and from virgin to recycled, *Phil. Trans. Roy. Soc. Lond.: Math. Phys. Eng. Sci.* 370 (1965) (2012) 1871–1895.
 [9] B.W. Rosen, *fibre Composite Materials*, American Society for Metals, Metals Park, Ohio, 1965, p. 37.
 [10] M.R. Piggott, A theoretical framework for the compressive properties of aligned fibre composites, *J. Mater. Sci.* 16 (10) (Oct 1981) 2837–2845.
 [11] K. Oguni, C.Y. Tan, G. Ravichandran, Failure mode transition in unidirectional e-glass/vinylester composites under multiaxial compression, *J. Compos. Mater.* 34 (24) (2000) 2081–2097.
 [12] P. Prabhakar, A.M. Waas, Interaction between kinking and splitting in the compressive failure of unidirectional fibre reinforced laminated composites, *Compos. Struct.* 98 (Supplement C) (2013) 85–92.
 [13] S.H. Lee, A.M. Waas, Compressive response and failure of fibre reinforced unidirectional composites, *Int. J. Fract.* 100 (3) (Dec 1999) 275–306.
 [14] C.S. Yerramalli, A.M. Waas, A failure criterion for fibre reinforced polymer composites under combined compression–torsion loading, *Int. J. Solids Struct.* 40 (5) (2003) 1139–1164.
 [15] C. Soutis, N.A. Fleck, Static compression failure of carbon fibre t800/924c composite plate with a single hole, *J. Compos. Mater.* 24 (5) (1990) 536–558.
 [16] B. Budiansky, N.A. Fleck, Compressive failure of fibre composites, *J. Mech. Phys. Solids* 41 (1) (1993) 183–211.
 [17] H. Schuerch, Prediction of compressive strength in uniaxial boron fibre-metal

- matrix composite materials, *AIAA J.* 4 (1) (1966) 102–106.
- [18] A.S. Argon, Fracture of Composites, *Treatise of Material Science and Technology* vol. 1, (1972), pp. 79–114.
- [19] N. Triantafyllidis, W.C. Schnaidt, Comparison of microscopic and macroscopic instabilities in a class of two-dimensional periodic composites, *J. Mech. Phys. Solids* 41 (9) (1993) 1533–1565.
- [20] N.A. Fleck, L. Deng, B. Budiansky, Prediction of kink width in compressed fibre composites, *J. Appl. Mech.* 62 (2) (1995) 329–337.
- [21] B. Budiansky, *Micromechanics*, *Comput. Struct.* 16 (1) (1983) 3–12.
- [22] T.J. Vogler, S. Kyriakides, On the initiation and growth of kink bands in fibre composites: Part i. experiments, *Int. J. Solids Struct.* 38 (15) (2001) 2639–2651.
- [23] P.M. Moran, X.H. Liu, C.F. Shih, Kink band formation and band broadening in fibre composites under compressive loading, *Acta Metall. Mater.* 43 (8) (1995) 2943–2958.
- [24] C.R. Chaplin, Compressive fracture in unidirectional glass-reinforced plastics, *J. Mater. Sci.* 12 (2) (Feb 1977) 347–352.
- [25] B. Budiansky, N.A. Fleck, J.C. Amazigo, On kink-band propagation in fibre composites, *J. Mech. Phys. Solids* 46 (9) (1998) 1637–1653.
- [26] N.A. Fleck, B. Budiansky, Compressive failure of fibre composites due to microbuckling, in: George J. Dvorak (Ed.), *Inelastic Deformation of Composite Materials: IUTAM Symposium*, Troy, New York, May 29 – June 1, 1990, Springer New York, New York, NY, 1991, pp. 235–273.
- [27] S. Sivashanker, N.A. Fleck, M.P.F. Sutcliffe, Microbuckle propagation in a unidirectional carbon fibre-epoxy matrix composite, *Acta Mater.* 44 (7) (1996) 2581–2590.
- [28] N.A. Fleck, S. Sivashanker, M.P.F. Sutcliffe, Compressive failure of composites due to microbuckle growth, *Eur. J. Mech. A Solid.* 16 (1) (1997) 65–82.
- [29] R. Gutkin, S.T. Pinho, P. Robinson, P.T. Curtis, On the transition from shear-driven fibre compressive failure to fibre kinking in notched cfrp laminates under longitudinal compression, *Compos. Sci. Technol.* 70 (8) (2010) 1223–1231.
- [30] I. Vinçon, O. Allix, P. Sigety, M.-H. Auvray, Compressive performance of carbon fibres: experiment and analysis, *Compos. Sci. Technol.* 58 (10) (1998) 1649–1658.
- [31] P.S. Steif, A model for kinking in fibre composites - i. fibre breakage via microbuckling, *Int. J. Solids Struct.* 26 (5) (1990) 549–561.
- [32] J.M. Guimard, O. Allix, N. Pechnik, P. Thevenet, Statistical energy and failure analysis of cfrp compression behavior using a uniaxial microbuckling model, *J. Compos. Mater.* 41 (23) (2007) 2807–2828.
- [33] S. Pimenta, R. Gutkin, S.T. Pinho, P. Robinson, A micromechanical model for kink-band formation: Part i — experimental study and numerical modeling, *Compos. Sci. Technol.* 69 (7) (2009) 948–955.
- [34] S. Narayanan, L.S. Schadler, Mechanisms of kink-band formation in graphite/epoxy composites: a micromechanical experimental study, *Compos. Sci. Technol.* 59 (15) (1999) 2201–2213.
- [35] G.W. Hunt, Peletier MA, Wade MA, The maxwell stability criterion in pseudo-energy models of kink banding, *J. Struct. Geol.* 22 (5) (2000) 669–681.
- [36] G.M. Martinez, M.R. Piggott, D.M.R. Bainbridge, B. Harris, The compression strength of composites with kinked, misaligned and poorly adhering fibres, *J. Mater. Sci.* 16 (10) (Oct 1981) 2831–2836.
- [37] Wung ECJ, S.N. Chatterjee, On the failure mechanisms in laminate compression specimens and the measurement of strengths, *J. Compos. Mater.* 26 (13) (1992) 1885–1914.
- [38] J. Lankford, Compressive failure of fibre-reinforced composites: buckling, kinking, and the role of the interphase, *J. Mater. Sci.* 30 (17) (Sep 1995) 4343–4348.
- [39] B.D. Garland, I.J. Beyerlein, L.S. Schadler, The development of compression damage zones in fibrous composites, *Compos. Sci. Technol.* 61 (16) (2001) 2461–2480.
- [40] J. Bai, S.L. Phoenix, Compressive failure model for fibre composites by kink band initiation from obliquely aligned, shear-dislocated fibre breaks, *Int. J. Solids Struct.* 42 (7) (2005) 2089–2128.
- [41] J.L. Wind, A.M. Waas, H.M. Jensen, Initiation of failure at notches in unidirectional fibre composites, *Compos. Struct.* 122 (Supplement C) (2015) 51–56.
- [42] E.G. Guynn, W.L. Bradley, W. Elber, *Micromechanics of Compression Failures in Open Hole Composite Laminates*. *Composite Materials: Fatigue and Fracture Second* (1989), p. 118 1012.
- [43] C. Soutis, N.A. Fleck, P.A. Smith, Failure prediction technique for compression loaded carbon fibre-epoxy laminate with open holes, *J. Compos. Mater.* 25 (11) (1991) 1476–1498.
- [44] C. Soutis, P.T. Curtis, N.A. Fleck, Compressive failure of notched carbon fibre composites, *Proc. Roy. Soc. Lond.: Math. Phys. Eng. Sci.* 440 (1993) 241–256 1909.
- [45] S.T. Pinho, P. Robinson, L. Iannucci, Fracture toughness of the tensile and compressive fibre failure modes in laminated composites, *Compos. Sci. Technol.* 66 (13) (2006) 2069–2079.
- [46] Z.P. Bažant, J.-J.H. Kim, I.M. Daniel, E. Becq-Giraudon, G. Zi, Size effect on compression strength of fibre composites failing by kink band propagation, *Int. J. Fract.* 95 (1) (1999) 103–141.
- [47] J. Lee, C. Soutis, Measuring the notched compressive strength of composite laminates: specimen size effects, *Compos. Sci. Technol.* 68 (12) (2008) 2359–2366 Deformation and Fracture of Composites: Analytical, Numerical and Experimental Techniques, with regular papers.
- [48] Z.P. Bažant, Size effect on structural strength: a review, *Arch. Appl. Mech.* 69 (9) (Nov 1999) 703–725.
- [49] A. Carpinteri, Decrease of apparent tensile and bending strength with specimen size: two different explanations based on fracture mechanics, *Int. J. Solids Struct.* 25 (4) (1989) 407–429.
- [50] M.R. Wisnom, Size effects in the testing of fibre-composite materials, *Compos. Sci. Technol.* 59 (13) (1999) 1937–1957.
- [51] Z.P. Bažant, Y. Xi, S.G. Reid, Statistical size effect in quasi-brittle structures: I. is weibull theory applicable? *J. Eng. Mech.* 117 (11) (1991) 2609–2622.
- [52] B. Paluch, Analysis of geometric imperfections affecting the fibres in unidirectional composites, *J. Compos. Mater.* 30 (4) (1996) 454–485.
- [53] S.W. Yurgartis, Measurement of small angle fibre misalignments in continuous fibre composites, *Compos. Sci. Technol.* 30 (4) (1987) 279–293.
- [54] D. Wilhelmsson, R. Gutkin, F. Edgren, LE Asp, An experimental study of fibre waviness and its effects on compressive properties of unidirectional ncf composites, *Compos. Appl. Sci. Manuf.* 107 (2018) 665–674.
- [55] M.P.F. Sutcliffe, modeling the effect of size on compressive strength of fibre composites with random waviness, *Compos. Sci. Technol.* 88 (Supplement C) (2013) 142–150.

3. Semi-analytical models

- [56] Wade MA, C. Völlmecke, J.F. Haley, S. Yiatros, Geometric modeling of kink banding in laminated structures, *Phil. Trans. Roy. Soc. Lond.: Math. Phys. Eng. Sci.* 370 (1965) (2012) 1827–1849.
- [57] RAE Zidek, C. Völlmecke, On the influence of material non-linearities in geometric modeling of kink band instabilities in unidirectional fibre composites, *Int. J. Non-Linear Mech.* 62 (Supplement C) (2014) 23–32.
- [58] C. Völlmecke, RAE Zidek, Geometric modeling of kink banding in multidirectional composites, *J. Eng. Math.* 95 (1) (Dec 2015) 173–191.
- [59] A Balacó De Morais, A.T. Marques, A micromechanical model for the prediction of the lamina longitudinal compression strength of composite laminates, *J. Compos. Mater.* 31 (14) (1997) 1397–1412.
- [60] S. Pimenta, R. Gutkin, S.T. Pinho, P. Robinson, A micromechanical model for kink-band formation: Part ii—analytical modeling, *Compos. Sci. Technol.* 69 (7) (2009) 956–964.
- [61] P. Davidson, A.M. Waas, Mechanics of kinking in fibre-reinforced composites under compressive loading, *Math. Mech. Solids* 21 (6) (2016) 667–684.
- [62] N. Feld, O. Allix, E. Baranger, J.-M. Guimard, Micro-mechanical prediction of ud laminates behavior under combined compression up to failure: influence of matrix degradation, *J. Compos. Mater.* 45 (22) (2011) 2317–2333.
- [63] A Balacó De Morais, modeling lamina longitudinal compression strength of carbon fibre composite laminates, *J. Compos. Mater.* 30 (10) (1996) 1115–1131.
- [64] A Balacó De Morais, Prediction of the layer longitudinal compression strength, *J. Compos. Mater.* 34 (21) (2000) 1808–1820.
- [65] S. Kyriakides, E.J. Perry, K.M. Liechti, Instability and failure of fibre composites in compression, *Appl. Mech. Rev.* 47 (6 part 2) (1994) S262.
- [66] S. Kyriakides, R. Arsecularatne, E.J. Perry, K.M. Liechti, On the compressive failure of fibre reinforced composites, *Int. J. Solids Struct.* 32 (6) (1995) 689–738. Time Dependent Problems in Mechanics.
- [67] T.J. Vogler, S.-Y. Hsu, S. Kyriakides, Composite failure under combined compression and shear, *Int. J. Solids Struct.* 37 (12) (2000) 1765–1791.
- [68] G. Eyer, O. Montagnier, C. Hochard, J.-P. Charles, Effect of matrix damage on compressive strength in the fibre direction for laminated composites, *Compos. Appl. Sci. Manuf.* 94 (2017) 86–92.
- [69] C.G. Dávila, P.P. Camanho, Failure criteria for frp laminates in plane stress, *NASA TM 212663* (613) (2003).
- [70] S.T. Pinho, L. Iannucci, P. Robinson, Physically-based failure models and criteria for laminated fibre-reinforced composites with emphasis on fibre kinking: Part i: Development, *Compos. Appl. Sci. Manuf.* 37 (1) (2006) 63–73.
- [71] P.P. Camanho, A. Arteiro, A.R. Melro, G. Catalanotti, M. Vogler, Three-dimensional invariant-based failure criteria for fibre-reinforced composites, *Int. J. Solids Struct.* 55 (Supplement C) (2015) 92–107.
- [72] A. Puck, H. Schürmann, Failure analysis of frp laminates by means of physically based phenomenological models, *Compos. Sci. Technol.* 58 (7) (1998) 1045–1067.
- [73] M. Knops, Analysis of Failure in fibre Polymer Laminates: the Theory of Alfred Puck, Springer Science & Business Media, 2008.
- [74] M. Vogler, R. Rolfes, P.P. Camanho, Modeling the inelastic deformation and fracture of polymer composites - part i: plasticity model, *Mech. Mater.* 59 (2013) 50–64.
- [75] P.P. Camanho, Bessa MA, G. Catalanotti, M. Vogler, R. Rolfes, Modeling the inelastic deformation and fracture of polymer composites - part II: smeared crack model, *Mech. Mater.* 59 (2013) 36–49.
- [76] R.A. Schapery, Prediction of compressive strength and kink bands in composites using a work potential, *Int. J. Solids Struct.* 32 (6) (1995) 739–765. Time Dependent Problems in Mechanics.
- [77] S. Basu, A.M. Waas, D.R. Ambur, Compressive failure of fibre composites under multi-axial loading, *J. Mech. Phys. Solids* 54 (3) (2006) 611–634.
- [78] S. Basu, A.M. Waas, D.R. Ambur, Prediction of progressive failure in multi-directional composite laminated panels, *Int. J. Solids Struct.* 44 (9) (2007) 2648–2676.
- [79] W.S. Slaughter, N.A. Fleck, Microbuckling of fibre composites with random initial fibre waviness, *J. Mech. Phys. Solids* 42 (11) (1994) 1743–1766.
- [80] N.A. Fleck, J.Y. Shu, Microbuckle initiation in fibre composites: a finite element study, *J. Mech. Phys. Solids* 43 (12) (1995) 1887–1918.
- [81] S.L. Lemanski, M.P.F. Sutcliffe, Compressive failure of finite size unidirectional composite laminates with a region of fibre waviness, *Compos. Appl. Sci. Manuf.* 43 (3) (2012) 435–444.
- [82] D. Liu, N.A. Fleck, M.P.F. Sutcliffe, Compressive strength of fibre composites with random fibre waviness, *J. Mech. Phys. Solids* 52 (7) (2004) 1481–1505.
- [83] A.R. Clarke, G. Archenhold, N.C. Davidson, W.S. Slaughter, N.A. Fleck,

Determining the power spectral density of the waviness of unidirectional glass fibres in polymer composites, *Appl. Compos. Mater.* 2 (4) (Jul 1995) 233–243.

4. Explicit micromechanical models

- [84] N. Triantafyllidis, S. Bardenhagen, The influence of scale size on the stability of periodic solids and the role of associated higher order gradient continuum models, *J. Mech. Phys. Solids* 44 (11) (1996) 1891–1928.
- [85] M. Romanowicz, Initiation of kink bands from regions of higher misalignment in carbon fibre-reinforced polymers, *J. Compos. Mater.* 48 (19) (2014) 2387–2399.
- [86] S.-Y. Hsu, T.J. Vogler, S. Kyriakides, Compressive strength predictions for fibre composites, *J. Appl. Mech.* 65 (1) (1998) 7–16.
- [87] T.J. Vogler, S.-Y. Hsu, S. Kyriakides, On the initiation and growth of kink bands in fibre composites. Part II: analysis, *Int. J. Solids Struct.* 38 (15) (2001) 2653–2682.
- [88] S.-Y. Hsu, T.J. Vogler, S. Kyriakides, On the axial propagation of kink bands in fibre composites: Part II analysis, *Int. J. Solids Struct.* 36 (4) (1999) 575–595.
- [89] C.S. Yerramalli, A.M. Waas, The effect of fibre diameter on the compressive strength of composites—a 3d finite element based study, *Comput. Model. Eng. Sci.* 6 (2004) 1–16.
- [90] J.L. Wind, S. Steffensen, H.M. Jensen, Comparison of a composite model and an individually fibre and matrix discretized model for kink band formation, *Int. J. Non-Linear Mech.* 67 (2014) 319–325.
- [91] H.M. Jensen, J. Christoffersen, Kink band formation in fibre reinforced materials, *J. Mech. Phys. Solids* 45 (7) (1997) 1121–1136.
- [92] Y. Lapusta, J. Harich, W. Wagner, Three-dimensional fe model for fibre interaction effects during microbuckling in composites with isotropic and anisotropic fibres, *Commun. Numer. Methods Eng.* 24 (12) (12 2008) 2206–2215.
- [93] J. Harich, Y. Lapusta, W. Wagner, 3d fe-modeling of surface and anisotropy effects during micro-buckling in fibre composites, *Compos. Struct.* 89 (4) (2009) 551–555.
- [94] M. Bishara, R. Rolfes, O. Allix, Revealing complex aspects of compressive failure of polymer composites – part i: fibre kinking at microscale, *Compos. Struct.* 169 (Supplement C) (2017) 105–115 In Honor of Prof. Leissa.
- [95] M. Bishara, M. Vogler, R. Rolfes, Revealing complex aspects of compressive failure of polymer composites – part ii: failure interactions in multidirectional laminates and validation, *Compos. Struct.* 169 (Supplement C) (2017) 116–128 In Honor of Prof. Leissa.
- [96] R. Gutkin, S.T. Pinho, P. Robinson, P.T. Curtis, Micro-mechanical modeling of shear-driven fibre compressive failure and of fibre kinking for failure envelope generation in cfrp laminates, *Compos. Sci. Technol.* 70 (8) (2010) 1214–1222.
- [105] S. Nezamabadi, J. Yvonnet, H. Zahrouni, M. Potier-Ferry, A multilevel computational strategy for handling microscopic and macroscopic instabilities, *Comput. Methods Appl. Mech. Eng.* 198 (27) (2009) 2099–2110.
- [106] M.R. Wisnom, On the high compressive strains achieved in bending tests on unidirectional carbon-fibre/epoxy, *Compos. Sci. Technol.* 43 (3) (1992) 229–235.
- [107] S. Drapier, C. Gardin, J.-C. Grandidier, M. Potier-Ferry, Structure effect and microbuckling, *Compos. Sci. Technol.* 56 (7) (1996) 861–867 9th French National Colloquium on Composite Materials.
- [108] S. Drapier, J.-C. Grandidier, M. Potier-Ferry, Towards a numerical model of the compressive strength for long fibre composites, *Eur. J. Mech. A Solid.* 18 (1) (1999) 69–92.
- [109] S. Drapier, J.-C. Grandidier, M. Potier-Ferry, A structural approach of plastic microbuckling in long fibre composites: comparison with theoretical and experimental results, *Int. J. Solids Struct.* 38 (22) (2001) 3877–3904.
- [110] P. Prabhakar, A.M. Waas, Micromechanical modeling to determine the compressive strength and failure mode interaction of multidirectional laminates, *Compos. Appl. Sci. Manuf.* 50 (Supplement C) (2013) 11–21.
- [111] P. Ladevèze, G. Lubineau, D. Violeau, A computational damage micromodel of laminated composites, *Int. J. Fract.* 137 (1) (Jan 2006) 139–150.
- [112] O. Allix, N. Feld, E. Baranger, J.-M. Guimard, C. Ha-Minh, The compressive behaviour of composites including fibre kinking: modeling across the scales, *Meccanica* 49 (11) (Nov 2014) 2571–2586.
- [113] D. Leguillon, Strength or toughness? a criterion for crack onset at a notch, *Eur. J. Mech. A Solid.* 21 (1) (2002) 61–72.

6. Summary and outlook

- [114] A.D. Hasanyan, A.M. Waas, Compressive failure of fibre composites: a homogenized, mesh-independent model, *J. Appl. Mech.* 85 (9) (June 2018) 091001–091001–15.
- [115] N. Safdar, B. Daum, R. Rolfes, Stochastic compressive failure surface modeling for the unidirectional fibre reinforced composites under plainstress, 6th European Conference on Computational Mechanics, Glasgow, 2018.
- [116] I.P. Kumar, P.M. Mohite, S. Kamle, Axial compressive strength testing of single carbon fibres, *Arch. Mech.* 65 (1) (2013) 27–43.
- [117] M.R. Wisnom, S.R. Hallett, C. Soutis, Scaling effects in notched composites, *J. Compos. Mater.* 44 (2) (2010) 195–210.
- [118] S. Hernandez, F. Sket, C. Gonzalez, J. Molina, J. Llorca, Experimental assessment of processing defects on the mechanical properties of a composite material by x-ray tomography, in: R. Rolfes, E.L. Jansen (Eds.), Proceedings of the 3rd ECCOMAS Thematic Conference on the Mechanical Response of Composites, Leibniz Universität Hannover, 2011, pp. 43–49.
- [119] W. Sun, A.P. Vassilopoulos, T. Keller, Experimental investigation of kink initiation and kink band formation in unidirectional glass fibre-reinforced polymer specimens, *Compos. Struct.* 130 (2015) 9–17.
- [120] P. Davidson, A.M. Waas, The effects of defects on the compressive response of thick carbon composites: an experimental and computational study, *Compos. Struct.* 176 (2017) 582–596.
- [121] F. Lahuerta, R.P.L. Nijssen, F.P. van der Meer, L.J. Sluys, Thickness scaled compression tests in unidirectional glass fibre reinforced composites in static and fatigue loading, *Compos. Sci. Technol.* 123 (2016) 115–124.
- [122] A.F. Johnson, D. Kohlgrüber, Design and performance of energy absorbing sub-floor structures in aerospace applications, IMechE Seminar S672, 2000.
- [123] Israr HA, S. Rivallant, J.J. Barrau, Experimental investigation on mean crushing stress characterization of carbon-epoxy plies under compressive crushing mode, *Compos. Struct.* 96 (2013) 357–364.
- [124] W.S. Slaughter, N.A. Fleck, B. Budiansky, Compressive failure of fibre composites: the roles of multiaxial loading and creep, *J. Eng. Mater. Technol.* 115 (July 1993) 308–313.
- [125] M.G. Violette, R.A. Schapery, Time-dependent compressive strength of unidirectional viscoelastic composite materials, *Mech. Time-Dependent Mater.* 6 (2) (Jun 2002) 133–145.
- [126] A. Vinet, D. Gamby, Prediction of long-term mechanical behaviour of fibre composites from the observation of micro-buckling appearing during creep compression tests, *Compos. Sci. Technol.* 68 (2) (2008) 526–536.

Chapter III.

A numerical investigation of the statistical size-effect in non-crimp fabric laminates under homogeneous compressive loads

In this chapter, the scale laws governing the reduction of compressive strength with increasing specimen size are investigated by numerical means. Several main concepts of the approach were already briefly discussed in the introduction, see Subsec. 1.4.3. The material under consideration features a mesoscale architecture, and the characteristic of the resulting misalignment topology have already been briefly discussed in Subsec. 1.3.2. Roving misalignment data obtained was obtained via large scale measurements and formed the basis for a misalignment quantification via the spectral representation method, see Subsec. 1.3.5. The topic of statistically informed microscale approaches introduced in Subsec. 1.3.3 is also revisited here.

This chapter was published as an article and the respective reference is stated below. The first author developed the scientific concept of the approach, provided the computer implementation, performed all simulations and wrote the manuscript.

B. Daum, G. Gottlieb, N. Safdar, M. Brod, J.-H. Ohlendorf, and R. Rolfes.

A numerical investigation of the statistical size-effect in non-crimp fabric laminates under homogeneous compressive loads. Journal of Composite Materials, 2021.

A numerical investigation of the statistical size effect in non-crimp fabric laminates under homogeneous compressive loads

Benedikt Daum¹ , Gerrit Gottlieb¹, Nabeel Safdar¹, Martin Brod¹, Jan-Hendrik Ohlendorf²  and Raimund Rolfes¹

Abstract

The compressive strength of fiber reinforced composites is typically limited by a shear localization phenomenon known as microbuckling and is very sensitive to local imperfections of fiber alignment. Local misalignments act as randomly distributed flaws and introduce a dependence of the compressive strength on the size of material volume element under consideration. For homogeneously loaded material elements, weakest-link theory in combination with a Weibull power law is a frequently employed statistical model for microbuckling strength. This implies a dependence of strength on the size of volume under consideration. The present contribution investigates the strength–size relation for a non-crimp fabric via a numerical approach. Characteristics of the misalignment flaws used in simulations are derived from a comprehensive data set collected via large-scale measurements of roving dislocations on dry fiber material. Predictions resulting from the weakest-link Weibull theory are compared against strength–size statistics gathered by numerical analysis. In this manner, the size effects in single plies and laminates are quantified. The main findings are that weakest-link Weibull theory is well suited to predict size related strength loss in individual plies. However, it is also found that when plies are bonded to form laminates, misalignments in individual plies are mitigated in a way that is inconsistent with the weakest-link assumption. In all situations considered here, the strength loss expected from weakest-link Weibull theory was outweighed by a strength increase due to the mitigation effect when the volume was increased by adding extra layers to a laminate.

Keywords

A polymer-matrix composites, B nonlinear behaviour, B strength, C buckling, C computational mechanics

1. Introduction

For a large class of composites comprising stiff fibers bonded by a compliant matrix, the strength under predominantly compressive loading is limited by a mechanism known as microbuckling or fiber kinking in the literature. Here, the former term or its abbreviation MB is used. MB is strongly linked to preexisting imperfections of fiber alignment and to matrix shear nonlinearity. As a mode of failure, it leads to a reduction in the applicable far field compressive stress due to rotation and subsequent fracture of fibers within a small band of localized shear deformation. It is initiated when the geometrical softening due to small pre-failure deformations outpaces the material hardening in the incipient shear band.^{1–3} In the interest of brevity, no extensive discussion of general aspects of MB is included here. For a comprehensive exposition of the basic mechanisms and closed-form analysis,^{1,3} experimental techniques,⁴ and computational approaches,^{5,6} the reader may refer to the cited literature reviews.

1.1 The statistical size effect and associated scaling law

In the presence of local stress concentrations, MB may progress with increasing load in a quasistatic manner due to stress redistribution.^{7,8} In homogeneously loaded panels, however, redistribution is insubstantial and initiation of MB at a local point leads to immediate sudden collapse in a transient dynamic manner. In the latter situation, several experimental investigations^{9–11} reported that MB-strength

¹Institute of Structural Analysis, Leibniz Universität Hannover, Hannover, Germany

²Institute for Integrated Product Development (BIK), University of Bremen, Bremen, Germany

Corresponding author:

Benedikt Daum, Institute of Structural Analysis, Leibniz Universität Hannover, Appelstraße 9A Hannover 30167, Germany. Email. b.daum@isd.uni-hannover.de

decreases with increasing coupon size. However, compressive testing is notoriously difficult, and inconclusive results were reported as well.¹² Nevertheless, for specimens under homogeneous compressive stress, a decrease of strength with increasing volume is expected due to stochastic considerations.^{12–14} To distinguish this effect from other mechanisms which produce a different kind of size effect in notched, that is, in-homogeneously loaded specimens, it is designated the statistical size effect.

The stochastic arguments that lead to the prediction of the statistical size effect in MB problems are very similar to the reasoning applied to the well understood size effect in ceramics and other brittle materials with random flaws. In brittle materials, failure initiation in any particular location triggers catastrophic failure propagation, that is, the overall strength is limited by the strength of the weakest element. The statistical size effect then arises from the increased chance of encountering more extreme imperfections in larger specimen volumes. For a weakest-link model, the probability of survival P of a volume V with respect to the applied far field compressive stress $\bar{\sigma}_{11}$ is given by (1). There, P_0 is the survival probability in some reference volume V_0 .

$$P(\bar{\sigma}_{11}) = \exp \left[\int_V \ln(P_0(\bar{\sigma}_{11})) \frac{dV}{V_0} \right] \quad (1)$$

To complete the model, a further assumption regarding $P_0(\bar{\sigma}_{11})$ is required, which is distinct from the previously discussed weakest-link model.¹⁵ For this purpose, a power law proposed by Weibull is typically employed (2); however, this assumption is not based on any physical arguments, and the suitability of such a model is frequently questioned.^{16,17} There, R_0 and m are the scale and shape parameters of the Weibull distribution and the symbol R_t refers to an optional third parameter which specifies a minimum threshold strength below which probability of failure is zero. For the 3-parameter variant of the Weibull distribution, R_t is positive and the 2-parameter variant is obtained by setting the threshold to zero. The angled brackets denote Macauley brackets, that is, $\langle x \rangle = x$ if $x > 0$ else $x = 0$.

$$P_0(\bar{\sigma}_{11}) = \exp \left[- \left\langle \frac{\bar{\sigma}_{11} - R_t}{R_0} \right\rangle^m \right] \quad (2)$$

By combining the weakest-link model and the Weibull power law assumptions, expression (3) is obtained.

$$P(\bar{\sigma}_{11}) = \exp \left[- \int_V \left\langle \frac{\bar{\sigma}_{11} - R_t}{R_0} \right\rangle^m \frac{dV}{V_0} \right] \quad (3)$$

For a homogeneously applied far field stress $\bar{\sigma}_{11}$, equation (3) implies the scaling law (4). To arrive at this

equation, the strengths R_1 and R_2 referring to same probability of survival, but different specimen volumes V_1 and V_2 , respectively, are introduced. Writing (3) for each $\bar{\sigma}_{11} = R_i$ and $V = V_i$ with $i = 1, 2$ and subsequently equating the probability yields (4). From a known strength R_1 determined for a particular Volume V_1 and a certain survivability P , a new strength R_2 of the same survivability but a different specimen size V_2 can be determined from the scaling law

$$\frac{R_2 - R_t}{R_1 - R_t} = \left(\frac{V_2}{V_1} \right)^{-1/m} \quad (4)$$

Experimental investigations of the size effect and scaling law are costly due to the large number and large size of specimens required for this purpose. Moreover, the strong sensitivity of MB to even small additional misalignment introduced during manufacturing or handling of specimens makes compressive testing a very delicate affair. Virtual testing via computational methods offers an alternative approach to investigate size effects within the controlled setting of numerical analysis. The amount of virtual tests is limited only by the numerical efficiency of the model; thus, the size effect may be identified by simply solving a large number of models with individual misalignment topologies and different domain sizes in a Monte-Carlos style approach. One of the main challenges in this approach is the proper and efficient representation of misalignment flaws in the models.

1.2. Misalignment representation in computational approaches

Computational modelling of MB must provide adequate representation of fiber misalignment flaws and matrix shear nonlinearity. Approaches to this problem may be roughly categorized into two groups: micromechanical models, see, for example, refs. 18–21, and homogenized models, for example, refs. 22–24. Micromechanical approaches resolve the constituents and microstructure of the composite; thus, misalignment and matrix response can be modelled directly. Effective or apparent properties of the composite at a larger length scale emerge naturally from the model. Hence, micromechanical approaches require relatively few abstractions or assumptions. A disadvantage of micromechanical approaches is that the discretization must be fine enough to represent microscale details like individual fibers. This results in a large computational effort and causes complications with automatic mesh generation techniques. In Monte-Carlo type investigations, large numbers of simulations must be solved and handled automatically; thus, the aforementioned shortcomings render micromechanical models impractical for all but very small microscale domain sizes. As an alternative, homogenized approaches take a standpoint at mesoscale. There, the fiber-matrix

microstructure is smeared out and represented indirectly via a homogeneous solid of effectively equivalent response. Matrix nonlinearity is accounted for by adjusting the shear response of the equivalent solid, and misalignments are treated by rotating its principal axes. Thus, more abstraction is required in the formulation of homogenized models for the benefit of decoupling the discretization size from the microstructure. Micromechanical approaches usually include only a single patch of misalignment.^{18,19} Homogenized models are less restricted with respect to size and may cover a spatial domain several times the size of the typical wavelength of misalignment undulations.

1.3. Measurement and quantification of misalignment

In order to build numerical models with realistic representations of the fiber misalignment, measurement and proper quantification of the apparently random properties of the misalignment topology is essential. In this spirit, several authors have gathered statistical data of misalignments and the proliferation of lab-sized X-ray computer tomography equipment triggered a rapid development in this field. For unidirectional carbon fiber composites, a variety of methods to determine in-situ misalignment angles via automated processing from volumetric grey-scale imaging data has been developed recently, see, for example, refs. 25 and 26, to cite just a few. In unidirectional fiber materials with simple architecture, misalignments are mostly due to random imperfections resulting from handling or processing. The situation is somewhat different for non-crimp fabric (NCF) materials with an elaborate mesoscale architecture, where stitching yarns or other bindings are used to bundle fibers into distinct rovings. The stitching results in an inherent, and somewhat regular, undulation of the predominant roving direction. Considering several NCF-materials, Wilhelmsson al.^{27,28} used image processing techniques to acquire misalignment data from optical images of micrographs to investigate the out-of-plane waviness characteristics.

The results of such measurements are typically presented in terms of empirical or fitted misalignment distributions. However, on their own, such misalignment distributions, in the statistical sense of the word, are not sufficient for the reconstruction of realistic misalignment topologies in numerical models. If the local misalignment of each grid point in the finite element mesh is determined by independently sampling from the misalignment distribution, a spurious mesh dependence is introduced. This is because in the measured misalignment topology, the misalignment field is smooth and the misalignments of nearby measurement points are related. Hence, the autocorrelation length has been found to be a very important statistical property to characterize misalignment topologies.^{23,29} This property

provides a measure of the minimum distance between points that have independent misalignments. Points that are closer than this distance have an (auto-) correlated misalignment, that is, their misalignment is not completely independent. Some authors^{23,30} proposed a characterization of the misalignment undulations in terms of their power spectrum in the frequency domain. This method provides a pertinent encoding of both misalignment distribution and autocorrelation properties.

1.4. Motivation

The brief review discussed so far motivates the present contribution to consolidate and extend earlier efforts with regard to these aspects:

- (i) The observed size effect in physical or virtual specimens with unsupported edges is not necessarily caused by the volume related statistical size effect elaborated in §1.1. In the presence of unsupported edges, MB is likely to be initiated there first before initiation can occur in the interior. This particular situation was considered in ref. 29 with the specific intention to quantify the effect of unsupported model edges on the compressive strength. Thus, volume related and edge related effects compete in specimens with unsupported edges, and it is not clear in advance if either effect is dominant. The present investigation is concerned with size effects resulting from a change in material reference volume only, and any lateral unsupported edges are avoided to isolate this effect. Hence, virtual specimens in the present contribution are taken as periodic unit cells embedded in surrounding material.
- (ii) Prior investigations regarding the size effect generally refer to unidirectional carbon fiber materials, see numerical investigations^{23,29} and experimental investigations.^{9–12} Although there is a comprehensive literature concerned with other aspects of MB in NCF-materials, it seems that the statistical size effect, as defined in §1.1, has not yet been considered for NCF-materials, in particular. It is discussed in the following, that the mesoscale roving architecture of NCF-materials results in some peculiarities, that are not present in unidirectional materials.
- (iii) As evident from the review §1.2 and §1.3, realistic modelling of the misalignment topology is critical for numerical MB-strength predictions. The misalignment topology in the present contribution is derived from a large-scale measurement of roving undulation which provides a wide statistical basis for the generation of realistic misalignment topologies, see §2.1 and §2.2.

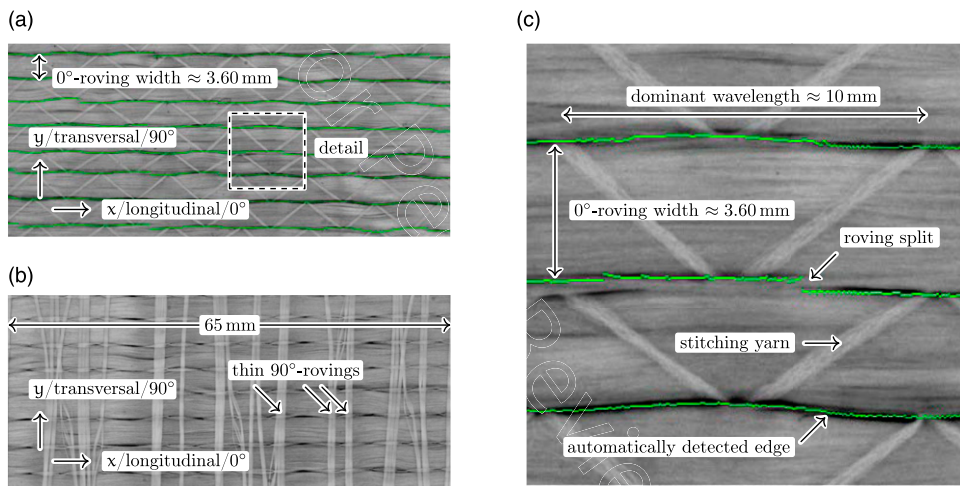


Figure 1. Images of the front (a) and reverse (b) sides of the dry textile. A magnified detail of the front side is shown in (c). Green pixels indicate the automatically detected edge and provide sampling points for the 0°-roving edge. Images courtesy of A. Miene/Faserinstitut Bremen.

(iv) Earlier numerical approaches reviewed above generally considered a single misalignment field in a 2-dimensional setting. Thus, the results may be interpreted as pertaining to the size effect in single plies, rather than multi-ply laminates. The present contribution considers a simple model for the interaction of ply-specific misalignment topologies in the laminate, see §2.4. It is shown in §3.2 that the bonding of individual plies to laminates has a significant effect on the strength–size relation and outweighs the statistical size effect in some situations.

2. Measurements and modelling

2.1. Fiber material and misalignment measurements

Misalignment data used in the investigation presented here was acquired via measurements on nominally unidirectional dry NCF-fiber material. All measurements were done on single plies resting on a rigid flat surface. In most applications, moulds are not flat and require some draping which leads to further roving dislocations and roving deformations. Moreover, measurements were performed on single uncompacted plies; hence, nesting, that is, further roving dislocations resulting from the compaction pressure, is also not considered. The type code of the material is [G;1134; 0°//G;36;90°][PES;12;L]¹, where the letter G indicates glass fiber and 1134/36 are the area weights in g/m². The 90°-rovings exist as somewhat irregularly arranged thin fiber strands. Due to the relatively small area weight of the 90°-rovings, the fiber material is considered nominally unidirectional. A plan view photo of the fiber material is shown in Figure 1. Both 0° and 90°rovings are bonded by a polyester

stitching yarn [PES;12;L] in tricot-stitch, which is the main source of undulation.

In order to enable large-area scans of the textile surface, an automated material unwinding unit³¹ was combined with a recording unit for textile surfaces. The textile was unrolled discontinuously in longitudinal direction in 60 mm steps. After each unrolling step, a robot arm mounted camera took a series of orthogonal images along the transversal direction. These images cover an area of 65 mm×65 mm with a resolution of 1 Pixel per 31.6 μm, see Figure 1(a) for an example. Images were subsequently joined in post-processing to cover a length of approximately 10 000 mm and a width of approximately 300 mm. From the image data the roving edge position was determined via an automatic edge detection algorithm. This yields a raw data set comprising about 320 000 sampling points for the lateral position along the nominal 0°-direction for each of the 83 rovings in the textile. Sampling points of the raw data set are marked in green, see Figure 1(c).

As apparent from Figure 1, the stitching yarn produces a 0°-roving undulation in the longitudinal direction with a relatively constant wavelength. This is due to the textile manufacturing process, where the stitching bond is produced via a rigid sewing mechanism. The stitching undulation occurs simultaneous with other imperfections. Occasionally, stitching does not occur at the boundary between rovings, and instead splits off a certain amount of filaments from one roving which then merge with the neighbouring roving. This situation typically appears as a discontinuous jump in the mutual edge of the involved rovings, see annotation ‘roving split’ in Figure 1(c). It appears that the presence of these measurement artifacts leads to some overestimation of the roving undulation, ramifications and remedies are discussed in §2.2

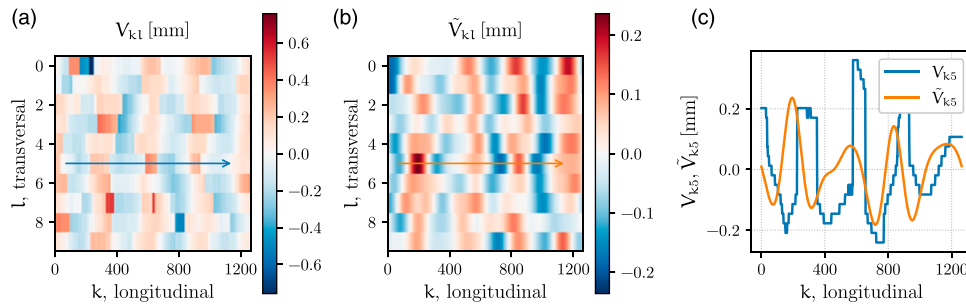


Figure 2. Lateral roving edge displacement fields for a domain of length $a = 40$ mm and width $b = 36.0$ mm. Index k counts the axial position in pixels and index l the roving edges. Measured displacement V_{kl} and modified displacement \tilde{V}_{kl} are shown in (a) and (b), respectively. To make differences more apparent, both are also drawn for $l = 5$ in (c). Notice that V_{k5} jumps when k rolls over from 1263 back to 0 while \tilde{V}_{k5} does not.

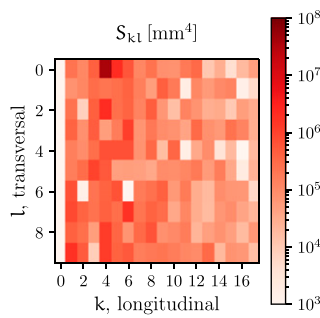


Figure 3. Plot of the power spectral density S_{kl} for the same data that is shown in Figure 2. Notice that only a very small segment of the range $0 \leq k \leq m - 1$ is shown. To smooth out the step-function-like measurement artefacts, all values of S_{kl} were set to zero for $k \geq k^{\text{cut}}$ in subsequent steps. For the length $a=40$ mm shown here, the cutoff occurs at $k^{\text{cut}} = 9$.

2.2. Misalignment data processing

In the following, the necessary preprocessing steps for the application of the measurement data in periodic unit cell analysis are elaborated. These steps were applied repeatedly to obtain as many undulation fields as were required for the analysis presented further down in §3.

Roving width is variable with a mean of 3.60 mm calculated from the entire measurement data. All models considered in the following were chosen to comprise 10 rovings within a fixed model width of $b = 36.0$ mm. In the first step of the preprocessing procedure, a continuous range of 10 rovings was selected at random from the total of 83 rovings. For this purpose, the first three and last three rovings were omitted, since the textile edges were slightly frayed, and those rovings showed an atypically small undulation. Subsequently, a longitudinal starting position was randomly selected from the range of about 320 000 sampling points per roving, omitting the first 5% and the last 5% of the data set. In order to investigate the size effect, models of different lengths $a = 20/40/60/80$ mm were considered. These lengths correspond to 2/4/

6/8 times the dominant undulation wavelength of about 10 mm caused by the stitching yarns dislocating the rovings. For the optical resolution of $31.6\mu\text{m}$ per pixel, these lengths correspond to ranges of $m = 632/1264/1896/2528$ total pixels in longitudinal direction. Beginning from the random starting point, the next m longitudinal sampling points and the next $n = 10$ rovings edges were used as the basis for further processing. The data subset defines a m by n matrix Y_{kl} storing the transversal position, that is, coordinate y in Figure 1, of each roving edge. Row index $k = 0 \dots m - 1$ indicates the position along the evenly spaced sampling points in longitudinal direction, and column index $l = 0 \dots n - 1$ indicates the edge number, each counting from 0 at their respective starting points. Next, the undulation is isolated from the position data by subtracting the mean lateral position \bar{Y}_l of each roving edge l to obtain a new matrix V_{kl} , see (5). It is emphasized that the index l refers to the edges between two rovings, not for the rovings themselves. In a periodic unit cell $n = 10$, roving edges are sufficient to define 10 rovings with the first edge repeated also as the last edge with a lateral translation by b .

$$V_{kl} = Y_{kl} - \bar{Y}_l \quad \bar{Y}_l = \frac{1}{m} \sum_{k=0}^{m-1} Y_{kl} \quad (5)$$

Although the measurement domain approximately fits an integer amount of stitching periods longitudinally, the unprocessed data is not precisely periodic, that is, $V_{0l} \neq V_{ml}$ and $V_{k0} \neq V_{kn}$, see Figure 2(a) and Figure 2(c). Even though deviations from periodicity are rather small, they are inconsistent with periodic unit cell analysis, tend to attract the region of failure and distort results. To avoid this problem, the method to obtain a precisely periodic undulation field via Fourier analysis presented by Liu et al.²³ is applied here. As the first step in this procedure, discrete Fourier analysis is performed on the matrix V_{kl} rendering complex-valued Fourier coefficients F_{kt} , see (6).

$$F_{kl} = \sum_{p=0}^{m-1} \sum_{q=0}^{n-1} V_{pq} \exp\left(-2\pi i \left(\frac{pk}{m} + \frac{ql}{n}\right)\right) \quad (6)$$

From the Fourier coefficients, the real-valued spectral power density S_{kl} may be calculated, (7), where superscript asterisk to F_{kl} indicates its conjugate complex number. The spectral power density S_{kl} retains the information regarding the magnitude of undulation; however, the phase angle θ_{kl} encoded in the complex-valued Fourier coefficients F_{kl} is stripped off in S_{kl} .

$$S_{kl} = \frac{ab}{(2\pi)^2} F_{kl} F_{kl}^* \quad (7)$$

A plot of the power spectral density S_{kl} is displayed in Figure 3. Notice that only a small segment of the range of index k is displayed. The matrix components of S_{kl} determine the intensity of the harmonic oscillation associated with k and l . The longitudinal wavelength of these harmonic oscillations is given by $\lambda_k = a/k$, and the transversal wavelength is given by $\mu_l = b/l$. The dominant harmonic in the measurement data is caused by the stitching yarn piercing through the ply back and forth and thereby displacing the rovings, see Figure 1. For $a=40$ mm, the stitching results in dominant peak at $k = 4$, $l = 0$ which is associated with a longitudinal wavelength $\lambda_4 = 10$ mm and $\mu_0 \rightarrow \infty$. The dominant wavelength of 10 mm corresponds to the nominal sewing period. In transversal direction, the roving displacement is mostly constant, that is, the peak is located at $l = 0$ where the associated wavelength μ_0 tends to infinity and the frequency to zero. Another property apparent from Figure 3 is that the intensity rapidly diminishes with increasing k .

In the next step, edge displacement fields of equivalent spectral power distribution as in the initial data subset V_{kl} , but with enforced periodicity on the boundary, were generated. For this purpose, the spectral power data is complemented by new phase angle data randomly generating θ_{kl} from a uniform distribution ranging from 0 to 2π . These phase angles are, however, not independent over the entire range $0 \leq k \leq m - 1$, $0 \leq l \leq n - 1$, but need to adhere to certain symmetry and antimetry conditions,²³ see (8).

$$\begin{aligned} \theta_{0,0} &= \theta_{m/2,0} = \theta_{0,n/2} = \theta_{m/2,n/2} = 0 \\ \theta_{m-k,0} &= -\theta_{k,0} \quad \text{for } k = 1, \dots, m/2 - 1 \\ \theta_{0,n-l} &= -\theta_{0,l} \quad \text{for } l = 1, \dots, n/2 - 1 \\ \theta_{m/2,n-l} &= -\theta_{m/2,l} \quad \text{for } l = n/2 + 1, \dots, n - 1 \\ \theta_{m-k,n-l} &= -\theta_{k,l} \quad \text{for } k = m/2 + 1, \dots, m - 1 \\ &\quad \text{and } l = 1, \dots, n - 1 \end{aligned} \quad (8)$$

By applying this procedure, a new undulation pattern \tilde{V}_{kl} is obtained from a given spectral power density S_{kl} as the

real-valued part, Re , of the inverse discrete Fourier transform (9). The undulation \tilde{V}_{kl} now satisfies periodicity constraints of the unit cell, unlike the initial data V_{kl} , see Figure 2(b) and (c). Since the spectral power density distribution over the wavelengths associated with k and l is the same between both, the essential characteristics are conserved in this process.

$$\begin{aligned} \tilde{F}_{kl} &= \sqrt{\frac{(2\pi)^2}{ab}} S_{kl} \exp(i\theta_{kl}) \\ \tilde{V}_{kl} &= \frac{1}{nm} \text{Re} \left(\sum_{p=0}^{m-1} \sum_{q=0}^{n-1} \tilde{F}_{pq} \exp\left(2\pi i \left(\frac{pk}{m} + \frac{ql}{n}\right)\right) \right) \end{aligned} \quad (9)$$

The measurement data V_{kl} quantifies the roving edge position in terms of pixels from the coordinate origin; hence, it is inherently discontinuous, cf. Figures 1(c) and 2(c). Occasional ‘split roving’ imperfections introduce further discontinuities to the data set. Together, these discontinuities result in low intensity, low wavelength contributions to S_{kl} and superimpose unrealistic short wavelength, and low amplitude undulations in \tilde{V}_{kl} if not action is taken. To eliminate these artefacts and to obtain a smooth output, all longitudinal harmonics with a wavelength below $\lambda^{\text{cut}} = 5$ mm were considered noise and were removed by setting $S_{kl} = 0$ for $k \geq k^{\text{cut}} = a/\lambda^{\text{cut}}$. This procedure has some effect on the misalignment magnitude; however, it is consistently the same for all misalignment topologies considered here.

2.3. Roving model

For the reasons elaborated in §1.2, the present investigation adopts a homogenized modelling approach at mesoscale. Individual fibers in the rovings are much smaller in diameter than the meso-length scale, so the rovings may be regarded as a transversally isotropic homogeneous solid with one preferential direction from a mesoscopic point of view. The rotation of this preferential direction may then be used to represent the initial misalignment and the subsequent fiber rotation associated with MB. Hence, a viable modelling approach could be based on a solid discretization in combination with a transversally isotropic constitutive law. One disadvantage of this approach is the difficulty of formulating an appropriate anisotropic and nonlinear constitutive law to emulate the roving response. In particular, it is difficult to account for the effect of longitudinal stress on the shear nonlinearity to which MB is very sensitive. Another disadvantage is of practical nature: In the popular Finite Element software Abaqus, which is used in this investigation, this approach suffers from a known limitation³² resulting from the particular implementation of the kinematics of anisotropic solids. In this software, the preferential axis of an anisotropic solid is rotated only by the amount due

Table 1. Material parameters.

Constituents			
Glass fibers	[G;1134;0°//G;36;90°]		
Stitching yarn	[PES;12;L]		
Matrix	Epoxy RIM 135/H137		
Fiber vol. content	50%		
Effective elastic properties			
Longitudinal	\bar{E}_{11}	44.77	GPa
Transversal	\bar{E}_{22}	11.10	GPa
Shear	$\bar{G}_{12}, \bar{G}_{13}$	4.37	GPa
Poisson's ratio	$\bar{\nu}_{12}$	0.27	
Shear properties			
Fracture strength		40	MPa
Energy release rate		1.5	N mm ⁻¹
Ramberg–Osgood parameters used in (10)			
parameter 1	γ_y	6.31×10^{-3}	
parameter 2	τ_y	27.6	MPa
parameter 3	N	7.99	

to the rigid body motion, disregarding any further rotation due to shear deformations. This leads to an overestimation of MB-strength. To overcome both of these problems, Lemansky and Sutcliffe^{24,29} proposed the use of a combination of isotropic solid elements and embedded truss or ‘rebar’ elements instead of a pure solid element discretization with anisotropy. In this approach, the stiffness of the solid elements is enhanced in the preferential direction by the embedded 1-dimensional elements so to obtain the desired longitudinal stiffness via the appropriate rule of mixture. Initial misalignment and subsequent rotation of the preferential direction is then directly associated with the nodal positions that the 1-dimensional elements attach to.

The present investigation adopts Lemansky and Sutcliffe’s approach, and nodal positions are adjusted to so that their length-wise connection traces the undulating preferential direction of the roving. The length-wise connection of these points by truss elements add extensional stiffness to the longitudinal direction, but does not add any bending stiffness and does not introduce any rotational degree of freedom. Truss elements are elastic, and their stiffness was adjusted so that the elastic longitudinal stiffness \bar{E}_{11} measured in a physical calibration test is matched, see Table 1. The linear and nonlinear response in transversal direction and under shear is determined by the solid elements alone. MB-strength is insensitive to the transversal direct stiffness, but sensitive to the shear nonlinearity. To match the nonlinear shear response of the roving, the solid elements feature an isotropic J_2 -plasticity model. This is motivated by the circumstance that yielding occurs in the matrix which may regarded as isotropic. Shear stress is the dominant component in the plasticity model. However, the truss stiffness is finite and this allows for a small contribution of

longitudinal stress via the J_2 yield criterion used in the solid elements. The yielding shear band is never unloaded before attaining the peak load; hence, no benefit can be obtained from a more sophisticated representation of shear nonlinearity via a combined plasticity damage model. To determine the elastic shear stiffness, the plastic hardening law and the shear fracture strength, six tensile tests on $\pm 45^\circ$ -layup specimens were performed according to standard DIN EN 6031. To account for softening subsequent to the initiation of shear fracture, the plastic hardening law was complemented by a subsequent plastic softening regime with an assumed energy release rate G_{II} regularized by element size, see Table 1 and Figure 4(b). The parameters listed in Table 1 state the shear hardening law in terms of parameters of the Ramberg–Osgood relation (10). This relation is used in analytical solutions discussed further down where a deformation theory of plasticity is assumed. The application of deformation theory is admissible, since material points in the shear band are never unloaded before collapse. In formula (10), γ_{12} , σ_{12} and \bar{G}_{12} are the shear strain, shear stress and effective shear modulus, respectively. Symbols τ_y and n are material constants.

$$\gamma_{12} = \frac{\sigma_{12}}{\bar{G}_{12}} \left(1 + \frac{3}{7} \left(\frac{\sigma_{12}}{\tau_y} \right)^{n-1} \right) \quad (10)$$

To verify the suitability of the present modelling approach to capture the peak load, a comparison is made to analytical results due to Budiansky and Fleck¹. The classical formula (11) relates the MB-strength R to the shear stress σ_{12} as a nonlinear function of the shear strain γ_{12} and the initial misalignment angle φ_0 . There, max denotes that the argument is to be maximized with respect to γ_{12} . This result was obtained under the assumption of longitudinally rigid fibers shielding the matrix from any longitudinal strain and stress and yielding is due to shear alone.

$$\frac{R}{G_{12}} = \max_{\gamma_{12}} \left(\frac{\sigma_{12}(\gamma_{12})}{\varphi_0 + \gamma_{12}} \right) \quad (11)$$

The assumption of rigid fibers is a simplification, and in reality, there is a small contribution from longitudinal stress to matrix shear yielding. The effect of this simplification may be gauged by using another analytical result that accounts for the effect of longitudinal stress on the shear nonlinearity, see equation (12). This relation is far more involved, and a full exposition is available in the original source, Equation 96 in Ref. 1. The discussion here is limited to a presentation of the results. Symbol r is to be understood as an independent variable and the ratio $s \equiv \sigma_{11}/\bar{G}_{12}$ acts as the dependent variable. Other symbols are as follows: the longitudinal modulus of the homogenized roving \bar{E}_{11} , the modulus of the isotropic matrix $E_m = 3350$ MPa, the fiber

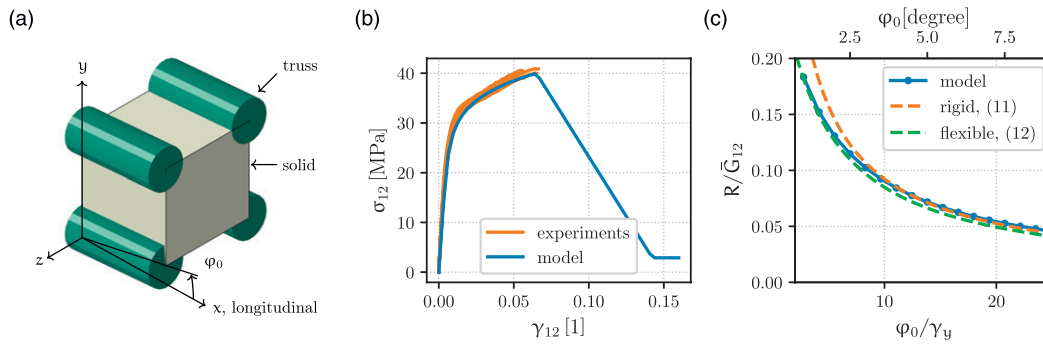


Figure 4. The verification model. The layout of the truss and solid elements in the model is shown in (a). The response of the model under shear loading is determined by the solid element and is compared to six experimental curves in (b). The compressive response of the model for a nonzero initial misalignment φ_0 is compared to analytical models (11) and (12) in (c).

$$r^2 = \frac{s^2 \left(\frac{\varphi_0}{\gamma_y} \right)^2}{\left(1 - s(b r^{n-1} + 1) \right)^2} + \frac{s^2}{3\gamma_y^2 \left(\frac{\bar{E}_{11}}{E_m} + \left(\frac{\bar{E}_{11}}{E_m} - 1 + \nu_f \right) \left(\frac{b}{\rho} r^{n-1} \right) \right)^2} \quad (12)$$

volume content $\nu_f = 1/2$, and further constants: $b = 7/10$, $\rho = 3/2$ and $\gamma_y = \tau_y / \bar{G}_{12}$. The normalized MB-strength $\max(s) = R / \bar{G}_{12}$ is obtained via numerical maximization of (12) with respect to r

Analytical results obtained for rigid fibers (11) and flexible fibers (12) are compared to numerical results obtained from a simple verification model, Figure 4. It is apparent that for a wide range of initial misalignments, all three models give very similar results. The finite stiffness of the truss elements ensures that the numerical results are closer to results from (12) for small initial misalignments $\varphi_0 < 3^\circ$.

Failure due to MB generally preempts failure due to exceeding the compressive fiber crushing strength. However, in some cases of exceptionally low misalignment, the strength limit imposed by MB may exceed the one imposed by fiber crushing strength, see the discussion in Ref. 33. Such situations are disregarded here and only failure due to MB is considered. Moreover, out-of-plane wrinkling of thicker laminates can also not be represented by the model due to the applied boundary conditions.

2.4. Meso scale unit cell modelling

The predominant undulation wavelength in the fiber textile considered here is 10 mm, and its ply thickness is 0.8 mm. These characteristic dimensions define the mesoscale between the microscale associated with the fiber diameter and the macro scale relating to the component size. At meso-scale, it is feasible to resolve individual 0° -rovings and their

geometry. No attempt is made to explicitly model the stitching yarn, and it is reflected only indirectly via its effect on the 0° -roving undulation. The irregularly arranged very low fiber weight 90° -rovings are not expected to substantially impact the microbuckling strength and are also omitted. As elaborated in §2.3, a combination of solid and truss elements, Abaqus designation C3D8 and T3D2, are employed to model the roving stiffness. In longitudinal direction, the mesh size is 10 elements per dominant wavelength of 10 mm. Transversally and through the thickness, each roving is discretized into 4 and 2 elements, respectively. To gauge the effect of the discretization size, models with half and double the elements in each direction were solved resulting in a strength increase of 16% and a strength decrease of 4.4%, respectively. For this investigation, about 1200 models were solved, and to keep the numerical effort manageable, the original mesh size was used. A view of the undeformed mesh for one particular model is shown in Figure 5.

As stated in §1.4, the intention of the present contribution is to investigate the statistical size effect pertaining to a change in volume in isolation from other competing size effects arising from a change of unsupported edge length. To eliminate the latter effect, material unit cells embedded in surrounding material are considered. The volume is varied by changing the model length a in steps of 20/40/60/80 mm. These steps are integer multiples of the wavelength of the dominant harmonic, see Figure 3 and the discussion in §2.2. Periodicity of displacement is enforced via standard periodic boundary conditions. The undulation

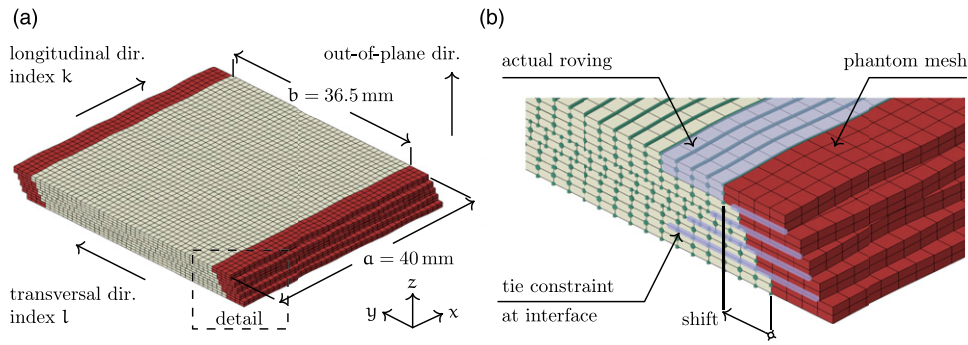


Figure 5. A view of the undeformed mesh of a five ply model of length $a=40$ mm. Subfigure (a) depicts a global view of the model and (b) shows a magnified detail. Rovings are oriented longitudinally and are four elements wide transversally. One roving and four interfaces are shaded blue in (b). The phantom rovings at the edge of the actual unit cell are coloured in red. To avoid clutter truss elements are not shown in (a).

field is applied to the unit cell geometry by adjusting the transversal nodal positions to $\tilde{Y}_{kl} = \tilde{V}_{kl} + \bar{Y}_l$, in order to trace out the edge dislocation as specified by the particular undulation field of the ply. In this process, \tilde{Y}_{kl} is re-sampled as required by the discretization size and applied to the nodal coordinates. Dislocations are faintly visible in Figure 5. The misalignment angles Φ_{kl} corresponding to these nodal dislocations are calculated via (13). Symbol Δ is the truss element length, and indices k and l are wrapped around by taking the modulo operation, if required.

$$\Phi_{kl} = \frac{\tilde{V}_{(k+1)(l)} - \tilde{V}_{(k)(l)}}{\Delta} \quad (13)$$

Out-of-plane misalignments are not modelled. Moreover, the out-of-plane motion is suppressed on the back surface of the laminate to avoid global plate buckling. Therefore, single ply models considered further down in §3.1 only account for the in-plane membrane response, similar to the pure 2-dimensional approaches cited in §1. However, the solid discretization allows the combination of multiple plies to volumetric laminate meshes which are considered in §3.2 and §3.3. In these laminate models, the membrane stiffness of neighbouring plies is coupled via the transverse shear stiffness of the solid elements.

For all model sizes, the spectral density S_{kl} is cut off at the same wavelength $\lambda^{\text{cut}} = 5$ mm and k^{cut} was adjusted accordingly. The histograms in Figure 6 display the distribution of misalignment angles for 100 randomly generated topologies for each of the 4 length classes $a = 20/40/60/80$ mm. The mean misalignment angle is near zero in all cases, and the standard deviation in each class is 2.67/2.68/2.65/2.65 degrees.

Since the element edges at the ply interface follow the imperfection data for their respective plies, meshes are non-congruent between neighbouring plies of laminate

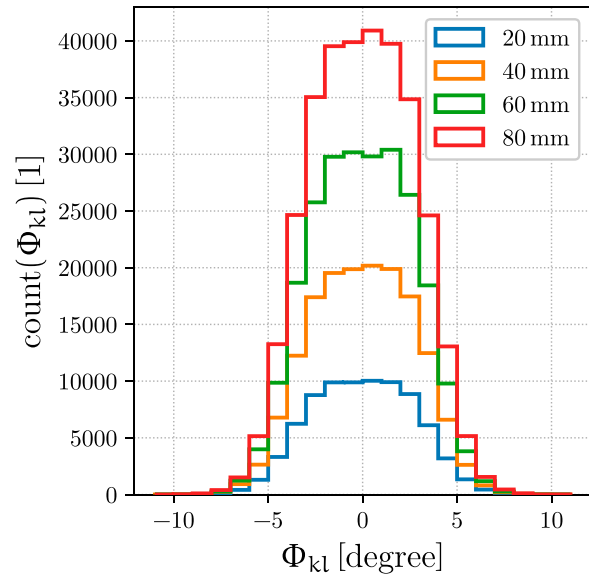


Figure 6. Histogram of the element-wise misalignment angle Φ_{kl} evaluated over 100 misalignment topologies generated for each model size class $a=20/40/60/80$ mm. The total number of elements/angles are 80k/160k/240k/320k in the four classes. The vertical axis counts the number of angles within fixed intervals of 1° .

meshes. Therefore, ‘tie’-constraints were used to enforce bonding of neighbouring plies at their mutual interface, see annotation ‘tie constraint’ in Figure 5(b). This type of constraint couples the displacement of the nodes of a dependent surface to the displacements interpolated from the independent surface.

It is assumed that the manual or automated production of the laminate does not enforce a well-defined lateral position but allows for some lateral shift during the layup of the dry fiber material. This seems reasonable, as the transversal position of consecutive plies in real laminates is usually not aligned perfectly flush and a certain random lateral shift

Table 2. Overview of the simulation series. The slash character separates steps of the varied parameter. Numbers in parentheses are repeated from earlier sections due to reused classes.

Section	Sample size	Plies	Length a [mm]	Width b [mm]	Thickness [mm]
Simulations					
§3.1	100	1	20/(40)/60/80	36	0.8
§3.2	100	(1)/2/3/4/5	40	36	(0.8)/1.6/2.4/3.4/4.0
§3.3	100	5	20/(40)/60/80	36	4.0
Physical validation tests					
§3.4	22	5	20	20	4.0

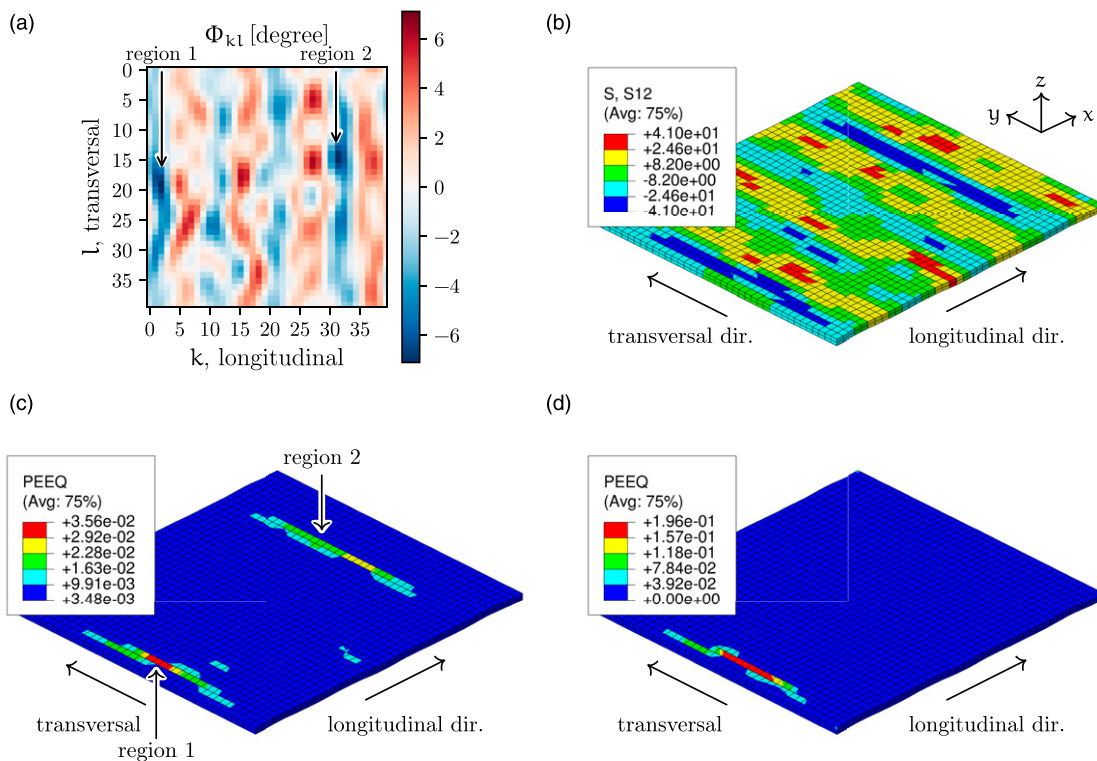


Figure 7. Progression of compressive failure in a typical single ply model of length $a=40$ mm. (a) Shows the initial misalignment field, (b) shows the in-plane shear stress σ_{12} , (c) and (d) both show the equivalent plastic strain; (b) and (c) depict the state at the peak load, that is, the applied far field compression $\bar{\sigma}_{11}$ is largest in magnitude so that $\bar{\sigma}_{11} = R$, (d) depicts the state when the termination criterion is met, that is, $\bar{\sigma}_{11} \leq 0.9R$.

from ply to ply is expected. To account for this manufacturing uncertainty in the model, every ply after the first one was shifted by a certain distance in transversal direction, see annotation ‘shift’ in Figure 5(b). The shift distance of each ply was determined at random from a uniform distribution between 0 and the mean roving width 3.60 mm. Due to this shift, the plan view outline of the ply surfaces forming the interface of any given ply pair are not congruent. This is problematic, as the independent surface of the tie constraint needs to cover the dependent surface completely to allow for displacement coupling via interpolation. As a remedy, the first and the last roving of each ply were repeated outside of

the unit cell as ‘phantom’ roving on either edge of the ply, see annotation ‘phantom roving’ in Figure 5(b). In the figure, phantom rovings are coloured teal and are not part of the unit cell proper coloured in beige. Phantom rovings represent a part of the geometry of the imaginary neighbour unit cells. This allows for an extension of independent tie-surface into the neighbour unit cells, thus, ensuring that it is larger than the dependent surface on the unit cell proper. Nodal displacements in the phantom rovings are entirely coupled to their respective parent rovings. Moreover, the phantom rovings are assigned very compliant material properties, so that their contribution to the unit cell stiffness is negligible.

3. Results and discussion

The previously discussed modelling techniques were applied to 3 separate series of simulations. In each of these series, only one parameter is changed in discrete steps separated by the slash character, see also Table 2. In Sections §3.1 and §3.3, series with model lengths $a = 20/40/60/80$ mm are investigated for a single ply and a 5 ply laminate, respectively. In §3.2, another series representing laminates comprising 2/3/4/5 plies is considered. For each configuration, a class of 100 models were independently generated and solved. All simulations considered an uniaxial loading via a far field compressive stress $\bar{\sigma}_{11}$. At mesoscale, this corresponds to the axial force acting on the unit cell normalized by the unit cell cross-section area. Likewise, the macro scale axial compressive strain $\bar{\epsilon}_{11}$ is defined as the shortening of the unit cell normalized by its length. Both $\bar{\sigma}_{11}$ and $\bar{\epsilon}_{11}$ are defined positive for compression. The primary result of each simulation is the maximum of $\bar{\sigma}_{11}$ which corresponds to

the MB-strength R of the model. In order to positively identify the peak stress, all simulations were continued into the softening regime until the far field stress dropped to 90% of the peak value. This termination criterion was attained in all but one simulation run. The unsuccessful simulation was excluded from all further analyses. Solutions were obtained via dynamic implicit analysis. Dynamic, rather than static, analysis was used to regularize the problem in the post-peak global softening regime. Simulation parameters were chosen so to avoid inertia effects until the load peak is attained. The implicit solution procedure does not require mass scaling for efficient increment sizes in the linear regime before the onset of softening. However, mass/time scaling was still used to enhance convergence in the softening regime.

To validate simulation results, a small series of physical compression tests was conducted and the respective results are reported in §3.4.

3.1. Length size effect study for single plies

In Figure 7, some key states in the failure progression of the first out of 100 single ply models belonging to the size class $a=40$ mm are depicted. It is apparent that up to the peak load, permanent deformation accumulates in two separate regions; however, in the post-peak regime, shear localizes into one critical region. The regions of noteworthy plastic strain correspond to the regions of large initial misalignment magnitude. The peak load is attained when the shear stress reaches the fracture strength of 40 MPa. However, this is particular to the materials considered here, and in general, MB can occur while the shear response is still hardening.

The empirical survival function for each length class in the series $a=20/40/60/80$ mm is shown in Figure 8. These empirical distributions were fitted with a normal distribution and 2/3 parameter Weibull distributions using the maximum-likelihood method. Parameters obtained from the fitting are reported in Table 3. There, and in the following, parameters referring to the 2-parameter form are furnished with an over-script tilde.

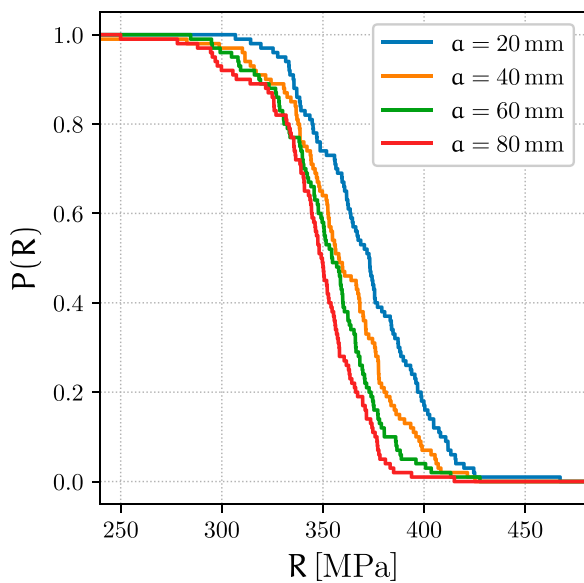


Figure 8. Empirical probability of survival P over the compressive strength R for different length classes.

Table 3. Parameters of different distribution fits. The abbreviation *gof.* stands for goodness-of-fit and indicates the probability that the data follows the respective distribution. Goodness-of-fit was determined via the Pearson- χ^2 -test.

Length a [mm]	Normal distribution fit			2-Parameter Weibull fit			3-Parameter Weibull fit			
	Mean [MPa]	Std. dev [MPa]	<i>gof.</i> [%]	Shape \tilde{m} [1]	Scale \tilde{R}_0 [MPa]	<i>gof.</i> [%]	Shape m [1]	Scale R_0 [MPa]	Thresh R_c [MPa]	<i>gof.</i> [%]
20	372	28.6	81	12.9	385	13	2.9	85	296	57
40	359	29.7	59	13.8	372	55	8.8	238	133	59
60	353	25.8	77	14.3	365	85	4.1	104	259	90
80	347	25.5	16	15.7	358	68	8.7	197	160	50

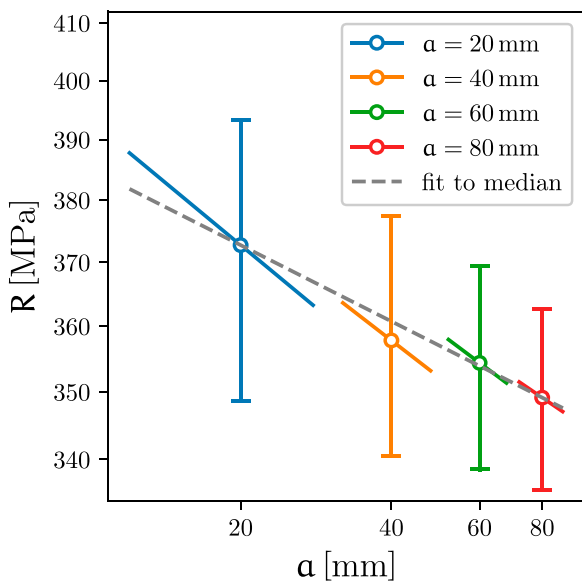


Figure 9. Percentiles of the observed strength R over the model length a . The dots mark the median strength with a probability of survival $P = 0.50$, error bars extend down/up to $P = 0.25/0.75$. The scaling on both axes is logarithmic, although it is barely noticeable on the vertical axis.

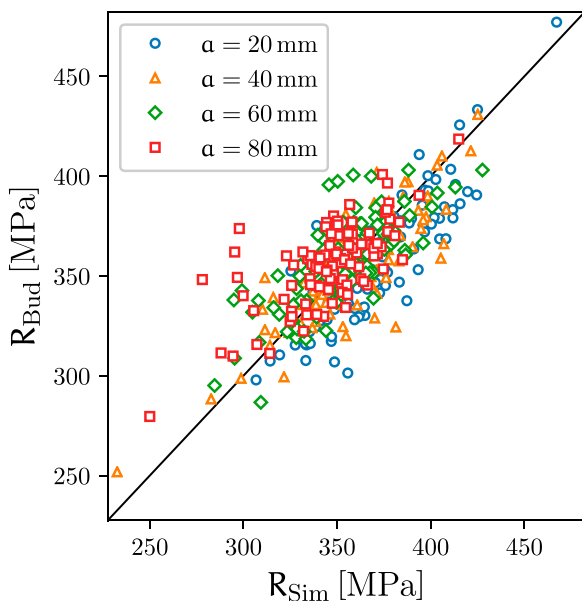


Figure 10. Scatter plot of strength R_{Sim} observed in the simulation versus strength R_{Bud} predicted by Budiansky's formula (11). The effective angle used in this formula is the 90-percentile of the set of all angles of a given model length class.

Each of either the 2- or 3-parameter fits to any of the 4 length classes may be used to calibrate the scaling law (4) rendering eight variants. If the weakest-link model (3) applies, all variants should result in approximately the same relation, regardless of which parameter set from Table 3 is used in the scale law (4). To test this presumption, scaling

laws for the median strength, that is, with a probability of survival $P = 0.5$, are plotted in Figure 9 for each of the 4 length classes as short inclined line segments near the respective model length. These segments show the 2-parameter form of the scale law and appear as a straight line due to the double logarithmic axis scale. The 3-parameter variants are very similar over the considered ranges and are not shown. The scaling law predicted by these curves is to be compared against the reduction of strength obtained for different model lengths. For this purpose, 25/50/75 percentiles of strength are also plotted over the model length a . To aid the comparison, another variant of the scaling law for $P = 0.5$ is included in the plot where $\bar{m} = 21.2$ and $\bar{R}_0 = 372$ MPa were determined so that the fit passes through the median strengths at $a = 20$ mm and 80 mm. Comparing all five variants shows that the slope of the four class-wise fits somewhat overestimate the observed reduction of median strength. Despite these deviations, it appears that the scale law implied by the Weibull fits are approximately consistent with the scaling of the class median strength for the range of sizes considered here. Moreover, it is apparent that in the case of single ply models, the predicted strength is very low. It is shown in the following sections that the bonding of plies to laminates brings about a substantial increase in strength.

Before moving on, the estimation of single ply strength via analytical formulae from measured or assumed misalignment distributions is briefly discussed. In the present approach, the entire set of misalignment angles is known for a given model manifestation from the model generation procedure. Moreover, this set of misalignment angles is associated with a particular microbuckling strength R_{Sim} observed in the simulation of the particular model. This association allows the verification of the predictive capabilities of classical closed-form theories for the buckling strength. In the following, the model (11) will be considered for this purpose. This and other similar formulae were derived via closed-form analysis and, hence, are limited due simplifications with respect to topology and constitutive response. Most critical is that these models take only a single deterministic misalignment angle φ_0 and it is not immediately apparent how they may be applied if the misalignment is quantified as a spatially variable field Φ_{kl} as is the case here. With regard to this problem, Wilhelmsson et al²⁷ proposed a modification to (11) by replacing φ_0 with an 'effective' misalignment angle calculated as a certain percentile of the distribution of angles in the field Φ_{kl} . For this purpose, the absolute value of each angle Φ_{kl} is taken to obtain a half-normal distribution. Subsequently, a certain percentile of the half-normal distribution is considered as the 'effective' misalignment angle. This still leaves the problem of determining which percentile might yield the appropriate 'effective' misalignment. For the present data, it is found empirically that the 90-percentile yields a close to best correlation of the prediction R_{Bud} to the observed strength

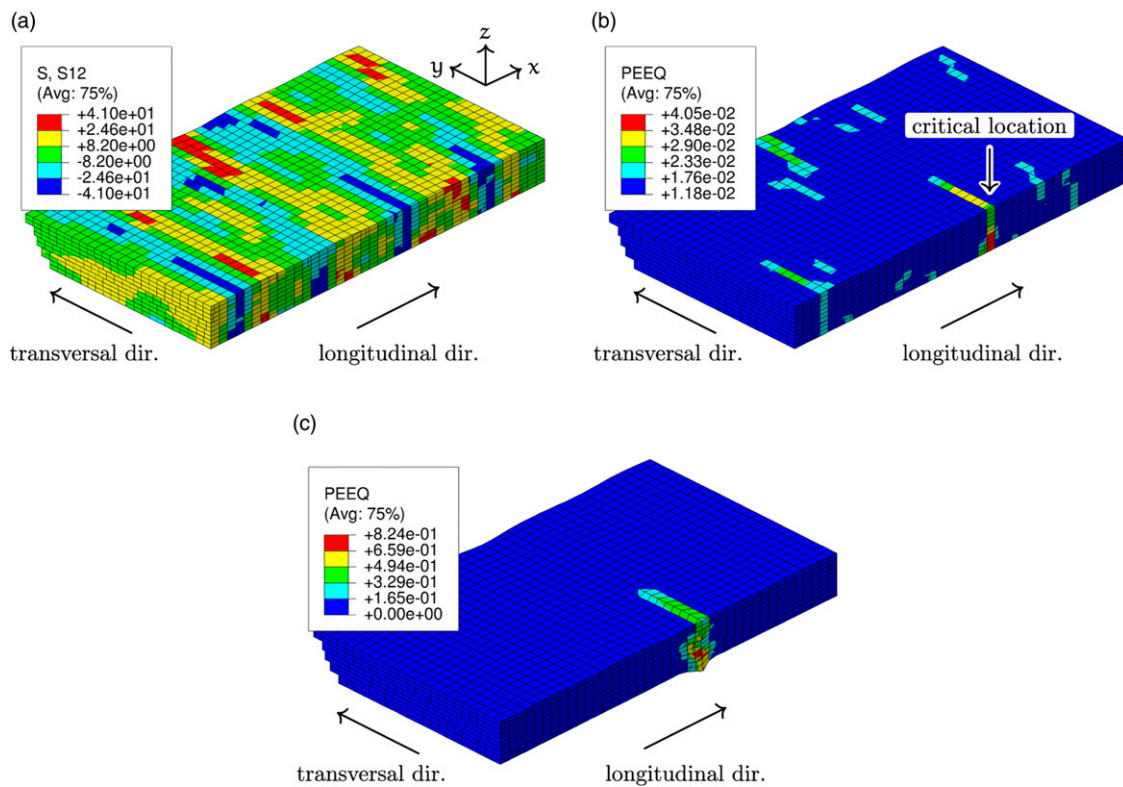


Figure 11. Progression of compressive failure in a typical five ply model of length $a=40$ mm. Model is the same as the one depicted in Figure 5. To inspect the interior only half of the model is shown. (a) and (b) show the in-plane shear stress σ_{12} and the equivalent plastic strain at $\bar{\sigma}_{11} = R$, respectively; (c) depicts the state when the termination criterion $\bar{\sigma}_{11} \leq 0.9R$ is met.

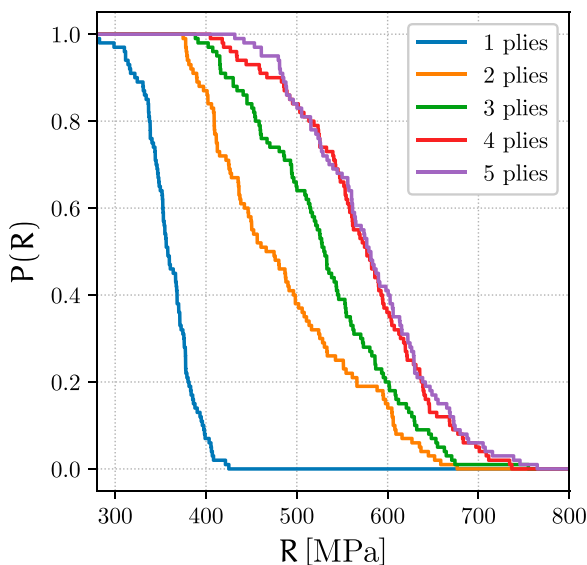


Figure 12. Empirical probability of survival P over the compressive strength R .

R_{Sim} for the series of simulations considered here. A scatter plot of prediction versus observation is provided in Figure 10. The prediction has a mean absolute error of

17.9/12.9/13.9/15.4 MPa for the four considered length steps and the quality of the prediction appears approximately independent from the size of the model.

3.2. The effect of laminating multiple plies

In this section, the effect of bonding 2/3/4/5 plies to a laminate is studied. Contrary to the study in the previous section, only a single unit cell length $a=40$ mm is considered here. Results for the same length already presented in the previous section provide the data point for the single ply case. All plies are nominally aligned in longitudinal direction, that is, $[0^\circ]_{2/3/4/5}$. This stacking sequence is found, for instance, in spar caps of wind turbine blades where transversal stiffness is provided by very thin 90° plies which are not explicitly modelled here. The failure progression in the first of 100 models belonging to the class of models with five plies is depicted in Figure 11.

Again, the results of the series are presented in terms of the empirical survival functions Figure 12 and corresponding parameters in Table 4. Median and percentiles of the strength for the considered ply numbers are plotted in Figure 13. It is apparent that the bonding of plies to a laminate leads to a dramatic increase in strength for the first few plies

Table 4. Parameters of different distribution fits. The abbreviation *gof.* stands for goodness-of-fit and indicates the probability that the data follows the respective distribution. Goodness-of-fit was determined via the Pearson- χ^2 -test. Single ply data is repeated from Table 3.

Plies	Normal distribution fit			2-Parameter Weibull fit			3-Parameter Weibull fit			
	Mean [MPa]	Std. dev [MPa]	<i>gof.</i> [%]	Shape \tilde{m} [1]	Scale \tilde{R}_0 [MPa]	<i>gof.</i> [%]	Shape m [1]	Scale R_0 [MPa]	Thresh R_t [MPa]	<i>gof.</i> [%]
1	359	29.7	59	13.8	372	55	8.8	238	133	59
2	486	81.8	0	6.1	521	0	1.2	121	372	23
3	531	76.0	95	7.4	564	21	2.4	191	362	86
4	574	73.5	88	8.7	607	94	4.0	285	316	89
5	581	72.2	40	8.5	613	75	2.6	198	405	57

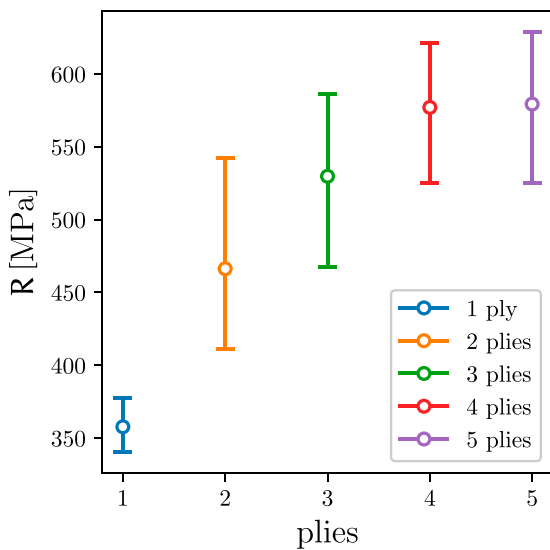


Figure 13. Percentiles of the observed strength R over the number of plies in the laminate. The dots mark the median strength with a probability of survival $P = 0.50$, error bars extend down/up to $P = 0.25/0.75$. Axes are not in logarithmic scale for this diagram.

with a diminishing effect as the ply number increases. This observed strength increase is at odds with the weakest-link Weibull theory discussed in §1.1. The scale law (4) predicts a drop in strength for any increase in volume, either length-wise or in thickness direction. Results from §3.1 confirmed the applicability of the scale law to the length-wise size effect; however, this is clearly not the case here.

An intuitive explanation for the suppression of the statistical size effect is that the critical misalignment, that is, the one that eventually initiates failure, is very likely to be near less severe misalignments in neighbouring plies. This mitigates the misalignment severity and increases strength in multi-ply laminates. For the NCF-textile considered here, the 10 mm harmonic is dominant, see Figure 3. Between neighbouring plies, these dominant harmonic undulations occur with a random phase shift, see (8). When the phase shift is small, the critical misalignment is likely to be in the neighbourhood of a

misalignment in the same direction in the next ply and the strengthening effect is small. If the phase shift happens to be close to half a period, misalignment in the neighbouring ply is likely to be in the opposite direction to the critical misalignment, thus reducing its severity and increasing the laminate strength.

To provide a quantitative evaluation of this reasoning, the simplest case of the 2-ply laminate is considered. The severity mitigation is estimated via the covariance C as defined in (14) for the angle pairs $\Phi_{kl}^{(1)}, \Phi_{kl}^{(2)}$ sharing the same indices k, l in the first and second ply. Positive/negative covariance means that most angle pairs have the same/opposite sign leading to a small/large mitigation, respectively. The misalignment angles are defined at the element-integration point, see (13) and the accompanying text for a definition. Due to the roving displacement and the lateral random shift between 0 and one roving width between plies, $\Phi_{kl}^{(1)}$ and $\Phi_{kl}^{(2)}$ are not necessarily nearest neighbours and may be offset by as much as one mean roving width of 3.60 mm. This simplification is considered adequate for the present purpose. Symbols $\bar{\Phi}^{(1)}$ and $\bar{\Phi}^{(2)}$ denote the mean misalignments in each ply which are approximately zero.

$$C = \sum_k^m \sum_l^n \left(\Phi_{kl}^{(1)} - \bar{\Phi}^{(1)} \right) \left(\Phi_{kl}^{(2)} - \bar{\Phi}^{(2)} \right) \quad (14)$$

By plotting the resulting angle covariance over the observed strength for each 2-ply model in the class, the intuitive expectation that there is an inverse correlation between strength and the degree of covariance of misalignments in neighbouring plies is confirmed, see Figure 14.

The observation that neighbouring plies have a mitigating effect on the misalignment severity also seems to hold in the case of more than 2 plies. To demonstrate this, a strength estimation based on the method of effective misalignment angles, as used in §3.1, is applied to the multi-ply laminate case in two different variants. In the first variant, the effective angle is determined as the 90-percentile of absolute value of the union of all misalignment angles $\Phi_{kl}^{(p)}$ of all p plies in the laminate. As apparent from Figure 15(a), this results in a very poor estimate of the observed strength, except for the single

ply case. The mean absolute errors are 128/173/217/226 MPa for 2/3/4/5 plies, respectively. In the second variant shown in Figure 15(b), a much better estimate is obtained by taking the 90-percentile with respect to a modified set of angles. As a crude approximation of the mitigating effect, this modified set holds the set union of angles averaged between neighbouring plies. Averaged angles $\bar{\Phi}_{kl} = \frac{1}{2}(\Phi_{kl}^{(1)} + \Phi_{kl}^{(2)})$ were calculated pointwise for angle pairs $\Phi_{kl}^{(1)}$ and $\Phi_{kl}^{(2)}$ sharing the indices k, l , and the 90-percentile was taken with respect to these averaged angles. This procedure is only

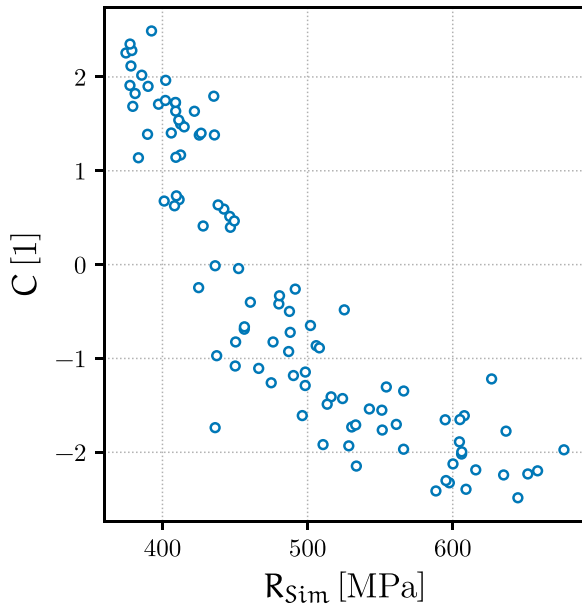


Figure 14. Scatter plot of the empirical covariance C of misalignment over the observed strength R for the 2-ply model series.

approximately correct for the reasons stated further up. Nevertheless, it provides an improved prediction with mean absolute errors of 36/66/99/116 MPa for 2/3/4/5 plies, respectively.

3.3. Length size effect study for laminates

The final series considers again models of increasing length like in §3.1, however, for laminates comprising five plies. Empirical survival distribution Figure 16 and corresponding parameters are reported in Table 5.

To discuss the size effect, a diagram in the manner of Figure 9 is constructed for the multi-ply case, see Figure 17. Like before, the diagram displays the observed 25/50/75 percentiles of the strength and a short segment of the scale law (4) configured class-wise using the parameters in Table 5. In contrast to the results for the single ply case, no lengthwise-size effect is apparent over the range of considered sizes.

3.4. Physical compression tests

Compression tests were performed according to the specifications of ASTM D6641 using a so-called ‘combined loading compression’ fixture. Test specimens are coupon shaped with unsupported edges. In the simulations, unsupported edges are eliminated by the application of periodic boundary conditions. To estimate the impact of the unsupported edges, 100 single ply models were solved with and without periodic boundary conditions which resulted in a lower mean strength of 3.7% in the latter case. Physical specimens were manufactured from the same dry fiber material as the one for which the misalignment was measured, see §2.1. The layup of the specimens is $[0^\circ]_5$ which corresponds to the layup of the models discussed in §3.3. The available fixture limited the gauge area of the specimen to

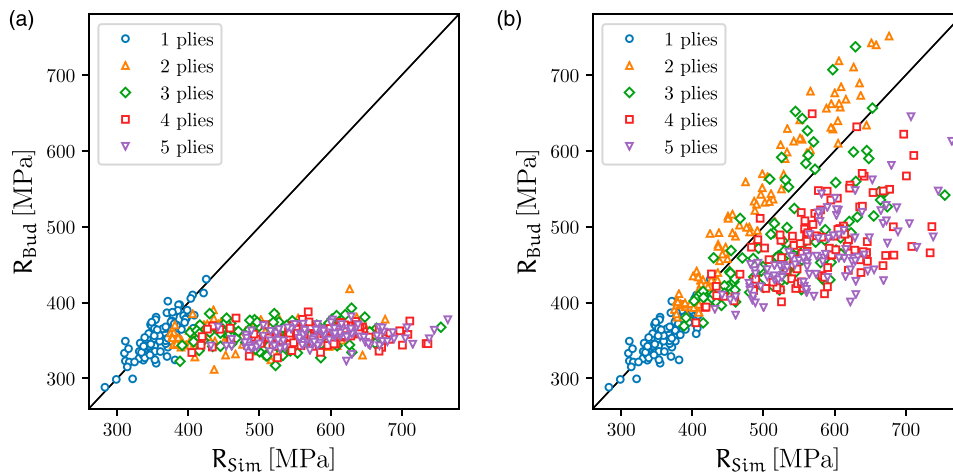


Figure 15. Scatter plot of laminate strength R_{Sim} observed in the simulation versus strength R_{Bud} predicted by Budiansky’s model (12). In (a) the effective angle is assumed as the 90-percentile of all initial misalignment angles. For (b) the same percentile was taken from a new set of angles obtained via averaging angles of neighbouring plies.

20 mm in width. Moreover, the free length between clamps was limited to 20 mm to avoid plate buckling. Thus, the effective stressed volume of the physical specimens is smaller than the volume in the simulations. In order to account for this size difference, the 25/50/75 percentiles of strength are shown in Figure 17 at a horizontal position that corresponds to the stressed volume in the specimen. The testing campaign produced 22 valid results for the compressive strength which is less than the 100 models solved for each configuration class. The empirical survival distribution obtained from the tests is shown in Figure 16. Median strength is somewhat higher, and the spread is more narrow in the physical specimens compared to the simulations. The most likely cause of this deviation is an over estimation of the fiber misalignment due to the measuring artefacts discussed in §2.2.

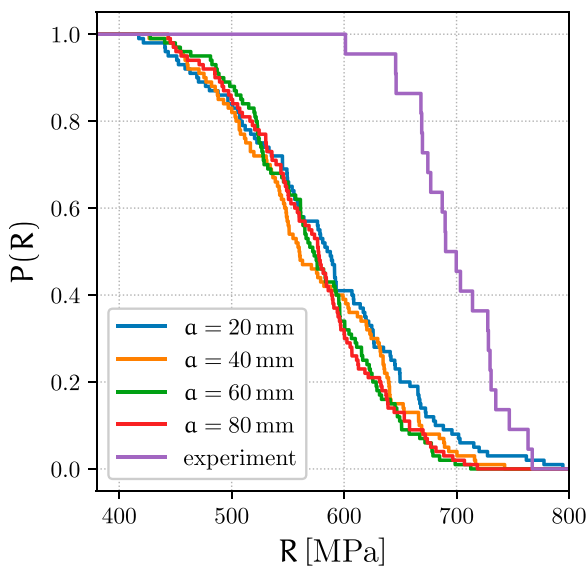


Figure 16. Empirical probability of survival P over the compressive strength R .

3.5. Comparison to results from the literature

It is difficult to compare results from the present contribution to earlier literature, since, the peculiarities of the considered materials and methods prevent direct comparison. Nevertheless, the findings of other authors are reported here to provide some orientation. To the knowledge of the authors, experimental campaigns with the specific intent to characterize size effects were only performed on unidirectional carbon fiber materials. An early experimental investigation by Jelf and Fleck⁹ tested proportionally scaled carbon fiber cross-ply laminate specimens. They assume a 3-parameter Weibull distribution and report $m = 6.1$, $R_0 = 805$ MPa and $R_t = 350$ MPa. Interestingly, the increase of strength with the number of laminate plies for the present NCF-material observed in §3.2 is in contrast to result obtained for unidirectional carbon fiber laminates. Lee and Soutis³⁴ found a strength decrease in proportionally up-scaled unidirectional carbon fiber laminate specimens and no effect of scale for quasi-isotropic layups. However, the authors point out that edge effects due to stress concentrations at the begin of the gauge length may occlude the volume related size effect considered there.

In a numerical investigation, Liu et al.²³ considered an embedded single ply unit cell without unsupported edges which is comparable to the present approach. However, the misalignment properties represented a unidirectional carbon fiber material without a dominant harmonic. The study investigated the effect of different standard deviations and spectral properties of the fiber misalignment for a constant model size. This allowed calibration of the scale law via the fitted Weibull parameters but not verification against the change of strength in models of different size as was considered in §3.1 and §3.3. For a root mean square misalignment amplitude of 0.7° , they find normalized parameters $R_0/\tau_y = 7.25$, $R_t/\tau_y = 28.6$ and $m = 5.60$. Other relevant results were reported by Sutcliffe²⁹ who conducted a numerical investigation of the statistical size effect in single ply models representing carbon fiber reinforced polymers. The misalignment pattern in that investigation was generated from a

Table 5. Parameters of different distribution fits. The abbreviation *gof.* stands for goodness-of-fit and indicates the probability that the data follows the respective distribution. Goodness-of-fit was determined via the Pearson- χ^2 -test. Data for 40 [mm] is repeated from Table 4.

Length a [mm]	Normal distribution fit			2-Parameter Weibull fit			3-Parameter Weibull fit			
	Mean [MPa]	Std. dev [MPa]	<i>gof.</i> [%]	Shape \tilde{m} [1]	Scale \tilde{R}_0 [MPa]	<i>gof.</i> [%]	Shape m [1]	Scale R_0 [MPa]	Thresh R_t [MPa]	<i>gof.</i> [%]
Simulations										
20	584	81.5	13	7.7	620	19	2.8	235	374	88
40	581	72.2	40	8.5	613	75	2.6	198	405	57
60	573	61.5	70	10.3	601	46	3.6	219	376	83
80	573	63.5	95	9.8	601	64	3.1	201	393	98
Experiments										
20	698	40.2	75	19.8	717	66	5.4	204	511	66

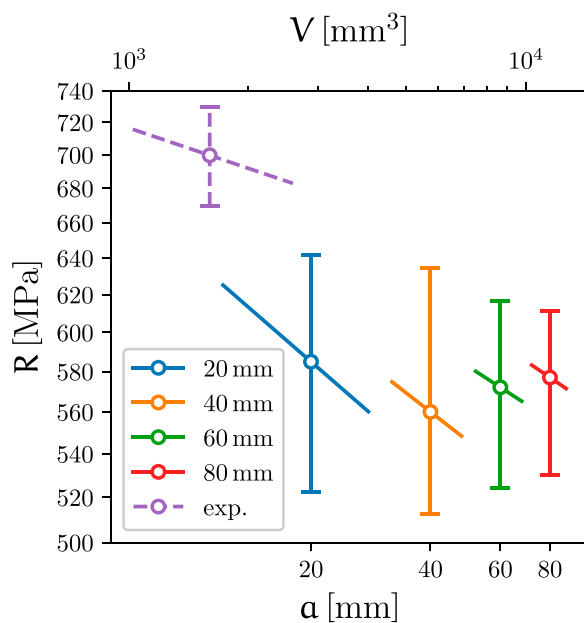


Figure 17. Percentiles of the observed strength R over the effective volume V . The volume V specified by the horizontal axis scale shown on the top of the frame applies to both physical specimens and simulation models. The second horizontal axis shown on the bottom specifies the unit cell length a and applies only to the simulation models. As before, dots mark the median strength with a probability of survival $P = 0.50$, error bars extend down/up to $P = 0.25/0.75$.

misalignment angle distribution with a standard deviation of 1.5° and a controlled autocorrelation property. Unlike the present contribution, the author considered a model with zero traction boundary conditions on the lateral edges. The author assumed a 2-parameter Weibull distribution and reports $\tilde{m} = 16.3$ and 12.9 . The first result was obtained from models with fiber misalignment limited to the model interior, while the latter result was reported for models with misalignments extending to the unsupported edges.

4. Conclusions

Overall, weakest-link Weibull theory provided a good model for the single ply case considered in §3.1. This is apparent from the approximate agreement of strength scaling laws (4) configured via any of the parameters in Table 3 to the observed reduction of strength. However, calibration of the scale law via the distribution parameters obtained for each size class somewhat overestimates the strength drop as evident from Figure 9. The apparent applicability of the weakest-link Weibull model to the single ply case is in contrast with the increase of strength with the number of plies observed in §3.2. From the perspective of a Weibull model, a reduction in strength is expected for any increase in volume, either in longitudinal or thickness direction. However, for the NCF-material considered here, any weakening due to volume increase is completely overpowered by the

misalignment mitigation mechanism discussed in §3.2. It is also apparent that the mitigation is quickly saturated and strengthening abates when the laminate comprises four to five plies, see Figure 13. The effect of more than five layers was not investigated here, and it is possible that for a much larger number of layers, the volume related Weibull weakest-link mechanism eventually becomes dominant. Since physical specimens for compression tests tend to have about five layers or more, it seems unlikely that the mitigation effect becomes apparent in such tests. The mitigating effect is still relevant for numerical investigations; however, it shows that, for example, 2-dimensional approaches representing the misalignment topology of a single ply will underestimate the strength. The same reasoning applies to the strength results obtained for single ply models in §3.1 that were considerably below typical compressive strengths for NCF-materials.

As a secondary result, the use of ‘effective’ misalignment angles derived from a specific percentile of the heterogeneous misalignment field was considered in §3.1 and §3.2. The use of a so defined effective misalignment angle in classical closed-form formulae like Budiansky’s appears applicable in the single ply case. The crux of this approach is, however, that the misalignment angle distribution and the appropriate percentile to define the effective misalignment are usually not known. In the multi-ply case, the approach renders poor results, unless the mitigation effect is considered, see Figure 15.

The length-wise size effect study considered in §3.3 did not reveal a clear size effect over the range of the considered sizes. Results discussed in that section are approximately comparable to results obtained from physical specimens. The comparison of the respective median strengths shown in Figure 17 indicate that the strength is somewhat underestimated in the simulations. On the contrary, the spread of strength results is wider in the simulations than in the physical tests. Since the compressive strength is very sensitive to the misalignment magnitude which is also difficult to measure, it appears that the most likely cause of this deviation is an imperfect quantification of the fiber misalignment angles. As elaborated in §2.1, the misalignment data was acquired by optically tracking the edge between subsequent rovings. The magnitude of undulation of this edge is artificially magnified by sporadic ‘roving split’ flaws which cannot be corrected easily. Hence, the misalignment magnitude may be somewhat larger in the models than in the test specimens. However, the misalignment magnitude is consistent between different models as is evident from Figure 6.

A possible direction for future improvement is the development of more robust image processing and measurement techniques for a more precise misalignment characterization at low cost per scanned area. The latter point is relevant, since a large data base is required to attain statistical significance which is difficult to obtain via high cost/high fidelity methods like computer tomography. Another aspect is that the periodic unit cell approach necessarily restricts the formation of the

shear band to directions parallel to the vector of periodicity. For the orthogonal unit cell used here and in the literature, the shear band is confined to the transversal direction. However, experimentally, the postmortem band is found at some angle to the transversal direction. The effect of this restriction could be evaluated via a non-orthogonal unit cell. A more comprehensive testing campaign dedicated to the quantification of size effects specific to NCF-materials is another starting point for future investigations.

Acknowledgements

Funding by the *Deutsche Forschungsgemeinschaft* (DFG, German research Foundation) - *Projektnummer* 329147126 is gratefully acknowledged. The authors thank Dr Andrea Miene/Faserinstitut Bremen for her support regarding measurements and image processing. Moreover, the authors thank Dr Clemens Hübler for advice regarding the statistical data analysis and Muzzamil Tariq for supporting experiments.

Declaration of conflicting interests

The author(s) declared no potential conflicts of interest with respect to the research, authorship, and/or publication of this article.

Funding

The author(s) disclosed receipt of the following financial support for the research, authorship, and/or publication of this article: This study is supported by *Deutsche Forschungsgemeinschaft* (DFG, German Research Foundation) (329147126)

ORCID iDs

Benedikt Daum  <https://orcid.org/0000-0002-5320-9698>

Jan-Hendrik Ohlendorf  <https://orcid.org/0000-0002-0552-3404>

Notes

1. Provided by SAERTEX GmbH and Co. KG

References

1. Budiansky B and Fleck NA. Compressive failure of fibre composites. *J Mech Phys Sol* 1993; 41(1): 183–211.
2. Davidson P and Waas AM. Mechanics of kinking in fiber-reinforced composites under compressive loading. *Mathematics Mech Sol* 2016; 21(6): 667–684.
3. Fleck NA. Compressive failure of fiber composites. In: Hutchinson J and Wu T (eds). *Advances in applied mechanics*. New York, NY: Academic Press; 1997, pp. 43–117.
4. Waas AM and Schultheisz CR. Compressive failure of composites, part ii: Experimental studies. *Prog Aerospace Sci* 1996; 32(1): 43–78.
5. Pinho ST, Gutkin R, Pimenta S, et al. On longitudinal compressive failure of carbon-fibre-reinforced polymer: from unidirectional to woven, and from virgin to recycled. *Phil Trans R Soc A: Math Phys Eng Sci* 2012; 370: 1871–1895.
6. Daum B, Feld N, Allix O, et al. A review of computational modelling approaches to compressive failure in laminates. *Composites Sci Tech* 2019; 181: 107663.
7. Soutis C, Curtis P and Fleck N. Compressive failure of notched carbon fibre composites. *Proc R Soc Lond A: Math Phys Eng Sci* 1993; 440: 241–256.
8. Lee J and Soutis C. Measuring the notched compressive strength of composite laminates: Specimen size effect of composites: analytical, numerical and experimental techniques, with regular papers. *Composites Sci Tech* 2008; 68(12): 2359–2366, Deformation and Fracture.
9. Jelf PM and Fleck NA. Compression failure mechanisms in unidirectional composites. *J Compos Mater* 1992; 26(18): 2706–2726.
10. Wisnom M, Atkinson J and Jones M. Reduction in compressive strain to failure with increasing specimen size in pinned buckling tests. *Composites Sci Tech* 1997; 57(9): 1303–1308.
11. Johnson DP, Morton J, Kellas S, et al. Scaling effects in sublaminar-level scaled composite laminates. *AIAA Journal* 1998; 36(3): 441–447.
12. Wisnom MR. Size effects in the testing of fibre-composite materials. *Composites Sci Tech* 1999; 59(13): 1937–1957.
13. Bažant ZP. Size effect on structural strength: a review. *Archive Appl Mech* 1999; 69(9): 703–725.
14. Bažant Z, Kim J-J, Daniel I, et al. Size effect on compression strength of fiber composites failing by kink band propagation. *Int J Fracture* 1999; 95(1): 103–141.
15. Zok FW. On weakest link theory and weibull statistics. *J Am Ceram Soc* 2017; 100(4): 1265–1268.
16. Danzer R, Supancic P, Pascual J, et al. Fracture statistics of ceramics - Weibull statistics and deviations from Weibull statistics. *Eng Fracture Mech* 2007; 74(18): 2919–2932.
17. Basu B, Tiwari D, Kundu D, et al. Is weibull distribution the most appropriate statistical strength distribution for brittle materials?. *Ceramics Int* 2009; 35(1): 237–246.
18. Kyriakides S, Arseculeratne R, Perry E, et al. On the compressive failure of fiber reinforced composites. *Int J Sol Structures* 1995; 32(6): 689–738, Time Dependent Problems in Mechanics.
19. Pimenta S, Gutkin R, Pinho S, et al. A micromechanical model for kink-band formation: Part i - experimental study and numerical modelling. *Composites Sci Tech* 2009; 69(7): 948–955.
20. Bishara M, Rolfes R and Allix O. Revealing complex aspects of compressive failure of polymer composites - part i: Fiber kinking at microscale Honor of Prof. Leissa. *Compos Structures* 2017a; 169(Suppl C): 105–115.
21. Bishara M, Vogler M and Rolfes R. Revealing complex aspects of compressive failure of polymer composites - part ii: Failure interactions in multidirectional laminates and validation Honor of Prof. Leissa. *Compos Structures* 2017b; 169(Suppl C): 116–128.

22. Fleck N and Shu J. Microbuckle initiation in fibre composites: A finite element study. *J Mech Phys Sol* 1995; 43(12): 1887–1918.
23. Liu D, Fleck N and Sutcliffe M. Compressive strength of fibre composites with random fibre waviness. *J Mech Phys Sol* 2004; 52(7): 1481–1505.
24. Lemanski SL and Sutcliffe MPF. Compressive failure of finite size unidirectional composite laminates with a region of fibre waviness. *Composites A: Appl Sci Manufacturing* 2012; 43(3): 435–444.
25. Kratmann K, Sutcliffe M, Lilleheden L, et al. A novel image analysis procedure for measuring fibre misalignment in unidirectional fibre composites. *Composites Sci Tech* 2009; 69(2): 228–238.
26. Sutcliffe MPF, Lemanski SL and Scott AE. Measurement of fibre waviness in industrial composite components. *Composites Sci Tech* 2012; 72(16): 2016–2023.
27. Wilhelmsson D, Gutkin R, Edgren F, et al. An experimental study of fibre waviness and its effects on compressive properties of unidirectional ncf composites. *Composites Part A: Appl Sci Manufacturing* 2018; 107: 665–674.
28. Wilhelmsson D and Asp LE. A high resolution method for characterisation of fibre misalignment angles in composites. *Composites Sci Tech* 2018; 165: 214–221.
29. Sutcliffe MPF. Modelling the effect of size on compressive strength of fibre composites with random waviness. *Composites Sci Tech* 2013; 88(Suppl C): 142–150.
30. Clarke AR, Archenhold G, Davidson NC, et al. Determining the power spectral density of the waviness of unidirectional glass fibres in polymer composites. *Appl Compos Mater* 1995; 2(4): 233–243.
31. Ohlendorf J-H, Rolbiecki M, Schmohl T, et al. *Mapretec - Ein Verfahren zur preform-Herstellung durch ebene Ablage für ein räumliches Bauteil als Basis einer automatisierten Prozesskette zur Rotorblattfertigung. resreport, Universität Bremen. Institut für integrierte Produktentwicklung (BIK); SAERTEX GmbH & Co. KG, 2015.*
32. Wisnom MR. Nonlinear analysis of misaligned unidirectional carbon fibre-epoxy compression specimens. *Composites Eng* 1993; 3(6): 547–556.
33. Gutkin R, Pinho ST, Robinson P, et al. Micro-mechanical modelling of shear-driven fibre compressive failure and of fibre kinking for failure envelope generation in cfrp laminates. *Composites Sci Tech* 2010; 70(8): 1214–1222.
34. Lee J and Soutis C. A study on the compressive strength of thick carbon fibre-epoxy laminates. *Composites Sci Tech* 2007; 67(10): 2015–2026.

Chapter IV.

A micropolar approach to microbuckling problems in unidirectionally reinforced polymer composites

In this chapter, micropolar solid theory is applied to regularize the simulation of MB via homogenized approaches in the post buckling regime. The relation of this contribution to the wider context of computational approaches to MB has been briefly discussed further up in Subsec. 1.4.2.

This chapter was published as an article and the respective reference is stated below. The first author developed the scientific concept of the approach, performed the theoretical work, provided the computer implementation, performed all simulations and wrote the manuscript.

B. Daum and R. Rolfes.

A micropolar approach to microbuckling problems in unidirectionally reinforced polymer composites. Mechanics of Materials, page 104112, 2021.

<https://doi.org/10.1016/j.mechmat.2021.104112>



Research paper

A micropolar approach to microbuckling problems in unidirectionally reinforced polymer composites

B. Daum*, R. Rolfes

Institute of Structural Analysis, Leibniz Universität Hannover, Appelstr. 9A, 30167 Hannover, Germany

ARTICLE INFO

Keywords:

A Polymer–matrix composites (PMCs)
 B Non-linear behavior
 B Strength
 C Buckling
 C Computational mechanics

ABSTRACT

The present contribution considers the application of micropolar continuum theory to predict the microbuckling strength of microbuckling problems in long fiber reinforced composites and to extend simulations into the collapse regime. The approach considers a homogenized description at a coarse length scale where fiber and matrix phases are not individually resolved, but are represented indirectly via an effectively equivalent homogenized solid. The salient characteristic of this approach is its superior numerical efficiency over a fine-scale micromechanical representation where fibers and matrix would need to be discretized separately. A disadvantage of conventionally homogenized models, however, is the circumstance that fiber curvature is not accounted for. Hence, the local fiber bending stiffness cannot be preserved in the homogenization process and the strain localization stage of microbuckling problems is rendered ill-posed. Micropolar homogenization rectifies this deficiency by introducing additional rotational degrees of freedom to account for curvature strain. The present contribution distinguishes itself from earlier micropolar homogenization approaches by adapting a Total-Lagrangian finite strain plasticity theory for micropolar continua to the microbuckling problem under consideration here. From this theoretical basis, a constitutive model and a finite element formulation are derived, and the extra parameters introduced by the micropolar solid are identified.

1. Introduction and phenomenology

Microbuckling, abbreviated MB in the following, refers to a particular mode of failure observed in long fiber reinforced unidirectional plies and other fiber architectures under predominantly compressive loading. Sometimes the term fiber-kinking is used synonymously to MB. A brief overview of the phenomenology associated with MB is given further down. For a more detailed overview regarding different aspects of MB several survey articles are available. A general exposition regarding the theory and closed form analysis of MB is due to Budiansky and Fleck (Budiansky and Fleck, 1994; Fleck, 1997; Budiansky et al., 1998). Experimental techniques were surveyed by Schultheisz and Waas (Schultheisz and Waas, 1996; Waas and Schultheisz, 1996). A review of computational models pertaining to MB of unidirectional plies and other fiber architectures is available in Ref. (Pinho et al., 2012a). Recently, computational approaches were also reviewed in Ref. (Daum et al., 2019). The listed literature provides a comprehensive survey to the topic, hence, the discussion of MB phenomenology and theory is limited to aspects that pertain directly to the subject of the present contribution.

Although other modes of failure may compete with MB, it is generally the strength limiting mode in panels under predominantly uniform

compressive stress. Unavoidable preexisting local fiber misalignment causes local shear stress fluctuations, even under nominally pure compression loading. Local shear stress acting on the matrix increases with the applied compression and eventually triggers a nonlinear material response. Under shear, polymer–matrix-composites typically have some degree of ductility, however, the resulting increase in compliance causes further rotation of the initially misaligned fibers and leads to geometrical softening. The far field compressive stress peaks when geometric softening outpaces plastic hardening in the matrix. The particular location where local softening is initiated first is determined by the local misalignment (Liu et al., 2004), free edge effects (Kyriakides et al., 1995; Sutcliffe, 2013) and other aspects. In homogeneously loaded panels, load redistribution is insignificant and cannot compensate for the local softening. Once initiated, MB causes structural collapse of the affected panel via a band of shear strain localization dynamically propagating from the initial location. The band is typically oriented at some obtuse angle to the fiber direction and is of small, but finite, width with respect to the structural scale. From a structural vantage point, the response of the panel is essentially linear until MB initiation. From there on, a sharp snap-back type response is typical, provided the panel is sufficiently large. The sensitive dependence of

* Corresponding author.

E-mail address: b.daum@isd.uni-hannover.de (B. Daum).<https://doi.org/10.1016/j.mechmat.2021.104112>

Received 25 August 2021; Received in revised form 6 October 2021; Accepted 14 October 2021

Available online 20 November 2021

0167-6636/© 2021 Elsevier Ltd. All rights reserved.

apparent strength on local misalignments poses a difficult challenge for compressive strength prediction and contributes to the large scatter of experimental data.

In the presence of an inhomogeneous stress distribution, e.g. due to a notch, compressive fiber crushing may compete with MB as the strength limiting failure mode (Gutkin et al., 2010b,a). Such a situation, however, will not be given any further consideration here and homogeneous loading is assumed throughout. On that condition, the apparent compressive strength is unrelated to fiber strength, as it has no direct effect on shear localization and fiber fracture occurs in later stages of the softening phase. Fiber bending resistance does not have an appreciable effect on the apparent composite strength either, provided that the wavelength of misalignment undulations is at least on the order of 200 (Lemanski and Sutcliffe, 2012) to 400 (Fleck and Shu, 1995) fiber diameters. Measurements and spectral analysis (Clarke et al., 1995; Liu et al., 2004; Sutcliffe et al., 2012) of fiber misalignment found that the minimum undulation wavelength for the base materials and manufacturing techniques considered there generally exceeded these limits. Fiber bending resistance does not have substantial impact on the peak load, i.e. the apparent strength, and bending resistance remains intact over a certain period of progressing shear localization. This gives rise to a phenomenon known as band broadening, where the band of shear localization subsequently widens as the compression increases. Eventually, fiber fracture degrades bending resistance, and fixes the band in place, typically at a width of 10–15 fiber diameters (Fleck et al., 1995). There is some controversy in the literature if fiber fracture is initiated by compressive (Pinho et al., 2012b; Pimenta et al., 2009a) or tensile stress (Fleck et al., 1995; Budiansky et al., 1998; Guimard et al., 2007) due to simultaneous compression and bending in the fiber. Also the in-situ compressive strength of the individual fiber remains unclear and may be substantially different from the tensile strength of fibers (Vinçon et al., 1998) which is more amenable to testing.

2. Scope and motivation

2.1. Micromechanical and homogenized modeling

The present contribution considers models representing a single ply of unidirectionally fiber reinforced polymer at a length scale on the order of a few tens or hundreds of fiber diameters in size. Models at this scale are well suited for the investigation of the phenomenology and progression of MB-failure of individual plies (Fleck and Shu, 1995; Kyriakides et al., 1995; Bishara et al., 2017). Moreover, models at this length scale may be coupled to a multiscale process to obtain a computational model for compressive failure at component scale (Nezamabadi et al., 2015). Depending on the representation of the composite, such models may be classified into two groups: homogenized and micromechanical models. In homogenized approaches, the mechanical properties of the microscopically heterogeneous composite are condensed into a homogeneous medium with an apparently equivalent response at a larger length scale. The effect of the individual phases of the composite and their microstructure is represented indirectly via suitably assumed constitutive models for the linear and nonlinear response. For instance, the anisotropy due to fiber orientation may be accounted for by the introduction of extra constitutive parameters into the strain energy and plasticity potentials (Eidel and Gruttmann, 2003; Vogler et al., 2013).

Complementary, micromechanical approaches aim for a direct representation of the individual phases and apparent properties of the composite, like anisotropy, arise from the constituents and their topology. Micromechanical models are closer to first principles and require less abstraction, however, the explicit modeling of the microstructure incurs a large computational cost limiting the model size to small length scales. Hence, when numerical efficiency and/or larger model size is required, homogenized modeling may be desirable even at relatively small length scales. In particular, efficiency and model size considerations make homogenized micro-scale models attractive for Monte Carlo analysis of stochastic fiber misalignment distributions (Safdar et al., 2018).

2.2. Limitations of homogenized modeling based on Cauchy continuum theory

As elaborated in Section 1, fiber bending resistance has, in most situations, no substantial effect on the apparent compressive strength of unidirectional plies. Thus, there is usually no need to account for strain gradient effects or inherent bending stiffness for the purpose of predicting apparent strength. In the subsequent shear localization phase, however, softening occurs which renders conventional homogenization based on first gradient Cauchy continuum theory ill-posed. This phenomenon is not particular to MB and has been extensively studied in a broader context of shear localization problems. The deficiency with respect to shear localization problems is the circumstance that shear strain tending toward infinity is predicted in a localization zone of a size approaching zero. In a computational model the discretization acts as an artificial lower bound for the extent of the localization zone. Moreover, the ill-posedness generally goes along with numerical difficulties, which are exacerbated in MB-problems by the strong nonlinearity of the snap-back response.

In nature, the singularity of infinite strain over a zone of size zero does not occur since shear band formation goes along with fiber bending. Smaller shear bands induce more bending resistance which enforces a finite bandwidth. Hence, fiber bending, although insignificant for the apparent MB-strength of the composite, plays an important role in the softening regime. This insight may be applied to the regularization of a numerical model by introducing an inherent length property relating to the fiber diameter to quantify bending resistance. A very straightforward regularization technique implementing this principle was proposed in Lemanski and Sutcliffe (2012) where beam elements were embedded into a Cauchy-solid discretization. These beams did not represent individual fibers, but rather their homogenized effect. Although remarkably simple, this technique seems feasible only for structured meshes of constant discretization size. Another drawback is that available beam and solid elements may not have matching interpolation order.

2.3. Generalized continuum theories

A more general approach to overcome the aforementioned limitations may be based on extended continuum theories. A discussion of the hierarchical relation of various extended continuum theories with regard to elasto-plastic modeling is available in Ref. (Forest and Sievert, 2003).

One possible extension of classical Cauchy theory is the introduction of higher than first gradients of the displacement in the constitutive potential functions. This class of extended theories is known in the literature as strain gradient theories if the second displacement gradient is included, or more general as higher grade theories. The second gradient of the displacement with respect to the fiber direction can be associated with fiber bending which provides the required length property absent in conventional Cauchy continuum theory. Fully nonlinear strain gradient continuum theory specialized for the transversal isotropic symmetry class may, in principle, feature a large number of invariants and corresponding material parameters (Spencer and Soldatos, 2007). However, practical models introduce only a handful of extra parameters (Steigmann, 2012; Kim, 2019)

Alternatively, continuum theory may be extended by incorporating extra degrees of freedom, in addition to the standard displacements. This latter class is known as higher order theories and is exemplified by micropolar theory, or synonymously: Cosserat theory; In a micropolar continuum, each point is endowed with rotational degrees of freedom, in addition to the usual displacements. Thus, in micropolar theory each continuum point may perform a rigid body rotation independent from the macroscopic rigid body rotation. In the context of a micropolar theory for a fiber reinforced material, this pointwise rotation may be associated with the local rotation of the fiber cross-section. This provides a handle to introduce a fiber bending strain energy term associated with the gradient of this rotation in a similar, but not completely equivalent manner as is the case for strain gradient theories.

2.4. Prior investigations and motivation

Beam-theory based approaches to MB-problems inherently reflect fiber bending stiffness and are quite common in the literature, see e.g. Refs. (Pimenta et al., 2009b; Feld et al., 2011; Davidson and Waas, 2016). It seems that ‘couple stress’ theory was first used by Fleck et al. in Ref. (Fleck et al., 1995) in an essentially 1-dimensional approach. This investigation is notable since it brought about the notion of band broadening.

For the sake of brevity, further discussion here is limited to approaches based on generalized continuum theory, omitting 1-dimensional approaches. On that condition, it appears that the first application of a ‘general Cosserat theory’-based, 2-dimensional formulation to MB-problems is due to Fleck and Shu (Fleck and Shu, 1995), extending earlier work. The resulting model was implemented in a finite element procedure which was then utilized to investigate the evolution of fiber rotation in a 2-dimensional domain. After these early investigations, it appears that the application of generalized continuum theories to MB have not been considered until more recent investigations by Hasanyan and Waas in Refs. (Hasanyan and Waas, 2018a,b). There, the authors handle geometric nonlinearity in an Updated-Lagrangian setting via a user defined element implemented in the finite element software Abaqus. Material nonlinearity is handled via a modification of Hill’s anisotropic plasticity model and a particular parameter identification procedure for the elastic and plastic material properties is presented.

The present contribution approaches the problem from a different theoretical angle by considering a finite strain plasticity constitutive model in a Total-Lagrangian formulation. The foremost motivation for this approach is that there exists a well established theory of plasticity for higher order solids within this setting (Forest et al., 1997; Forest and Sievert, 2003). Thus, the specialized model for MB presented in this contribution is embedded within a wider context and links up to existing theory. Another aspect is that the Total-Lagrangian vantage point is very popular in solid mechanics and, hence, seems advantageous from a didactic point of view. Besides these practical advantages, it is not claimed that a Total-Lagrangian setting offers a fundamental advantage, and the popular finite element program Abaqus in which earlier approaches were embedded uses a different setting. The model used in the present contribution was implemented from scratch, and the choice of a finite strain setting is not predetermined by some external program. As an additional advantage, this allows the present contribution to provide a transparent exposition of all relevant steps in the model formulation, spanning from equilibrium to numerical implementation. In effect, this contributes to a more complete understanding of the problem within the context of the theory of higher order solids. Moreover, a parameter identification procedure complementary to the one used in Ref. (Hasanyan and Waas, 2018a) is presented. An advantage of the procedure presented here is that it does not depend on the size of the representative volume element adopted as a micromechanical reference model.

3. Model development

3.1. Concept and outline of the present approach

To begin, the modeling concept shall be motivated by referring to some general properties of MB-problems. In line with earlier micropolar approaches to MB mentioned in Section 2.4, the present contribution considers 2-dimensional problems. While fibers are intact, they effectively suppress inelastic deformation along their axis in a homogenized description of the composite. Thus, plasticity is restricted to in-plane shear and possibly transversal normal deformations. However, only in-plane shear inelasticity is essential for MB-problems since, compressive strain transversal to the fiber direction occurs only at large rotations in the deep post-peak load regime, except for any applied far field

Table 1
Index notation and reference frames.

case	alphabet	letter range	coordinate frame
lower case	Latin	a, b, \dots	current
upper case	Latin	A, B, \dots	initial
lower case	Latin	r, s, \dots	back-rotated
lower case	Greek	α, β, \dots	intermediate
lower case	Latin	i, j, \dots	unspecified

transversal loads. In-plane shear nonlinearity is a crucial mechanism for the initiation of MB as well as for the evolution of the shear band in the immediate post peak load regime for the reasons discussed in Section 1. Moreover, it is generally the only mode with notable degree of ductility. Thus, the present contribution considers matrix shear-nonlinearity as the sole material nonlinearity resulting in a simple and clear constitutive model. In light of the additional complexity introduced by the micropolar modeling, this clarity is of particular value. It is noted, that the lack of representation given to other sources of inelastic deformation, like transversal cracking/debonding, fiber fracture, etc., restricts the present approach to the immediate post peak load regime.

The remainder of this section is structured as follows: After a brief discussion of the notation in Section 3.2, the geometrically nonlinear theory for elastoplastic micropolar solids with respect to various reference frames is recalled from Section 3.3 to Section 3.5 based on the theory presented in Forest et al. (1997), Sievert et al. (1998). In Sections 3.6 and 3.7, a new constitutive model tailored to MB-problems is derived within this theory. The linearization and discretization for a finite element formulation are presented in Sections 3.8 and 3.9. Subsequent to a specialization to the case of linear elasticity in Section 3.10, a novel parameter identification technique is discussed in Section 4. In Section 5 the calibrated micropolar model is compared against an analytical model, a micromechanical model, and a conventionally homogenized model.

3.2. Notation

In direct tensor notation, underscore and under-tilde decorations indicate tensor order as defined in (1) for the place holder symbol X and unit vectors \underline{e}_i .

$$\underline{X} = X_i \underline{e}_i \tag{1a}$$

$$\underline{\tilde{X}} = X_{ij} \underline{e}_i \otimes \underline{e}_j \tag{1b}$$

$$\underline{\approx X} = X_{ijkl} \underline{e}_i \otimes \underline{e}_j \otimes \underline{e}_k \otimes \underline{e}_l \tag{1c}$$

When index notation is used, the letter and case of the index indicate the configuration the respective coordinate frame refers to, see Table 1. A two dimensional model is contemplated, hence, all indices iterate over the range $\{1, 2\}$. Symbols δ_{ij} and ϵ_{kl} denote the Kronecker delta and Levi-Civita permutation symbols. The 2 dimensional Levi-Civita symbol ϵ_{kl} corresponds to ϵ_{kl3} in 3 dimensions. As usual, indices following a comma denote differentiation w.r.t. the corresponding direction. The symbol δ is also used as a prefix to a variable to denote variation. Square brackets are used for arguments to functions.

3.3. Kinematics

The displacement-kinematics at finite deformations in a micropolar continuum are specified in terms of a deformation gradient \underline{F} mapping a material segment, initially along $d\underline{X}$, to $d\underline{x}$ in the current configuration in the same way as for a standard continuum (2a). In addition to displacements, a micropolar continuum features independent rotational degrees of freedom and each material point is endowed with a local set of orthogonal directors that may undergo a local rigid body rotation.

This *micro rotation* is, in general, different from the macroscopic rotation of the body, i.e. it is different from the rotation of the displacement field obtained via the polar-decomposition of the deformation gradient \tilde{F} . In the context of the plane formulation contemplated here, the micro rotation is defined in terms of a single rotation angle φ , initially zero. This angle defines an orthogonal rotation matrix $\tilde{R}[\varphi]$, the so-called micro rotation. It maps the director \mathbf{A} from the initial configuration to \mathbf{a} in the current configuration (2b). Subsequently, the director will be identified with the normal to the fiber cross-section.

$$dx_a = F_{aA}dX_A \quad (2a)$$

$$a_a = R_{aA}[\varphi]A_A \quad (2b)$$

Since the micro rotation \tilde{R} is independent from the rotation obtained via polar decomposition of the deformation gradient \tilde{F} , the basis for defining strain measures has to be reconsidered. For this purpose the decomposition (3) is introduced, where \tilde{G} denotes the so-called *Cosserat tensor*. Unlike the right stretch tensor encountered in the polar decomposition of \tilde{F} , it is, in general, unsymmetric.

$$F_{aA} = R_{ar}G_{rA} \quad (3)$$

Solving (3) for \tilde{G} renders a definition in terms of \tilde{F} and \tilde{R} , see (4a). Imposing a rigid body rotation by the orthogonal matrix \tilde{Q} subsequent to \tilde{F} and \tilde{R} , leaves the Cosserat tensor unchanged, i.e. the Cosserat tensor is invariant with respect to \tilde{Q} (4b).

$$G_{rA}[\tilde{F}, \tilde{R}] := R_{ar}F_{aA} \quad (4a)$$

$$G_{rA}[\tilde{Q}\tilde{F}, \tilde{Q}\tilde{R}] = Q_{as}R_{sr}Q_{at}F_{tA} = \delta_{st}R_{sr}F_{tA} = G_{rA}[\tilde{F}, \tilde{R}] \quad (4b)$$

A gradient in the micro rotation of neighboring material points gives rise to a strain-like property known as *wryness*. In the context of a plane deformation, the wryness is given by the vector $\underline{\Gamma} := [\Gamma_{31} \ \Gamma_{32}]^T$ denoting the gradient of the rotation angle φ with respect to the spatial directions in the initial frame (5b). The first index always equals 3 and is dropped in the following so that $\Gamma_1 \equiv \Gamma_{31}$ and $\Gamma_2 \equiv \Gamma_{32}$.

$$d\varphi = \Gamma_A dX_A \quad (5a)$$

$$\Gamma_A = \varphi_{,A} \quad (5b)$$

The wryness is related to the micro rotation as shown in (6a), where ϵ_{rs} is the Levi-Civita permutation symbol in 2 dimensions. Like the Cosserat tensor, wryness is invariant under the rigid body rotation \tilde{Q} , see (6b).

$$\Gamma_A[\tilde{R}] := \frac{1}{2}\epsilon_{rs}R_{as}R_{ar,A} \quad (6a)$$

$$\Gamma_A[\tilde{Q}\tilde{R}] = \frac{1}{2}\epsilon_{rs}Q_{at}R_{ts}Q_{au}R_{ur,A} = \frac{1}{2}\epsilon_{rs}\delta_{tu}R_{ts}R_{ur,A} = \Gamma_A[\tilde{R}] \quad (6b)$$

The invariance property of \tilde{G} and $\underline{\Gamma}$ implies objectivity and makes them a suitable basis for the formulation of constitutive equations.

3.4. Kinetics

The wryness strain resulting from a gradient in the rotational degree of freedom is conjugate to a corresponding *couple stress*. The couple stress acts as a moment on each material point in addition to the conventional force stress conjugate to displacement strain. Couple and force stresses are constitutively related to their respective strain measures, and linked to each other by the equilibrium condition. For the case at hand, couple stresses are thought of as the micropolar homogenization of the fiber bending moments. In a micromechanical representation of the composite, the couple stress would be observed directly as the moment arising from the distribution of (force-)stress over the volume element. The homogenized representation of the composite takes a stand point at a coarser length scale where fibers and matrix are not individually resolved. In a conventionally homogenized solid the effect of the uneven stress distribution is lost.

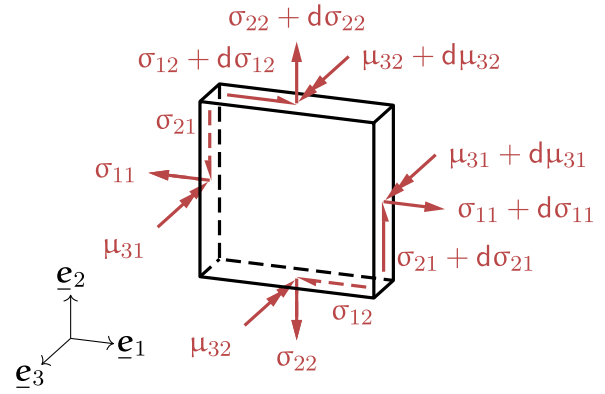


Fig. 1. Force and couple stress components acting on a volume element.

Force- and couple stress components acting on a homogenized material point in the current configuration are shown in Fig. 1. In principle, external loads may introduce additional force or moment densities to the balance considerations, however, such loads are disregarded here. Moreover, only static equilibrium is considered, eliminating any inertia effects. Notice that the convention used here is so that the first index of the stress component indicates the direction of action, while the second indicates the section plane. Assuming plane stress in direction e_3 , the first index of the two nonzero couple stress components is always 3. To simplify the notation, this redundant index is omitted for couples stress components $\mu_{31} \equiv \mu_1$ and $\mu_{32} \equiv \mu_2$.

As for conventional solids, translational equilibrium requires that the divergence of the Cauchy force stress σ vanishes, (7a). The presence of Cauchy couple stress $\mu = [\mu_1 \ \mu_2]^T$ in the rotational equilibrium renders the Cauchy force stress tensor non-symmetric, in general, see (7b).

$$\sigma_{ab,b} = 0 \quad (7a)$$

$$\mu_{a,a} - \epsilon_{ab}\sigma_{ab} = 0 \quad (7b)$$

The virtual power $\delta\mathcal{P}$ is the weak form of (7), where v is the current volume.

$$\delta\mathcal{P} = \int_v (\sigma_{ab,b}\delta u_a + (\mu_{a,a} - \epsilon_{ab}\sigma_{ab})\delta\varphi) dv = 0 \quad (8)$$

Applying Gauss' theorem, (8) is separated into virtual power densities of the internal forces δp_{int}^{cur} and external forces at the boundary δp_{ext}^{cur} . Both measured w.r.t. units of current volume and area, respectively. Symbol n_a denotes components of the normal vector at the boundary surface s with prescribed tractions.

$$\delta\mathcal{P} = + \int_{s_{\sigma,s_\mu}} \delta p_{ext}^{cur} ds - \int_v \delta p_{int}^{cur} dv = 0 \quad (9a)$$

$$\delta p_{ext}^{cur} = \sigma_{ab}n_b\delta u_a + \mu_a n_a\delta\varphi \quad (9b)$$

$$\delta p_{int}^{cur} = \sigma_{ab}(\delta u_{a,b} + \epsilon_{ab}\delta\varphi) + \mu_a\delta\varphi_{,a} \quad (9c)$$

The boundary term (9b) corresponds to the externally applied traction forces and couples, it is not considered any further. Moving on to the power density of the internal forces, (9c), the virtual velocity gradient $\delta u_{a,b}$ and the virtual angular velocity $\delta\varphi$ are restated in terms of rates referring to the Cosserat tensor and wryness. By taking the time derivative and variation of (4a) and (6a), the identities (10) become apparent.

$$\delta u_{a,b} + \epsilon_{ab}\delta\varphi = R_{ar}\delta\dot{G}_{rA}^{-1}G_{As}R_{bs} \quad (10a)$$

$$\delta\varphi_{,a} = \delta\Gamma_A^{-1}G_{Ar}R_{ar} \quad (10b)$$

By using (10) in (9c) the expression (11) for the virtual internal power density w.r.t. to a rotated frame is obtained. There, $s_{rs} = R_{ar}\sigma_{ab}R_{bs}$ and

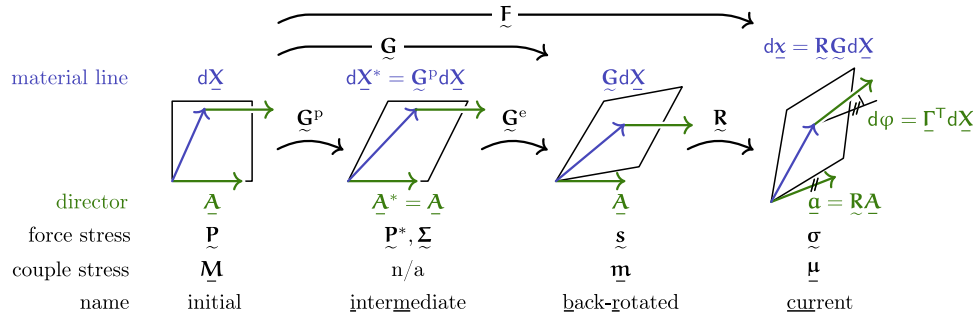


Fig. 2. Schematic of the different kinematic and kinetic quantities.

$m_r = \mu_a R_{ar}$ are understood as a pull-back of force and couple Cauchy stress from the current configuration to a coordinate frame attached to the micro-structure (Forest et al., 1997). The name back-rotated is used here to refer to this frame and a schematic overview of the different stages of deformation is included further down.

$$\delta p_{\text{int}}^{\text{br}} = s_{rs}^{-1} \dot{G}_{As} \delta \dot{G}_{rA} + m_r \dot{G}_{Ar} \delta \dot{\Gamma}_A \quad (11)$$

3.5. Multiplicative split and thermodynamical principles

For the formulation of the elasto-plastic constitutive model it is necessary to separate strain into elastic and plastic contributions. The field of finite strain plasticity of conventional continuum theory produced a large variety of concepts and approaches to this end (Xiao et al., 2006). Approaches based on the notion of an elastically unloaded intermediate configuration between initial and current configuration form a particular class of theories within this field. In the context of conventional solids, the main characteristic of that approach is a multiplicative decomposition of the total deformation gradient into respectively purely plastic and purely elastic sub-steps. The plastic step maps the initial configuration to the intermediate and the elastic step maps the intermediate to the current configuration.

A comprehensive theory for finite strain plasticity of generalized continua was presented in Forest and Sievert (2003), and in particular for micropolar continua in Sievert et al. (1998), Forest et al. (1997). For micropolar solids, the problem of elastic-plastic strain partition applies to both the Cosserat tensor and the wryness, rather than just the deformation gradient as in conventional solids. To this end, the aforementioned authors propose a multiplicative decomposition for the Cosserat tensor in combination with a mixed multiplicative/additive split for the wryness.

For the MB-problem under consideration here, plastic deformation may occur only via fiber-parallel in-plane shear. As argued in Section 3.1, no other plastic deformation shall be considered, in particular no plastic deformation of the fiber. Noting that wryness and couple stress serve as homogenized abstractions of fiber bending strain and stress, it is assumed here that the total wryness is entirely elastic, negating the need for a decomposition. With respect to the remaining Cosserat tensor, the theory based on a multiplicative split as outlined above is adopted. This yields (12), where superscripts e and p denote elastic and plastic sub-steps of deformation, respectively.

$$G_{rA} = G_{ra}^e G_{aA}^p \quad (12a)$$

$$\Gamma_A = \Gamma_a^e \delta_{aA} \quad (12b)$$

Like the overall Cosserat deformation \underline{G} , its elastic part \underline{G}^e is an invariant tensor under rigid body rotation \underline{Q} superimposed to the current configuration. Thus, the time derivatives $\dot{\underline{G}}$ of the invariant quantities \underline{G} and $\underline{\Gamma}$ with regard to their decomposition in (12) are given in (13).

$$\dot{G}_{rA} = \dot{G}_{ra}^e G_{aA}^p + G_{ra}^e \dot{G}_{aA}^p \quad (13a)$$

$$\dot{\Gamma}_A = \dot{\Gamma}_a^e \delta_{aA} \quad (13b)$$

Dropping the variation symbol δ in (11), the actual power is obtained. Inserting the multiplicative split (12) and (13) in this expression yields $p_{\text{int}}^{\text{im}}$, the internal power density per unit volume on the intermediate configuration (14d). There, several abbreviations were introduced: \underline{P}^* the stress conjugate of the rate of the elastic Cosserat tensor (14a), $\underline{\Sigma}$ the Mandel stress $\underline{\Sigma}$ conjugate to the plastic velocity gradient (14b), and \underline{M} conjugate to the rate of wryness. The symbol J^e represents the determinant of elastic Cosserat tensor, and is assumed to be approximately 1.

$$P_{ra}^* := J^e s_{rs}^{-1} G_{as}^e \quad (14a)$$

$$\Sigma_{\alpha\beta} := J^e G_{ra}^e P_{*r\beta} \quad (14b)$$

$$M_A := J^e m_r G_{Ar} \quad (14c)$$

$$p_{\text{int}}^{\text{im}} = P_{ra}^* \dot{G}_{ra}^e + \Sigma_{\alpha\beta}^{-1} G_{A\beta}^p \dot{G}_{aA}^p + M_A \dot{\Gamma}_A \quad (14d)$$

Fig. 2 provides a schematic overview of the numerous kinematic and kinetic quantities involved. The designation intermediate configuration for the elastically unloaded configuration in-between the initial and the back-rotated configuration is somewhat ambiguous, however it is retained here from conventional plasticity theory.

The elastic part of Cosserat tensor \underline{G}^e and the wryness $\underline{\Gamma}$ are assumed to contribute to the Helmholtz strain energy $\psi[\underline{G}^e, \underline{\Gamma}]$.

$$\psi = \frac{\partial \psi}{\partial G_{ra}^e} \dot{G}_{ra}^e + \frac{\partial \psi}{\partial \Gamma_A} \dot{\Gamma}_A \quad (15)$$

Now state laws for \underline{P}^* and \underline{M} may be obtained by considering the intrinsic mechanical dissipation d under isothermal conditions.

$$d = \left(P_{ra}^* - \frac{\partial \psi}{\partial G_{ra}^e} \right) \dot{G}_{ra}^e + \Sigma_{\alpha\beta}^{-1} G_{A\beta}^p \dot{G}_{aA}^p + \left(M_A - \frac{\partial \psi}{\partial \Gamma_A} \right) \dot{\Gamma}_A \quad (16)$$

The standard argument of reversibility of \dot{G}_{ra}^e and $\dot{\Gamma}_A$ requires that the brackets vanish identically, i.e. the state laws are given by (17).

$$P_{ra}^* = J^e \frac{\partial \psi}{\partial G_{ra}^e} \quad (17a)$$

$$M_A = J^e \frac{\partial \psi}{\partial \Gamma_A} \quad (17b)$$

The elastic domain in stress-space is defined by the inequality $\underline{y}[\underline{\Sigma}, \underline{Q}] < 0$, where \underline{y} is the yield function. Evolution equations for the rate of the plastic Cosserat tensor are obtained by maximizing d subject to the inequality constraint $\underline{y}[\underline{\Sigma}, \underline{Q}] \leq 0$. This is implemented by minimizing the Lagrangian functional \mathcal{L} as defined in (18), where λ is a Lagrange-multiplier taking only positive values.

$$\mathcal{L} = -d + \lambda \underline{y} \quad (18)$$

Optimality condition $\partial \mathcal{L} / \partial \Sigma_{\alpha\beta} = 0$ provides the evolution Eqs. (19).

$$G_{A\beta}^p \dot{G}_{aA}^p = \lambda \frac{\partial \underline{y}}{\partial \Sigma_{\alpha\beta}} \quad (19a)$$

This concludes the summary of the finite strain plasticity theory for micropolar solids and sets the stage for formulating a specific material model. For this purpose specific functions of the strain energy ψ and the yield function \underline{y} are adopted in Sections 3.6 and 3.7, respectively.

3.6. Elasticity

The task at hand is to specify a strain energy function ψ that reflects the transversal isotropic symmetry of the long fiber reinforced ply and properly accounts for the extensions required by the micropolar solid. The strain energy should give rise to a transversal isotropic elastic relation and, therefore, depends on the direction unit vector \underline{A}^* on the intermediate configuration. Moreover, in (15) it was already assumed that the strain energy depends on the generally unsymmetric elastic Cosserat tensor \underline{G}^e and the wryness $\underline{\Gamma}$. Both are invariant under rigid body transformation as shown by (4b) and (6b). In the following it is convenient to separate the Cosserat tensor into a symmetric part \underline{S} and an antisymmetric part \underline{T} , see (20).

$$S_{ij} := \frac{1}{2}(G_{ij}^e + G_{ji}^e) - \delta_{ij} \quad (20a)$$

$$T_{ij} := \frac{1}{2}(G_{ij}^e - G_{ji}^e) \quad (20b)$$

To proceed, the customary assumption that force and couple stress are coupled via the equilibrium equations, but not by the constitutive relation is adopted. A constitutive coupling of force stress and couple stress is possible in the case of general anisotropy, but not for the transversal isotropic symmetry class considered here (Kessel, 1964). On this basis, the strain energy may be split into separate contributions from force strain ψ_1 and couple strain ψ_2 , see (21).

$$\psi[\underline{A}^*, \underline{G}^e, \underline{\Gamma}] = \psi_1[\underline{A}^*, \underline{S}, \underline{T}] + \psi_2[\underline{A}^*, \underline{\Gamma}] \quad (21)$$

The two strain energy contributions are isotropic tensor functions of the considered arguments \underline{A}^* , \underline{S} , \underline{T} , and $\underline{\Gamma}$, i.e. they depend on the arguments only via certain functional bases. Tables for the irreducible functional bases of isotropic tensor functions for vectorial and tensorial arguments are available in the literature, e.g. (Liu, 2002). Considering the force strain energy ψ_1 first, the functional bases of the respective arguments are stated in (22) where bases of higher than 2nd order in \underline{G}^e were omitted.

$$I_1[\underline{S}] = S_{ii} \quad (22a)$$

$$I_2[\underline{S}] = S_{ij}S_{ij} \quad (22b)$$

$$I_3[\underline{A}^*, \underline{S}] = A_i^*S_{ij}A_j^* \quad (22c)$$

$$I_4[\underline{A}^*, \underline{S}] = A_i^*S_{ij}S_{jk}A_k^* \quad (22d)$$

$$I_5[\underline{T}] = T_{ij}T_{ij} \quad (22e)$$

$$I_6[\underline{A}^*, \underline{S}, \underline{T}] = A_i^*T_{ij}S_{jk}A_k^* \quad (22f)$$

To obtain a linear elastic constitutive relation, the strain energy is specified as a quadratic form, see (23). There, factors η_1 to η_6 are generic elasticity constants, their identification is discussed further down. The mixed term I_1I_3 is redundant in 2 dimensions and omitted. Linear terms representing effects like thermal expansion are not considered.

$$2\psi_1[\underline{A}^*, \underline{G}^e] = \eta_1 I_1^2 + \eta_2 I_2 + \eta_3 I_3^2 + \eta_4 I_4 + \eta_5 I_5 + \eta_6 I_6 \quad (23)$$

From (23) and (17a) one obtains the force stress (24a). The force stress elasticity tensor $\underline{\mathbb{E}}$ appearing there is related to the elasticity constants as stated in (25) and (24b).

$$P_{ra}^* = \mathbb{E}_{ras\beta}(G_{s\beta}^e - \delta_{s\beta}) \quad (24a)$$

$$\begin{aligned} \mathbb{E}_{ras\beta} &= \frac{\partial P_{ra}^*}{\partial G_{s\beta}^e} = \eta_1 \mathbb{E}_{ras\beta}^1 + \eta_2 \mathbb{E}_{ras\beta}^2 + \eta_3 \mathbb{E}_{ras\beta}^3 \\ &+ \eta_4 \mathbb{E}_{ras\beta}^4 + \eta_5 \mathbb{E}_{ras\beta}^5 + \eta_6 \mathbb{E}_{ras\beta}^6 \end{aligned} \quad (24b)$$

The tensor contributions $\mathbb{E}_{ras\beta}^k$ are the second derivative of the corresponding invariant I_k with respect to \underline{G}^e .

$$\mathbb{E}_{ras\beta}^1 = +\delta_{ra}\delta_{s\beta} \quad (25a)$$

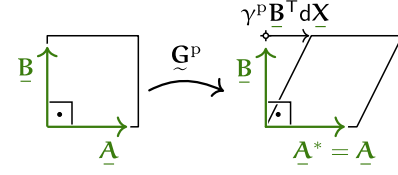


Fig. 3. Kinematics of plastic deformation.

$$\mathbb{E}_{ras\beta}^2 = +\frac{1}{2}(\delta_{r\beta}\delta_{s\alpha} + \delta_{rs}\delta_{\alpha\beta}) \quad (25b)$$

$$\mathbb{E}_{ras\beta}^3 = +A_r^*A_\alpha^*A_s^*A_\beta^* \quad (25c)$$

$$\mathbb{E}_{ras\beta}^4 = +\frac{1}{4}(2\delta_{r\beta}A_s^*A_\alpha^* + 2\delta_{s\alpha}A_r^*A_\beta^* + \epsilon_{r\alpha}\epsilon_{s\beta}) \quad (25d)$$

$$\mathbb{E}_{ras\beta}^5 = -\epsilon_{ra}\epsilon_{s\beta} \quad (25e)$$

$$\mathbb{E}_{ras\beta}^6 = +\delta_{\alpha\beta}A_r^*A_s^* - \delta_{rs}A_\alpha^*A_\beta^* \quad (25f)$$

Because neither P_{ra}^* nor $G_{s\beta}^e$ are symmetric, the force stress elastic tensor $\mathbb{E}_{ras\beta}$ features only major symmetry, i.e. it is symmetric only with regard to a simultaneous transposition of $r \leftrightarrow s$ and $\alpha \leftrightarrow \beta$. Moving on to the couple stress constitutive relation, the respective functional bases are given in (26).

$$J_1[\underline{\Gamma}] = \Gamma_\alpha\Gamma_\alpha \quad (26a)$$

$$J_2[\underline{A}^*, \underline{\Gamma}] = A_\alpha^*\Gamma_\alpha \quad (26b)$$

The generic constants for the couple stress are ζ_1 and ζ_2 and the quadratic form is stated in (27).

$$2\psi_2[\underline{A}^*, \underline{\Gamma}] = \zeta_1 J_1 + \zeta_2 J_2^2 \quad (27)$$

and from (17b)

$$M_A = D_{AB}\Gamma_B \quad (28a)$$

$$D_{AB} = \zeta_1 \delta_{AB} + \zeta_2 A_A^*A_B^* \quad (28b)$$

In Section 3.10 the fourth order force elasticity tensor $\underline{\mathbb{E}}$ is recast to a matrix notation and a parameter identification technique is discussed in Section 4.

3.7. Plasticity

Plastic deformation is restricted to fiber-parallel in-plane shear. Hence, the plastic part of the Cosserat tensor can be expressed in terms of the fiber director \underline{A} , unit vector \underline{B} perpendicular the fiber direction, and a plastic shear factor γ , see Fig. 3 and (29a). The plastic shear from initial to intermediate configuration does not rotate the fiber direction, therefore, the rate of the plastic Cosserat tensor is given by (29b). Moreover, $\underline{A}^* = \underline{A}$ may be used in the elastic relations derived in Section 3.6.

$$G_{\alpha A}^p = \delta_{\alpha A} + \gamma^p A_\alpha B_A \quad (29a)$$

$$\dot{G}_{\alpha A}^p = +\dot{\gamma}^p A_\alpha B_A \quad (29b)$$

Yielding is initiated when the shear stress on the fiber parallel section plane attains a critical value. The respective shear stress component is obtained by projecting the Mandel stress $\underline{\Sigma}$ onto vectors \underline{A} and \underline{B} . The yield strength in this plane is denoted by S and is a function of the isotropic hardening variable q (30). The shear strength refers to apparent properties of the homogenized solid and the hardening variable is strictly increasing with the rate $\dot{q} = |\dot{\gamma}^p|$.

$$y = |\Sigma_{\alpha\beta} A_\alpha B_\beta| - S[q] \quad (30)$$

Evaluating the general evolution law (19) for the specific yield function (30) provides (31), where s is a shorthand for $\text{sgn}[\Sigma_{\alpha\beta} A_\alpha B_\beta]$, and sgn is the Signum function.

$$G_{A\beta}^p \dot{G}_{\alpha A}^p = \lambda \frac{\partial y}{\partial \Sigma_{\alpha\beta}} = s \lambda A_\alpha B_\beta \quad (31)$$

The next step is to develop an integration procedure for the constitutive law in the elasto-plastic regime for the use in an incremental-iterative finite element solution process. The procedure is supposed to take the new Cosserat tensor $\underline{\underline{G}}$, obtained by the previous iteration of the global equilibrium, and should return the stress $\underline{\underline{P}}^*$ and internal variables γ^p, q compatible with the state law and yield condition. In order to formulate a numerical solution scheme, the relevant equations are combined into one, starting by stating the Mandel stress defined in (14b) in terms of the elastic Cosserat tensor by inserting the elastic relation (24).

$$\Sigma_{\epsilon\alpha} = G_{r\epsilon}^e \mathbb{E}_{ras\beta} (G_{s\beta}^e - \delta_{s\beta}) \quad (32)$$

Using the previous equation and $G_{r\epsilon}^e = G_{rA} G_{A\epsilon}^p = G_{rA} (\delta_{A\epsilon} - \gamma^p A_A B_\epsilon)$, the resolved shear stress $\Sigma_{\epsilon\alpha} A_\epsilon B_\alpha$ can be recast in terms of the input $\underline{\underline{G}}$ and a quadratic polynomial in the unknown γ^p . The single scalar unknown γ^p may then be found by inserting this expression in the yield function (30) and applying Newton's scheme. For this purpose the Jacobian $j = \partial y / \partial \gamma^p$ is required, see (33).

$$j = s \left(\Sigma'_{\epsilon\alpha} A_\epsilon B_\alpha - \frac{\partial S}{\partial q} \right) \quad (33a)$$

$$\begin{aligned} \Sigma'_{\epsilon\alpha} &= \frac{\partial}{\partial \gamma^p} \left[G_{rA} G_{A\epsilon}^p \mathbb{E}_{ras\beta} G_{sB}^p G_{B\beta}^p \right] \\ &= -(A_A B_\epsilon G_{B\beta}^p + G_{A\epsilon}^p A_B B_\beta) G_{rA} \mathbb{E}_{ras\beta} G_{sB}^p \end{aligned} \quad (33b)$$

$$G_{B\beta}^p = (\delta_{B\beta} - \gamma^p A_B B_\beta) \quad (33c)$$

3.8. Linearization

To utilize the previously discussed constitutive model for the simulation of MB-problems a numerical solution scheme for the unknown displacements \underline{u} and unknown rotations φ must be adopted. In the context of a solution via an implicit finite element simulation the prior linearization and discretization of the respective equations is required. Here, a Lagrangian formulation is contemplated and the power of the internal forces (11) is recast by grouping the stress terms (34a) and (34b) to provide the power density per unit volume on the initial configuration (34c). To simplify the notation, no superscript is used with p_{int} .

$$P_{rA} := s_{rs} G_{As}^{-1} \quad (34a)$$

$$M_A := m_r G_{Ar}^{-1} \quad (34b)$$

$$p_{\text{int}} = P_{rA} \dot{G}_{rA} + M_A \dot{\Gamma}_A \quad (34c)$$

In (34c), the force stress power is specified in terms of the conjugate pair $\underline{\underline{P}}, \underline{\underline{G}}$ rather than $\underline{\underline{P}}^*, \underline{\underline{G}}^e$ for which the elastic relation (24a) was derived. However, $\underline{\underline{P}}$ may be readily obtained via the pull-back operation (35).

$$P_{rA} = G_{A\alpha}^p P_{r\alpha}^* \quad (35)$$

The nonlinear solution path comprises subsequent equilibrium states. In each equilibrium state the variation (36) w.r.t. \underline{u} and $\dot{\varphi}$ vanishes.

$$\delta p_{\text{int}} = \frac{\partial}{\partial h} [p_{\text{int}} [u_a + h \delta u_a, \dot{\varphi} + h \delta \dot{\varphi}]]_{h=0} \quad (36)$$

Taking into account the definitions (4a) and (5b) provides (37). There, the abbreviations $\delta \dot{F}_{aA} := \delta \dot{u}_{a,A}$ and $R'_{ar} := \partial R_{ar} / \partial \varphi = R_{as} \epsilon_{rs}$ are introduced.

$$\delta \dot{G}_{rA} = R'_{ar} F_{aA} \delta \dot{\varphi} + R_{ar} \delta \dot{F}_{aA} \quad (37a)$$

$$\delta \dot{\Gamma}_A = \delta \dot{\varphi}_{,A} \quad (37b)$$

$$\delta p_{\text{int}} = P_{rA} \delta \dot{G}_{rA} + M_A \delta \dot{\Gamma}_A \quad (37c)$$

Application of the Newton–Raphson scheme to search for solutions to (37c), requires a linearization (38) w.r.t. the unknowns \underline{u} and φ .

$$\Delta [\delta p_{\text{int}}] = \frac{\partial}{\partial h} [\delta p_{\text{int}} [u_a + h \Delta u_a, \varphi + h \Delta \varphi]]_{h=0} \quad (38)$$

The linearized equilibrium is given by (39).

$$\Delta [\delta \dot{G}_{rA}] = (+R'_{ar} \Delta F_{aA} - R_{ar} F_{aA} \Delta \varphi) \delta \varphi + R'_{ar} \Delta \varphi \delta F_{aA} \quad (39a)$$

$$\Delta [\delta \dot{\Gamma}_A] = 0 \quad (39b)$$

$$\Delta [\delta p_{\text{int}}] = \Delta P_{rA} \delta \dot{G}_{rA} + P_{rA} \Delta [\delta \dot{G}_{rA}] + \Delta M_A \delta \dot{\Gamma}_A \quad (39c)$$

Moreover, increments $\Delta[\underline{\underline{G}}]$ and $\Delta[\underline{\underline{\Gamma}}]$ are given in (40).

$$\Delta G_{rA} = R_{ar} \Delta F_{aA} + R'_{ar} F_{aA} \Delta \varphi \quad (40a)$$

$$\Delta \Gamma_A = \Delta \varphi_{,A} \quad (40b)$$

In (39c) the increments of the force stress $\Delta[P_{rA}]$ and the increment of the couple stress $\Delta[M_A]$ appear. The stress increments are related to the strain increments (40) by their respective tangent operators $\underline{\underline{C}}$ and $\underline{\underline{D}}$, (41).

$$\Delta P_{rA} = C_{rAsB} \Delta G_{sB} \quad (41a)$$

$$\Delta M_A = D_{AB} \Delta \Gamma_B \quad (41b)$$

Since the couple stress is entirely elastic, D_{AB} is given by (28b). The force stress increment, however, is to be determined via the algorithmic elasto-plastic tangent. To limit the scope, the algorithmic tangent is not derived in an analytical manner here, rather it is determined by the numerical perturbation technique proposed in Ref. (Miehe, 1996). The method preserves the quadratic convergence of the Newton–Raphson scheme, but incurs some extra computational cost over the analytical approach.

3.9. Discretization

Completion of the nonlinear finite element formulation commenced in Section 3.8 requires the discretization of the domain. Thus, for a given element ℓ , displacements \underline{u}^ℓ and rotations φ^ℓ are interpolated from respective discrete nodal values U_{an}^ℓ and V_n^ℓ via a set of interpolation functions N_n defined with respect to coordinates ξ_i in the reference domain, see (42) and Fig. 4.

$$u_a^\ell = N_n[\underline{\xi}] U_{an}^\ell = \mathcal{A}_{anp} N_n[\underline{\xi}] U_p^\ell \quad (42a)$$

$$\varphi^\ell = N_n[\underline{\xi}] V_n^\ell \quad (42b)$$

Index n indicates the node number and p iterates over the range $[1..2\hat{n}]$ where \hat{n} is the amount of nodes in the element. The factor $\mathcal{A}_{anp} = 1$ if $p = n + \hat{n}(a - 1)$ and zero otherwise is used to vectorize nodal displacements via $U_{an}^\ell = \mathcal{A}_{anp} U_p^\ell$. From (42) the gradients (43) are calculated, where I_{iA}^ℓ is the inverse of the element-Jacobian and i refers to the direction on the reference domain. The abbreviations \mathcal{B}_{aAp}^ℓ and B_{An}^ℓ are defined as apparent from (43).

$$F_{aA}^\ell = \delta_{aA} + \mathcal{A}_{anp} N_{n,i}[\underline{\xi}] I_{iA}^\ell [\underline{\xi}] U_p^\ell = \delta_{aA} + \mathcal{B}_{aAp}^\ell [\underline{\xi}] U_p^\ell \quad (43a)$$

$$\Gamma_A^\ell = I_{iA}^\ell [\underline{\xi}] N_{n,i}[\underline{\xi}] V_n^\ell = B_{An}^\ell [\underline{\xi}] V_n^\ell \quad (43b)$$

Inserting the relevant expression into the linearization of the virtual power density of the internal forces (39c) and subsequent integration over the element domain Ω^ℓ provides the internal force $\underline{F}_{\text{int}}^\ell$ and tangent stiffness $\underline{\underline{K}}^\ell$ contributions (44). The vector of nodal variables has the structure $[U_{11} \dots U_{2\hat{n}} V_1 \dots V_{\hat{n}}]$.

$$\underline{F}_{\text{int}}^\ell = \int_{\Omega^\ell} \begin{bmatrix} \underline{f}^\ell \\ \underline{g}^\ell \end{bmatrix} d\Omega \quad (44a)$$

$$\underline{\underline{K}}^\ell = \int_{\Omega^\ell} \begin{bmatrix} \underline{k}^\ell & \underline{l}^\ell \\ \underline{m}^\ell & \underline{n}^\ell \end{bmatrix} d\Omega \quad (44b)$$

The sub-matrices in (44) are defined in (45).

$$f_p^\ell = P_{rA} \mathcal{B}_{aAq}^\ell R_{ar} \quad (45a)$$

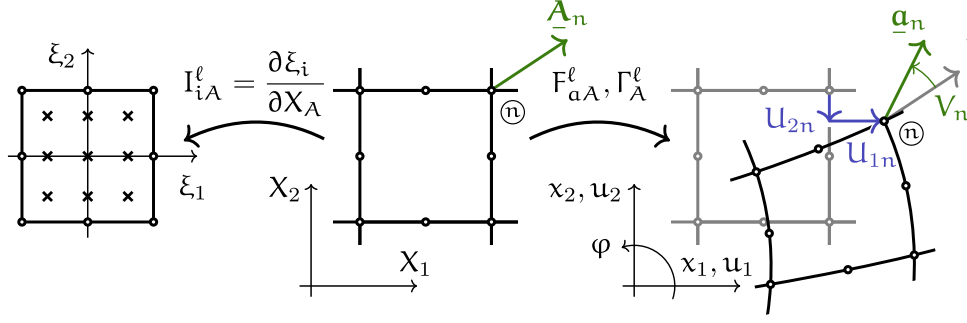


Fig. 4. Nodal displacements $U_{\alpha n}^{\ell}$ and nodal rotations V_n^{ℓ} for a given finite element ℓ . From left to right the images show: the reference space, the initial configuration, and the current configuration.

$$g_n^{\ell} = M_A B_{Am} + P_{rA} F_{aA} N_m R'_{ar} \quad (45b)$$

$$k_{pq}^{\ell} = C_{rAsB} \mathcal{B}_{aBp}^{\ell} \mathcal{B}_{bAq}^{\ell} R_{as} R_{br} \quad (45c)$$

$$l_{pn}^{\ell} = C_{rAsB} F_{bA} N_m \mathcal{B}_{aBp}^{\ell} R_{as} R'_{br} + P_{rA} N_m \mathcal{B}_{aAp}^{\ell} R'_{ar} \quad (45d)$$

$$m_{np}^{\ell} = l_{pn}^{\ell} \quad (45e)$$

$$n_{nm}^{\ell} = B_{Am}^{\ell} D_{AB} B_{Bn}^{\ell} + C_{rAsB} F_{aB} F_{bA} N_m N_n R'_{as} R'_{br} - P_{rA} F_{aA} N_m N_n R_{ar} \quad (45f)$$

The finite element formulation discussed here has been implemented in a Python program. All results presented in Section 5 pertaining to micropolar solids were obtained from this implementation. For MB-problems, a snap-back type response, i.e. a simultaneous decrease of applied load and load-point displacement, is typical for the post-peak load regime. Hence, an arc-length controlled solution of the global equilibrium is required to traverse this segment of the equilibrium path. The particular arc-length control scheme used here is detailed in de Souza Neto and Feng (1999).

3.10. Specialization for small strain elasticity

Before proceeding to the parameter identification procedure in the next section, the set of elasticity constants η_i and ζ_i , introduced in Section 3.6, are interpreted by contemplating the special case of geometric and material linearity. To this effect, a small perturbation by $\underline{\Delta u}$ and $\Delta\varphi$ w.r.t. the initial configuration shall be considered, i.e. $F_{aA} \rightarrow \delta_{aA}$, $R_{ar} \rightarrow \delta_{ar}$ and $R'_{ar} \rightarrow \epsilon_{ra}$. An according specialization of (39) leads to (46), where the superscript 0 indicates that the linearization refers to the initial configuration.

$$\Delta G_{rA}^0 = \Delta F_{rA}^0 + \epsilon_{rA} \Delta\varphi^0 \quad (46a)$$

$$\Delta \Gamma_A^0 = \Delta\varphi_{,A}^0 \quad (46b)$$

All stress measures defined above coincide, and symbols $\Delta\sigma^0$ and $\Delta\mu^0$ introduced further down denote the linearized force and couple stress. Both can be obtained from their respective elastic relation (24a) and (28a). The couple stress elastic relation is already given in a matrix form and it is illuminating to also restate the force stress elastic relation in this manner. For this purpose a vectorization $\underline{\epsilon}$ of the linearized Cosserat tensor and wryness strain is adopted (47). To ease interpretation, the first 3 components in $\underline{\epsilon}$ are formed so that they coincide with Voigt's vector notation of the linearized strain in conventional solids. The remaining components are particular to micropolar solids and shall be examined further in the following.

$$\underline{\epsilon} = \left[\Delta G_{11}^0 \quad \Delta G_{22}^0 \quad (\Delta G_{12}^0 + \Delta G_{21}^0) \quad (\Delta G_{12}^0 - \Delta G_{21}^0) \quad \Delta \Gamma_1^0 \quad \Delta \Gamma_2^0 \right]^T \quad (47)$$

By referring to the relation (46a) the strain vector may also be formulated in terms of linearized displacement strains and linearized rotations. To this end, the symbol $\Delta\phi^0 = \frac{1}{2}(\Delta F_{21}^0 - \Delta F_{12}^0)$ is introduced to denote the linearized macro rotation, i.e. the rotation of the displacement field. When micro and macro rotation differ, a respective strain is registered in the 4th component of $\underline{\epsilon}$. The last

two components $\Delta\Gamma_1^0$ and $\Delta\Gamma_2^0$ represent the curvature strain in their respective direction.

$$\underline{\epsilon} = \left[\Delta F_{11}^0 \quad \Delta F_{22}^0 \quad (\Delta F_{12}^0 + \Delta F_{21}^0) \quad 2(\Delta\phi^0 - \Delta\Phi^0) \quad \Delta \Gamma_1^0 \quad \Delta \Gamma_2^0 \right]^T \quad (48)$$

The force and couple stress components are rearranged into vector form $\underline{\tau}$ in a manner similar to the strain components. Again, the bracket terms are formed to have correspondence to the first 3 components of the stress vector in conventional solids.

$$\underline{\tau} = \left[\Delta\sigma_{11}^0 \quad \Delta\sigma_{22}^0 \quad \frac{1}{2}(\Delta\sigma_{12}^0 + \Delta\sigma_{21}^0) \quad \frac{1}{2}(\Delta\sigma_{12}^0 - \Delta\sigma_{21}^0) \quad \Delta\mu_1^0 \quad \Delta\mu_2^0 \right]^T \quad (49)$$

With respect to these definitions a matrix representation $\underline{\tilde{D}}$ of the elastic constitutive relation is obtained (50). For clarity, it is assumed there that the preferential direction \underline{A} is aligned with the first coordinate direction \underline{e}_1 .

$$\underline{\tau} = \underline{\tilde{D}} \underline{\epsilon}$$

$$\underline{\tilde{D}} = \begin{bmatrix} \eta_1 + \eta_2 + \eta_3 + \eta_4 & \eta_1 & 0 & 0 & 0 & 0 \\ \eta_1 & \eta_1 + \eta_2 & 0 & 0 & 0 & 0 \\ 0 & 0 & \frac{1}{2}\eta_2 + \frac{1}{4}\eta_4 & \frac{1}{8}\eta_6 & 0 & 0 \\ 0 & 0 & \frac{1}{8}\eta_6 & -\frac{1}{2}\eta_5 & 0 & 0 \\ 0 & 0 & 0 & 0 & \zeta_1 + \zeta_2 & 0 \\ 0 & 0 & 0 & 0 & 0 & \zeta_1 \end{bmatrix} \quad (50)$$

4. Parameter identification

The 6 generic constants η_1 to η_6 appearing in the elastic stiffness matrix $\underline{\tilde{D}}$, see (50) may be replaced by a new set of constants $D_{11}, D_{12}, D_{22}, D_{33}, D_{34},$ and D_{44} , see (51). Moreover, bending moments are only transmitted in fiber direction, hence, the constant ζ_1 is set to zero.

$$\underline{\tilde{D}} = \begin{bmatrix} D_{11} & D_{12} & 0 & 0 & 0 & 0 \\ D_{12} & D_{22} & 0 & 0 & 0 & 0 \\ 0 & 0 & D_{33} & D_{34} & 0 & 0 \\ 0 & 0 & D_{34} & D_{44} & 0 & 0 \\ 0 & 0 & 0 & 0 & \zeta_2 & 0 \\ 0 & 0 & 0 & 0 & 0 & 0 \end{bmatrix} \quad (51)$$

The upper left sub matrix in (51) is the same as for a conventional transversal isotropic solid. Assuming plane strain, the respective coefficients are given by (54). There, $E_l, E_t,$ and $\nu_{lt} = -\frac{\zeta_t}{E_l}$ are the standard effective moduli and Poisson's ratios of the homogenized solid, where indices l and t denote the longitudinal and transversal directions.

$$D_{11} = \frac{E_l^2}{E_l - E_t \nu_{lt}^2} = \eta_1 + \eta_2 + \eta_3 + \eta_4 \quad (52)$$

$$D_{12} = \frac{E_l E_t \nu_{lt}}{E_l - E_t \nu_{lt}^2} = \eta_1 \quad (53)$$

$$D_{22} = \frac{E_l E_t}{E_l - E_t \nu_{lt}^2} = \eta_1 + \eta_2 \quad (54)$$

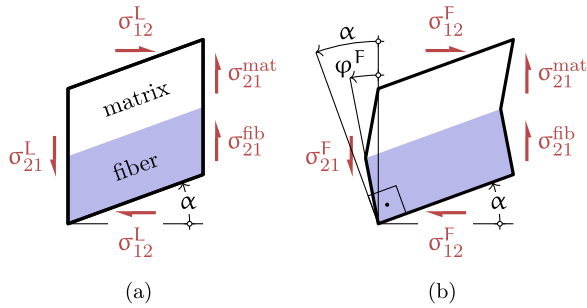


Fig. 5. A micromechanical schematic of the two shear load cases considered to identify the micropolar shear properties. In (a) the rotation of the cross-section is locked to zero, while in (b) it rotates freely as determined by its shear stiffness.

4.1. Elastic shear parameter identification

The remaining coefficients D_{33} , D_{34} , and D_{44} are particular to micropolar solids and require attention. Ref. (Hasanyan and Waas, 2018a) identifies these parameters by considering three complementary shear load cases: $\sigma_{12} \neq 0$ with $\sigma_{21} = 0$, $\sigma_{21} \neq 0$ with $\sigma_{12} = 0$ and $\sigma_{12} = \sigma_{21}$; The respective loads were applied as surface traction on a micromechanical finite element model. No periodicity boundary conditions were enforced in that approach resulting in a somewhat non-uniform deformation which was controlled by studying the effect of the micromodel size. There, the compliance matrix, i.e. the inverse of (51), is found from the resulting deformation of the model under the corresponding applied load.

The present contribution takes a complementary approach by identifying the elastic parameters from the stiffness, rather than the compliance, of a unit cell. This allows the consideration of periodicity constraints to avoid any dependence on the considered unit cell size. For this purpose only two complementary shear load cases need to be considered: one were the rotation of the fiber cross-section is locked to zero, and another with free rotation of the cross-section, see Fig. 5. There, the symbol α is introduced to denote the applied shear angle, and φ denotes the rotation of the fiber cross-section, as before. To simplify the notation, the prefix Δ and the superscript 0 indicating the linearization w.r.t. the initial configuration are dropped.

Considering the locked load case first, a set of equations is obtained by evaluating (50) with $\varphi = 0$. Notice that this constraint requires that the fiber has finite shear flexibility. The unsymmetric shear stress components $\sigma_{12}^L, \sigma_{21}^L$ arising under these conditions are furnished with an superscript L and it is recalled that the first index denotes the direction of action while the second denotes the section plane. The curvature is zero, thus, there is no constitutive moment. The moment resulting from the non-symmetric stress tensor is in balance with an external moment resulting from the constraint.

$$\sigma_{12}^L = (D_{33} - D_{44})\alpha \quad (55a)$$

$$\sigma_{21}^L = (D_{33} - 2D_{34} + D_{44})\alpha \quad (55b)$$

A second set of equations is obtained by considering the load case where the fiber cross-section is free to rotate, and symbols referring to this case are furnished with an overscript F . The homogenized solid responds like a Cauchy solid in this situation, i.e. the symmetric part of shear stress $\frac{1}{2}(\sigma_{12}^F + \sigma_{21}^F)$ should be determined by the conventional shear modulus G_{II} and the asymmetric stress $\frac{1}{2}(\sigma_{12}^F - \sigma_{21}^F)$ must vanish. It is important to notice that the rotation of the fiber cross-section φ^F is determined by the fibers shear flexibility, hence, it differs from the rotation of the fiber axis which corresponds to α .

$$G_{II}\alpha = (D_{33} - D_{34})\alpha + 2D_{34}\varphi^F \quad (56a)$$

$$0 = (D_{34} - D_{44})\alpha + 2D_{44}\varphi^F \quad (56b)$$

Next, the intermediate constants σ_{21}^L, φ^F , and G_{II} are related to properties of the constituents via an analytical micromechanics approach. In the locked shear case, the shear angles in both fiber and matrix coincide with α . Hence,

the corresponding stress is given by $\sigma_{21}^L = (v^{\text{fib}}G^{\text{fib}} + (1 - v^{\text{fib}})G^{\text{mat}})\alpha$, where $G^{\text{fib}}, G^{\text{mat}}$ are the fiber and matrix shear moduli and v^{fib} is the fiber volume content. For the free shear case, the applied shear stress is symmetric $\sigma_{12}^F = \sigma_{21}^F = G_{II}\alpha$. In a 2-dimensional setting, shear stress coupling between fiber and matrix may be assumed so that the rotation of the fiber cross-section from the vertical can be stated as $\varphi^F = (1 - G_{II}/G^{\text{fib}})\alpha$, i.e. it will be slightly less than α . Moreover, the conventional shear modulus can be expressed as $1/G_{II} = v^{\text{fib}}/G^{\text{fib}} + (1 - v^{\text{fib}})/G^{\text{mat}}$. Subsequently, σ_{12}^L can be eliminated from the 4 equations in (55) and (56), and the remaining equations can be solved for D_{33}, D_{34}, D_{44} , see (57). In the limit case of zero fiber volume fraction $v^{\text{fib}} \rightarrow 0$ the micropolar solid reverts back to a Cauchy solid for the pure matrix with $D_{33} \rightarrow G^{\text{mat}}$ and $D_{34} \rightarrow D_{44} \rightarrow 0$.

$$\sigma_{12}^L = G^{\text{mat}}\alpha \quad (57a)$$

$$D_{33} = \frac{1}{4} \left(\frac{(2 - v^{\text{fib}})^2 G^{\text{mat}}}{1 - v^{\text{fib}}} + v^{\text{fib}} G^{\text{fib}} \right) \quad (57b)$$

$$D_{34} = \frac{v^{\text{fib}}}{4(1 - v^{\text{fib}})} \left((2 - v^{\text{fib}})G^{\text{mat}} - (1 - v^{\text{fib}})G^{\text{fib}} \right) \quad (57c)$$

$$D_{44} = \frac{v^{\text{fib}}}{4(1 - v^{\text{fib}})} \left(v^{\text{fib}} G^{\text{mat}} + (1 - v^{\text{fib}})G^{\text{fib}} \right) \quad (57d)$$

4.2. Hardening law

In subsequent sections, the micropolar modeling approach is compared against micromechanical and analytical reference models. The hardening law for the matrix plasticity has a strong impact on the MB-strength, and care must be taken to ensure the comparability of the various types of models.

In the micromechanical reference models, both fibers and matrix are assumed isotropic and matrix plasticity is represented by isotropic J_2 -plasticity. Matrix hardening is isotropic and obeys the power law (58) for monotonic loading. The equation relates the plastic shear angle in the matrix $(\gamma_{12}^{\text{mat}})^p$ to the respective shear yield stress σ_{12}^{mat} in an uniaxial shear test. Symbol G^{mat} represents the matrix shear modulus and τ_y and n are plasticity parameters, their numeric values are stated in Table 2. The threshold for initial yielding was set at $\sigma_{12}^{\text{mat}} = 20$ MPa. The peak load is sensitive to the parameters τ_y and n , but not the initial yield strength. This is because plastic strain remains quite small after initial yielding and only becomes substantial at higher shear stress. The micromechanical reference models were solved in Simulia/Abaqus. The input material card for the hardening law in this software requires a translation of (58) to a relation of the equivalent plastic strain to the von Mises stress and the respective conversion factors were taken into account.

$$(\gamma_{12}^{\text{mat}})^p = \frac{3\tau_y}{7G^{\text{mat}}} \left(\frac{\sigma_{12}^{\text{mat}}}{\tau_y} \right)^n \quad (58)$$

In the micropolar medium fiber and matrix are smeared out, the hardening law must be specified in terms of the homogenized plastic shear angle γ_{12}^p and the homogenized shear stress σ_{12} . Assuming shear rigid fibers and moderate deformation, the homogenized plastic shear angle is related to the matrix shear angle by the kinematic relation $(\gamma_{12}^p)^{\text{mat}} = \gamma_{12}^p / (1 - v^{\text{fib}})$, where v^{fib} is the fiber volume fraction. To obtain a strictly increasing hardening variable, the symbol q was introduced in Section 3.7, its rate obeys $\dot{q} = |\dot{\gamma}_{12}^p|$. Moreover, the shear yield stress in the micropolar solid is by designated S , thus, the hardening law equivalent to (58) for the micropolar solid is given by (59). The approximation stated there follows from neglecting fiber shear flexibility which is admissible for the purpose of defining the hardening law. For the fiber volume fraction of 50%, the equivalent plastic strain in the matrix, Abaqus output variable PEEQ in the figures shown further down, is related to q via $\text{PEEQ} = 2/\sqrt{3}q$.

$$q = \frac{3(1 - v^{\text{fib}})\tau_y}{7G^{\text{mat}}} \left(\frac{S}{\tau_y} \right)^n \approx \frac{3\tau_y}{7G_{II}} \left(\frac{S}{\tau_y} \right)^n \quad (59)$$

The peculiar form (58) was chosen to facilitate comparison to classical closed form estimates for the peak load, which will be considered in Section 5.1. In closed form analysis, typically a deformation theory of plasticity

Table 2

Properties for fiber and matrix constituents used in the micromechanical reference model. The values approximately correspond to a carbon fiber/epoxy prepreg UD300/M79.

fiber, isotropic				matrix, isotropic			
slice thickness	volume fraction	Young's modulus	Poisson's ratio	Young's modulus	Poisson's ratio	parameter τ_y	parameter n
5 μm	50%	250 GPa	0.3	5 GPa	0.3	40 MPa	6

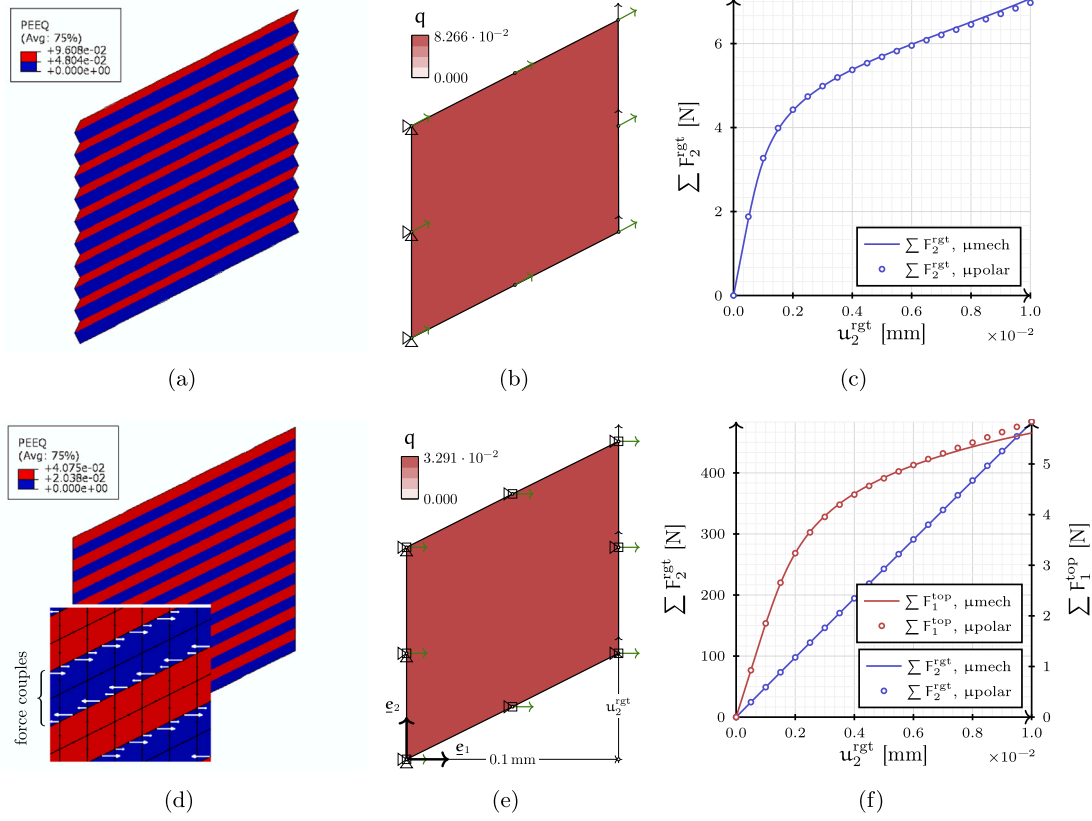


Fig. 6. Meshes and load–displacement diagrams for the shear tests. (a), (d): micromechanical reference model solved in Simulia/Abaqus; (b), (e): results obtained from an implementation of the present micropolar formulation; (a) to (c): shear with free micro rotation; (d) to (f): shear with locked micro rotation; Green arrows emanating from nodes indicate the rotated fiber direction vector α . Symbols $\sum F_2^{\text{rgt}}$ and $\sum F_1^{\text{top}}$ represent the total of the vertical nodal forces on the right and the total of the horizontal nodal forces on the top boundary, respectively. All meshes are shown with a linear scaling by a factor of $(n^{\text{fib}}/l)E^{\text{fib}}I^{\text{fib}} = 0.260 \text{ N mm}$ applied to displacements, and also rotations for (b) and (e). (For interpretation of the references to color in this figure legend, the reader is referred to the web version of this article.)

is adopted to represent the matrix nonlinearity from a homogenized vantage point. Following Ref. (Budiansky and Fleck, 1993), the Ramberg–Osgood relation (60) will be used in the context of the closed form peak load formulae discussed further down. The symbol γ_{12} denotes the total shear angle of the homogenized solid, i.e. $\gamma_{12} = \sigma_{12}/G_H + \gamma_{12}^p$.

$$\gamma_{12} = \frac{\sigma_{12}}{G_H} \left(1 + \frac{3}{7} \left(\frac{\sigma_{12}}{\tau_y} \right)^{n-1} \right) \quad (60)$$

4.3. Bending stiffness and verification

To verify the micropolar model in the elastic and plastic regime it is compared against results of a micromechanical finite element model for the two calibration shear load cases considered in Section 4.1 and a third load case involving bending. For this purpose, numeric values for the properties of the constituents are adopted, see Table 2. The particular numerical values listed there correspond to a carbon fiber/epoxy prepreg UD300/M79. For the comparison a square domain of size $0.1 \text{ mm} \times 0.1 \text{ mm}$ containing 10 fibers with a volume fraction of 50% is considered. Compatible deformation is enforced via periodic boundary conditions. Due to the periodicity of the model, size has no effect on the resulting effective properties. In the micromechanical reference model, fiber and matrix phases are explicitly

represented by alternating slices. The thickness of the fiber slices corresponds to the fiber diameter only approximately, since the segmentation was adjusted to match a given fiber volume content.

Results obtained from micromechanical and micropolar models are compared in Fig. 6 for the two shear load cases defined in Section 4.1. The shear is applied via a prescribed vertical displacement by u_2^{rgt} on the right boundary and the resulting reaction forces are tracked to obtain the effective stress response. In the micropolar solid the strain is completely homogeneous, therefore, the domain is discretized by a single element. Results for the free shear load case are shown in Fig. 6(a) to (c). In the micromechanical model the periodicity constraints enforce the overall shear deformation, but still allow the fiber cross-section to rotate freely, see Fig. 6. Correspondingly, the rotational degree of freedom was left unconstrained in all nodes for the micropolar model. The locked shear load case is shown in (d) to (f). In that case displacement in direction 1 is suppressed at all nodes for both the micromechanical and the micropolar models. In the micromechanical model the condition of zero displacement in direction 1 prevents the fiber cross-section from rotating, in the micropolar model the same is implemented by constraining φ to zero. The condition of zero displacement in direction 1 acting on the interior of the micro model does not effect a source or sink of force-stress (as seen from a micropolar vantage point), since the reaction forces at the interior nodes occur as force couples

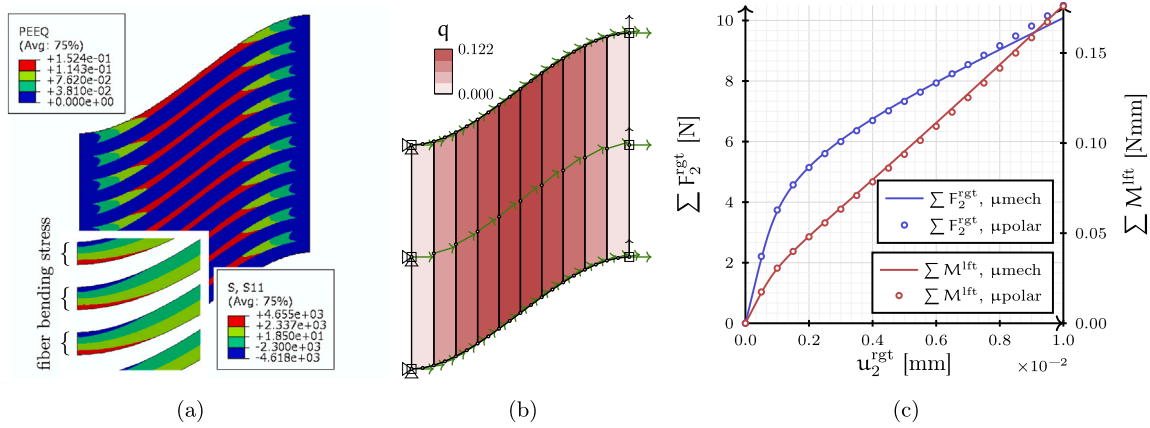


Fig. 7. Meshes and load–displacement diagram for the bending load case. All meshes are plotted in the same manner as in Fig. 6; (a): micromechanical reference model, the inset shows σ_{11} for the fiber only; (b): micropolar model; Symbol $\sum F_2^{rgt}$ represents the total of the vertical nodal forces on the right and $\sum M^{lft}$ represents the total reaction moment on the left boundary.

in such a manner that their total cancels out. Even so, the force couples render a non-zero total moment acting on the interior, thus the condition implements a moment-stress source, see inset to Fig. 6(d). The need for such an external moment density to arise in the locked shear load case was already mentioned in Section 4.1. The elastic shear stiffness of the fiber is much larger than the shear stiffness of the elastoplastic matrix, hence, there is large difference in the reaction forces on the right and the top boundary of the model, see (f). Inspecting force–displacement diagrams (c) and (f) shows a good match between micromechanical and micropolar models in both the elastic and plastic regime.

With the force stress elasticity constants accounted for, the only remaining constant is ζ_2 , since ζ_1 has already been eliminated. The constant ζ_2 quantifies bending resistance and has no effect in any of the tests discussed above because the rotation is homogeneous over the domain in all of them. A suitable test with inhomogeneous rotation and, hence, nonzero wryness, is shown in Fig. 7. The reference model is finely discretized using about 6400 elements, the micropolar mesh comprises only 10 elements. In this test again a displacement u_2^{rgt} at the right vertical edge is applied, however, micro rotation is now suppressed only at the left and right vertical edges but not in the interior. To enforce the no micro rotation condition on the micromechanical model, the left and right edges are rigid so that the fiber cross-section cannot rotate there. On the top and bottom boundaries periodicity conditions are still in place in both models, resulting in a smooth variation of φ along the horizontal direction. Although the micromechanical model has no notion of couple stress, a nonzero reaction moment results from the inhomogeneous distribution of the force stress σ_{11} on the vertical edges, see inset of Fig. 7(a). The right edge is free to translate horizontally, so the net force resulting from σ_{11} is zero. There is, however, a nonzero net moment due to the bending stress in the fibers. This net moment was extracted from the micromechanical model by multiplying the nodal reaction force at the rigid boundary with its respective lever arm. Since the net horizontal force is zero, the reference point for the lever arm has no effect on the result. In this manner the total reaction moment on the vertical edges was extracted from the micromechanical model, see in Fig. 7(c). The specific bending stiffness ζ_2 of the micropolar solid may be estimated by $(n^{fib}/l)E^{fib}I^{fib} = 0.260$ N mm, where $n^{fib} = 10$ is the number of fibers over the length $l = 0.1$ mm and $E^{fib}I^{fib}$ is the bending stiffness of a single fiber. However, a better match to the micromechanical reference is obtained with a slightly smaller value of $\zeta_2 = 0.245$ N mm which is used in all subsequent calculations. The small difference is likely caused by bending stress in the matrix. From Fig. 7(c) it is apparent that the total of the nodal forces $\sum F_2^{rgt}$ on the right edge as a reaction to the applied displacement u_2^{rgt} is matched well in this load case without any further adjustments.

5. Microbuckling simulations

5.1. Comparison to classical peak load estimates

With the micropolar model fully calibrated, it is ready to be applied to microbuckling problems. The first application is a comparison of the micropolar model against the classical peak load formula given by Budiansky and Fleck (Budiansky and Fleck, 1993), see (61). This formula considers a zero-dimensional material point under uniform far field compression and with an uniform preexisting fiber misalignment angle θ relative to the axis of compression. It predicts the peak compressive stress R which initiates microbuckling. Another input is the nonlinear shear stress/shear strain relation $\sigma_{12}(\gamma_{12})$ which is inversely given by (60). The operator $\max_{\gamma_{12}}$ denotes that the argument is to be maximized with respect to γ_{12} , which is performed numerically.

$$R = \max_{\gamma_{12}} \left(\frac{\sigma_{12}(\gamma_{12})}{\theta + \gamma_{12}} \right) \quad (61)$$

Since (61) assumes that all quantities are uniform, the corresponding micropolar model comprises only a single element. The initial misalignment θ is implemented by rotating the initial orientation of the director \underline{A} by the respective amount. The model is then loaded by an uniform compressive load $-\sigma_{11}$ along the zero degree axis so that the peak load R is exceeded, see Fig. 8(a). For small initial misalignment angles θ , the characteristic snap-back response necessitates the use of an arc-length solution scheme. The peak load values obtained from the micropolar model is compared the corresponding prediction by (61) for a range of initial misalignments in Fig. 8(b) showing good agreement.

5.2. Comparison to a micromechanical model

To verify the suitability of the micropolar model for microbuckling problems in a 2-dimensional setting it is compared to another micromechanical reference model. Additionally, results obtained from a homogenized model based on conventional continuum theory are presented to demonstrate the deficiencies of that approach. All three models consider a square domain of side length $l = 0.5$ mm under plane strain. In the micromechanical model, the domain contains 50 fiber slices. The nominal fiber direction is aligned with \underline{e}_1 , however, a small preexisting misalignment by angle θ acts as imperfection. The imperfection has the form of a half period of a sine wave over the model domain with an amplitude of $\Theta = 2^\circ$, see (62).

$$\theta = \Theta \sin\left(\pi \frac{x_1}{l}\right) \quad (62)$$

It is noted that the fiber undulation wave length is 1 mm, i.e. on the order of 200 fiber diameters. In this situation, Refs. (Lemanski and Sutcliffe, 2012; Fleck and Shu, 1995) suggest that fiber bending stiffness has only minor

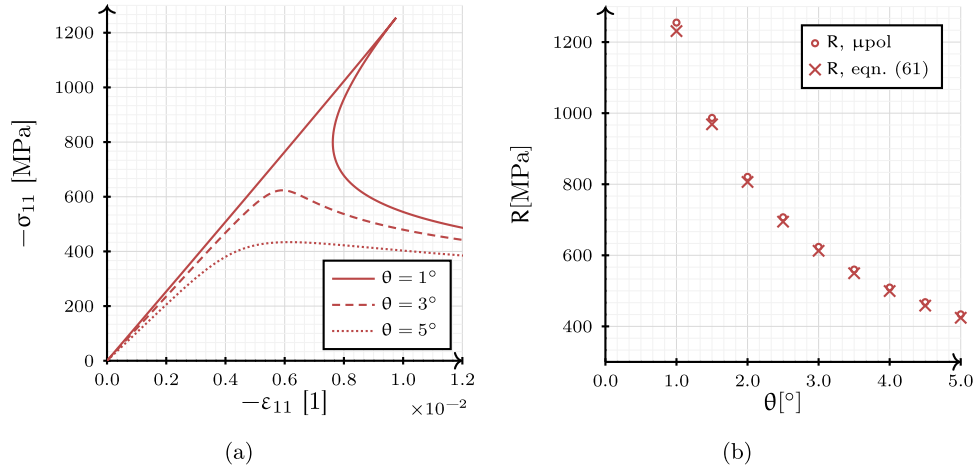


Fig. 8. Results for the single element MB-verification model. (a) shows relation of applied far field compression $-\sigma_{11}$ to compressive strain $-\epsilon_{11}$, (b) shows a comparison of peak loads as obtained from the micropolar model to results calculated from (61).

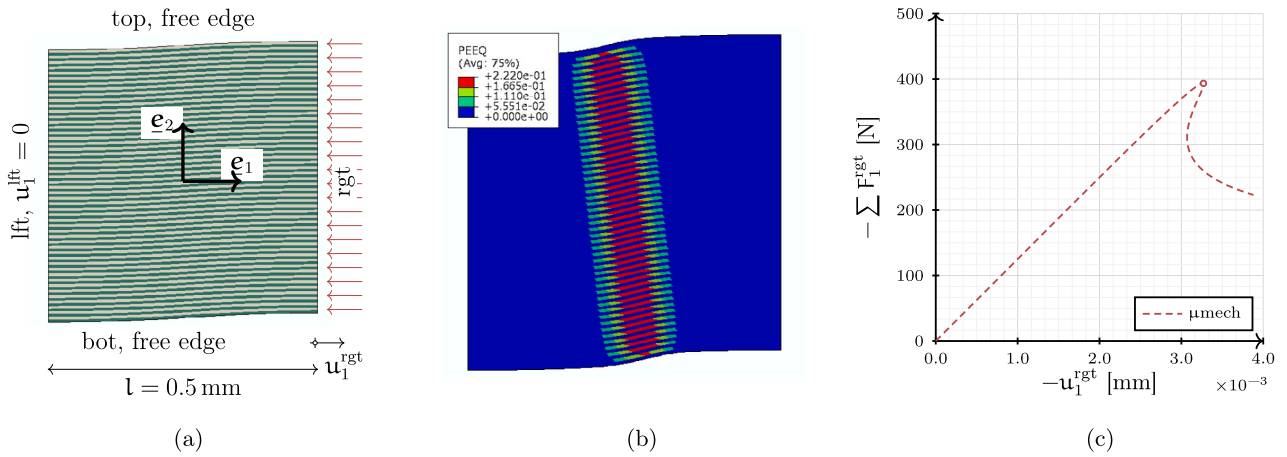


Fig. 9. Undeformed mesh (a), mesh at maximal deformation (b), and load-displacement diagram (c) for the micromechanical reference model. Displacements are to scale and not magnified. Symbol $-\sum F_1^{rgt}$ is the total compressive force applied to the right boundary. The point marker denotes the peak in the load-displacement diagram.

or negligible effect on the peak load. In the micromechanical reference model fibers are explicitly modeled. The fiber geometry equivalent to (62) is generated by applying a stress-free pre-deformation of $u_2^{mi} = \int \theta dX_1$. The conventionally homogenized model requires an anisotropic plasticity model to prevent the solid from yielding in fiber direction. Here, this is implemented by using a Hill-type anisotropic plasticity model where all yield strengths except for the in-plane shear strength are set so large that they may be ignored. This results in plastic behavior comparable to the one discussed in Section 3.7. In the conventionally homogenized model, θ rotates the initial orientation of the material principal axes. In the micropolar model, θ defines the initial orientation of the director $\underline{A}^T = \begin{bmatrix} \cos(\theta) & \sin(\theta) \end{bmatrix}$.

Load is applied in form of a homogeneous uniaxial compression in nominal fiber direction at the right vertical edge, see Fig. 9(a). Horizontal displacement is fixed on the left edge and the top and bottom edges are traction free. The same boundary conditions apply to all three models. In the micromechanical reference model, the reaction force is essentially linear until a load peak at 393 N, followed by snap-back collapse, see Fig. 9(c). It is noted that the arc-length procedure renders the quasi-static equilibrium path, however, in nature MB is a dynamic process and the quasi-static solution is merely an approximation. The simulation is stopped at a displacement $-u_1^{rgt} = 4.0 \times 10^{-3}$ mm, since the maximum shear stress in the matrix has increased to about 70 MPa at this point and thus exceeds the matrix fracture stress for the material adopted here. The width of the band of plastic deformation is well defined as apparent from Fig. 9(b) and

corresponds to about 25 fiber slices. It does not conform to the band of initial misalignment which extends over the entire model. Moreover it is inclined at an angle of about 8° to the vertical.

Attempting to replicate the results of the micromodel with an conventionally homogenized model results in several problems, see Fig. 10. The bandwidth obtained from this kind of model is sensitive to the discretization size, compare Figs. 10(a) and 10(b), and does not match the width observed in the micromechanical model. The mesh dependence also affects the load-displacement response in the softening regime which is rather erratic as apparent from Fig. 10(c). There 3 different discretizations are considered, the two shown in the figure and an intermediate one. All deviate from the micromechanical reference. It is also noteworthy that the homogenized approach overestimates the peak load, rendering peak loads between 445 N and 460 N compared to 393 N for the micromodel. There are 2 causes for this overestimation of the peak load in the homogenized models: The main cause is that in the finite element software Abaqus the rotation of the principal material axes is implemented in such a way that it accounts only for the rigid body rotation of the deformation, i.e. for simple shear by angle α the material axis rotate only by $\alpha/2$. As a result, in this software the rotation of the principal material axis lags behind the actual fiber rotation and the peak load is overestimated. This limitation was first reported in Wisnom (1993). It is shown further down that the micropolar model does not suffer from this limitation. A secondary cause of the overestimation is that the effect of compressive stress on matrix yielding is not considered. This is a relatively minor effect, due to the large difference in stiffness between matrix and

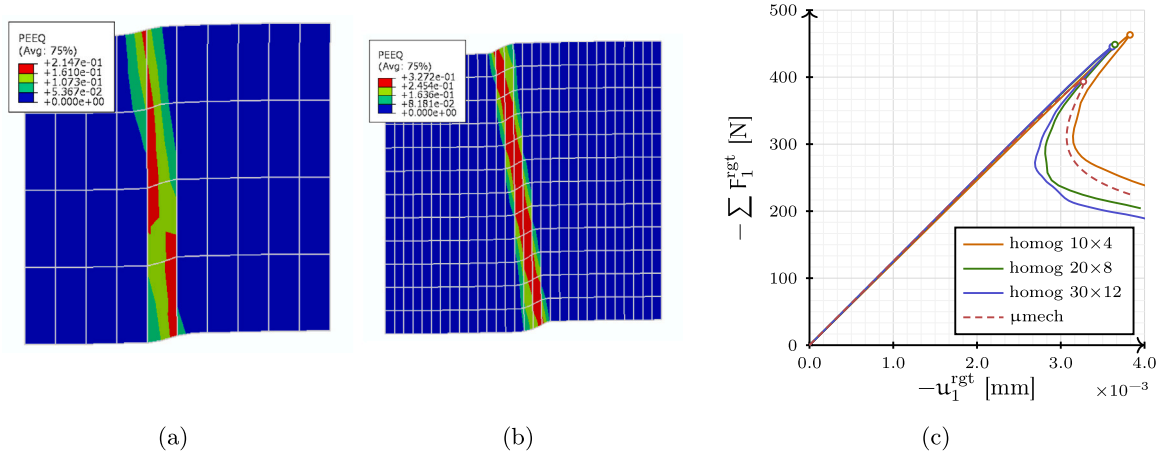


Fig. 10. Meshes 10×4 (a), 30×12 (b), and load–displacement diagram (c) for a conventionally homogenized model. The point markers denote at the peaks in the load–displacement diagram. Notice the overestimation of the peak load and the erratic load–displacement relation in the softening regime.

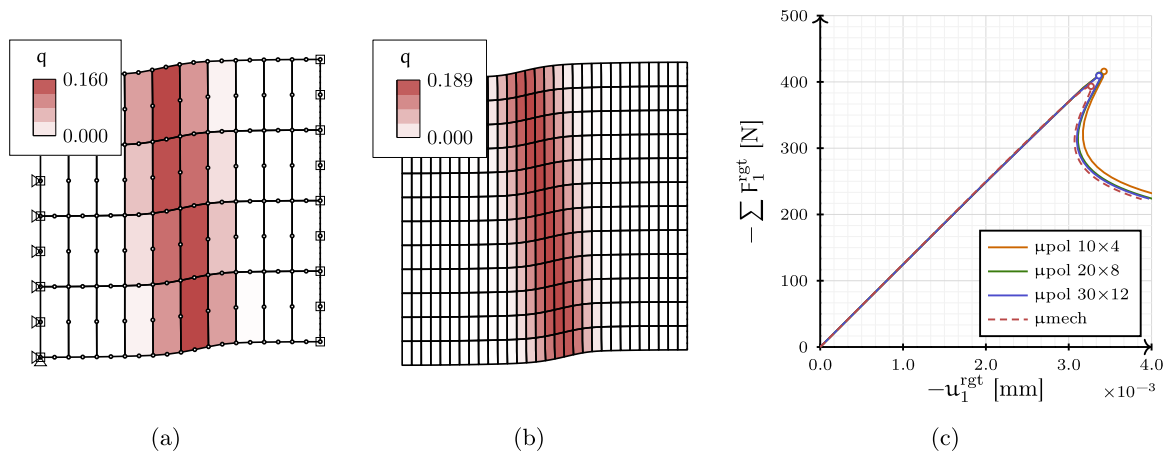


Fig. 11. Meshes 10×4 (a), 30×12 (b), and load–displacement diagram (c) for the micropolar model. The point markers denote at the peaks in the load–displacement diagram. The deformation and the load–displacement response converge to the reference on mesh refinement (a) to (c).

fiber which effectively shields the matrix from longitudinal stress so that yielding is dominated by shear stress.

The micropolar approach correctly replicates the micromechanical reference model, both with regard to the deformation as well as the load–displacement response, see Fig. 11. The bandwidth is well defined even for the very coarse mesh in Fig. 11(a) and it is about the same as in the micromechanical model. The load–displacement relation is smooth and closely matches the reference. A small difference to the reference is apparent with regard to the peak load, where the micropolar models predict between 415 N to 409 N, while the reference value is slightly smaller at 393 N. Like in the conventionally homogenized model, this discrepancy results from the neglect of the compressive stress in the plasticity model. More importantly, however, the micropolar model avoids the limitation regarding the rotation of the material axes present in the Abaqus implementation.

As a side note, the effect of the shear nonlinearity on the peak load is briefly discussed. For this purpose, simulations on the micropolar model without matrix plasticity were performed, all other conditions being the same as mentioned above. The models without plasticity render a very high peak load, at about 4 times the peak load of the model including plasticity. The post peak load behavior is different and no distinct strain localization occurs. This is expected, since the two properties with the strongest impact on microbuckling strength are fiber misalignment and the nonlinearity (plasticity) of the matrix shear response. Neglecting the latter has dramatic effects on the peak load and renders a model approximately in line with the elastic bifurcation theory for MB which was developed by

B. W. Rosen. This elastic bifurcation theory has historical relevance since it was developed as one of the very first approaches to the subject. It does not, however, provide a suitable model for MB and is known overestimate peak loads by about a factor of 4 for common materials. Ref. (Budiansky and Fleck, 1993) provides a good exposition of the elastic bifurcation theory and its shortcomings.

6. Summary and conclusion

The present contribution considered the adaptation of micropolar continuum theory for the application to microbuckling (MB) problems. The present approach is founded on the finite strain plasticity theory for generalized continua (Forest et al., 1997; Sievert et al., 1998; Forest et al., 2000; Forest and Sievert, 2003) to MB-problems, thus, distinguishing itself from other such adaptations (Fleck and Shu, 1995; Hasanyan and Waas, 2018a,b). On this basis, a finite strain elasto-plastic constitutive model and a corresponding finite element implementation were developed. A novel identification procedure for the additional parameters introduced by the micropolar solid was also presented and verified against a reference model. The resulting model allows the extension of simulations into the post peak load regime, which is required for the investigation of MB investigation of certain MB-specific phenomena like band broadening. The calibrated model was verified against a micromechanical reference, and it was shown to accurately predict bandwidth and band inclination. The peak load prediction was also found to be satisfactory. In contrast, a conventionally homogenized model gave an erratic response in the softening regime and also poorly

predicted the peak load due an implementation detail in the proprietary software Abaqus.

An avenue of further extension of the present approach is the consideration of additional failure modes in the softening regime like matrix rupture and fiber fracture. The fiber fracture aspect is of particular interest, since it has been proposed that it is initiated by bending stress, either compressive (Pinho et al., 2012b; Pimenta et al., 2009a) or tensile (Fleck et al., 1995; Budiansky et al., 1998; Guimard et al., 2007), see the discussion in Section 1. Detection of fiber failure is not possible in a conventionally homogenized approach where no measure of fiber bending exists. In a micropolar setting, however, the wryness quantifies curvature, thus, providing a handle for the formulation of a fiber bending failure criterion in a homogenized context. Another direction for future work is the application of the present approach to a realistic multi ply laminate modes with representative misalignment topologies in a 3 dimensional setting. An apparent challenge in this respect is that the mesh size is tied to the inherent length scale of the problem, i.e. it should not exceed about 10 times the fiber diameter or else the bandwidth cannot be resolved. Hence, the computational effort required to solve a coupon sized laminate model is expected to be substantial.

Declaration of competing interest

The authors declare that they have no known competing financial interests or personal relationships that could have appeared to influence the work reported in this paper.

References

- Bishara, M., Rolfes, R., Allix, O., 2017. Revealing complex aspects of compressive failure of polymer composites - Part I: Fiber kinking at microscale. *Compos. Struct.* 169 (Supplement C), 105–115, In Honor of Prof. Leissa.
- Budiansky, B., Fleck, N.A., 1993. Compressive failure of fibre composites. *J. Mech. Phys. Solids* 41 (1), 183–211.
- Budiansky, B., Fleck, N.A., 1994. Compressive kinking of fiber composites: A topical review. *Appl. Mech. Rev.* 47 (6S), S246–S250.
- Budiansky, B., Fleck, N., Amazigo, J., 1998. On kink-band propagation in fiber composites. *J. Mech. Phys. Solids* 46 (9), 1637–1653.
- Clarke, A., Archenhold, G., Davidson, N., Slaughter, W., Fleck, N., 1995. Determining the power spectral density of the waviness of unidirectional glass fibres in polymer composites. *Appl. Compos. Mater.* 2 (4), 233–243.
- Daum, B., Feld, N., Allix, O., Rolfes, R., 2019. A review of computational modelling approaches to compressive failure in laminates. *Compos. Sci. Technol.* 181, 107663.
- Davidson, P., Waas, A., 2016. Mechanics of kinking in fiber-reinforced composites under compressive loading. *Math. Mech. Solids* 21 (6), 667–684.
- Eidel, B., Gruttmann, F., 2003. Elastoplastic orthotropy at finite strains: multiplicative formulation and numerical implementation. *Comput. Mater. Sci.* 28 (3), 732–742, Twelfth International Workshop on Computational Mechanics of Materials.
- Feld, N., Allix, O., Baranger, E., Guimard, J.-M., 2011. Micro-mechanical prediction of UD laminates behavior under combined compression up to failure: influence of matrix degradation. *J. Compos. Mater.* 45 (22), 2317–2333.
- Fleck, N., 1997. Compressive failure of fiber composites. In: Hutchinson, J., Wu, T. (Eds.), *Advances in Applied Mechanics*. Academic Press, New York, NY, pp. 43–117.
- Fleck, N., Deng, L., Budiansky, B., 1995. Prediction of kink width in compressed fiber composites. *J. Appl. Mech.* 62 (2), 329–337.
- Fleck, N.A., Shu, J.Y., 1995. Microbuckle initiation in fibre composites : A finite element study. *J. Mech. Phys. Solids* 43 (12), 1887–1918.
- Forest, S., Barbe, F., Cailletaud, G., 2000. Cosserat modelling of size effects in the mechanical behaviour of polycrystals and multi-phase materials. *Int. J. Solids Struct.* 37 (46), 7105–7126.
- Forest, S., Cailletaud, G., Sievert, R., 1997. A cosserat theory for elastoviscoplastic single crystals at finite deformation. *Arch. Mech.* 49, 705–736.
- Forest, S., Sievert, R., 2003. Elastoviscoplastic constitutive frameworks for generalized continua. *Acta Mech.* 160 (1), 71–111.
- Guimard, J., Allix, O., Pechnik, N., Thevenet, P., 2007. Statistical energy and failure analysis of CFRP compression behavior using a uniaxial microbuckling model. *J. Compos. Mater.* 41 (23), 2807–2828.
- Gutkin, R., Pinho, S., Robinson, P., Curtis, P., 2010a. Micro-mechanical modelling of shear-driven fibre compressive failure and of fibre kinking for failure envelope generation in CFRP laminates. *Compos. Sci. Technol.* 70 (8), 1214–1222.
- Gutkin, R., Pinho, S., Robinson, P., Curtis, P., 2010b. On the transition from shear-driven fibre compressive failure to fibre kinking in notched CFRP laminates under longitudinal compression. *Compos. Sci. Technol.* 70 (8), 1223–1231.
- Hasanyan, A.D., Waas, A.M., 2018a. Compressive failure of fiber composites: A homogenized, mesh-independent model. *J. Appl. Mech.* 85 (9), 091001.
- Hasanyan, A.D., Waas, A.M., 2018b. Localization in anisotropic elastoplastic micropolar media: Application to fiber reinforced composites. *J. Mech. Phys. Solids* 121.
- Kessel, S., 1964. *Lineare Elastizitätstheorie des anisotropen Cosserat-Kontinuums*. In: *Abhandlungen der Braunschweigischen Wissenschaftlichen Gesellschaft*. H. Schaefer, pp. 1–22, in German.
- Kim, C.I., 2019. Strain-gradient elasticity theory for the mechanics of fiber composites subjected to finite plane deformations: Comprehensive analysis. *Multiscale Sci. Eng.* 1 (2), 150–160.
- Kyriakides, S., Arseculeratne, R., Perry, E., Liechti, K., 1995. On the compressive failure of fiber reinforced composites. *Int. J. Solids Struct.* 32 (6), 689–738, Time Dependent Problems in Mechanics.
- Lemanski, S., Sutcliffe, M., 2012. Compressive failure of finite size unidirectional composite laminates with a region of fibre waviness. *Composites A* 43 (3), 435–444.
- Liu, I.-S., 2002. *Continuum Mechanics*. Springer-Verlag Berlin Heidelberg GmbH.
- Liu, D., Fleck, N., Sutcliffe, M., 2004. Compressive strength of fibre composites with random fibre waviness. *J. Mech. Phys. Solids* 52 (7), 1481–1505.
- Miehe, C., 1996. Numerical computation of algorithmic (consistent) tangent moduli in large-strain computational inelasticity. *Comput. Methods Appl. Mech. Engrg.* 134 (3), 223–240.
- Nezamabadi, S., Potier-Ferry, M., Zahrouni, H., Yvonnet, J., 2015. Compressive failure of composites: A computational homogenization approach. *Compos. Struct.* 127 (Supplement C), 60–68.
- Pimenta, S., Gutkin, R., Pinho, S., Robinson, P., 2009a. A micromechanical model for kink-band formation: Part I - Experimental study and numerical modelling. *Compos. Sci. Technol.* 69 (7), 948–955.
- Pimenta, S., Gutkin, R., Pinho, S., Robinson, P., 2009b. A micromechanical model for kink-band formation: Part II - analytical modelling. *Compos. Sci. Technol.* 69 (7), 956–964.
- Pinho, S., Gutkin, R., Pimenta, S., De Carvalho, N., Robinson, P., 2012a. On longitudinal compressive failure of carbon-fibre-reinforced polymer: from unidirectional to woven, and from virgin to recycled. *Phil. Trans. R. Soc. A* 370 (1965), 1871–1895.
- Pinho, S., Gutkin, R., Pimenta, S., De Carvalho, N., Robinson, P., 2012b. On longitudinal compressive failure of carbon-fibre-reinforced polymer: from unidirectional to woven, and from virgin to recycled. *Philos. Trans. R. Soc. Lond. Ser. A Math. Phys. Eng. Sci.* 370 (1965), 1871–1895.
- Safdar, N., Daum, B., Rolfes, R., 2018. Stochastic compressive failure surface modelling for the unidirectional fibre reinforced composites under plainstress. In: *6th European conference on computational mechanics*, Glasgow.
- Schultheisz, C.R., Waas, A.M., 1996. Compressive failure of composites, part I: Testing and micromechanical theories. *Prog. Aerosp. Sci.* 32 (1), 1–42.
- Sievert, R., Forest, S., Trostel, R., 1998. Finite deformation cosserat-type modelling of dissipative solids and its application to crystal plasticity. *J. Physique IV* 8 (PR8), Pr8–357.
- de Souza Neto, E., Feng, Y., 1999. On the determination of the path direction for arc-length methods in the presence of bifurcations and 'snap-backs'. *Comput. Methods Appl. Mech. Engrg.* 179 (1), 81–89.
- Spencer, A., Soldatos, K., 2007. Finite deformations of fibre-reinforced elastic solids with fibre bending stiffness. *Int. J. Non-Linear Mech.* 42 (2), 355–368, Special Issue in Honour of Dr Ronald S. Rivlin.
- Steigmann, D.J., 2012. Theory of elastic solids reinforced with fibers resistant to extension, flexure and twist. *Int. J. Non-Linear Mech.* 47 (7), 734–742.
- Sutcliffe, M., 2013. Modelling the effect of size on compressive strength of fibre composites with random waviness. *Compos. Sci. Technol.* 88 (Supplement C), 142–150.
- Sutcliffe, M., Lemanski, S., Scott, A., 2012. Measurement of fibre waviness in industrial composite components. *Compos. Sci. Technol.* 72 (16), 2016–2023.
- Vinçon, I., Allix, O., Sigety, P., Auvray, M.-H., 1998. Compressive performance of carbon fibres: experiment and analysis. *Compos. Sci. Technol.* 58 (10), 1649–1658.
- Vogler, M., Rolfes, R., Camanho, P., 2013. Modeling the inelastic deformation and fracture of polymer composites - part I: Plasticity model. *Mech. Mater.* 59, 50–64.
- Waas, A.M., Schultheisz, C.R., 1996. Compressive failure of composites, Part II: Experimental studies. *Prog. Aerosp. Sci.* 32 (1), 43–78.
- Wisnom, M.R., 1993. Nonlinear analysis of misaligned unidirectional carbon fibre-epoxy compression specimens. *Compos. Eng.* 3 (6), 547–556.
- Xiao, H., Bruhns, O.T., Meyers, A., 2006. Elastoplasticity beyond small deformations. *Acta Mech.* 182 (1), 31–111.

Chapter V.

Towards component scale, an outlook

V.1. Measurement and image processing techniques

In Chapter III, Sec. 2 a large scale/low cost method of acquiring misalignment data from optical images on dry fiber material was presented. The foremost merit of this method is its ability to scan large areas at low cost, which is of major importance for a possible future application in an industrial environment. This aspect is also relevant for academic purposes, since it allows the collection of a large data set for statistical analysis. However, the method also suffers from several disadvantages. One disadvantage is that it operates on dry fiber material. The effects of compaction or infiltration on the misalignment require further investigation. Another shortcoming of the current method is that the imaging data is 2d and does not capture the out-of-plane undulation. An extension to 3d-surface data would be straightforward by extending the sensory equipment, e.g. using stereoscopic imaging or by adding a laser altimeter. In this way, out-of-plane undulations resulting from nesting effects in the layup of successive plies may be captured. Volumetric data may be subsequently reconstructed from the surface data of the ply interfaces in the laminate.

Processing of the image data obtained via such measurement may also be improved further. In Chapter III, Sec. 4 it has been noticed that the method of inferring misalignment from the roving edge used there tends to overestimate the misalignment. One particular reason for this overestimation was that this method is susceptible to the split roving manufacturing imperfection that causes a discontinuity in the detected roving edge, but does not necessarily cause a large misalignment of the actual fibers within the split roving. Hence, it appears desirable to detect the fiber direction directly from the image data, rather than infer it from the roving edge. As summarized in Subsec. 1.3.1 and Chapter III, Sec. 1.3 the development of image processing techniques to this end is a very active field of research. The application of the method proposed in Ref. [Kratmann et al., 2009] is examined here, pars pro toto. This and similar approaches operate on imaging data in frequency domain, hence there is a connection to the spectral representation method for misalignment topologies discussed in Subsec. 1.3.5. The technique is demonstrated on a 2048 by 2048 pixel 8-bit gray scale image taken by a conventional camera, see Fig. V.1(a). This raw image is subdivided into 32 by 32 tiles (indices K, L) of 64 by 64 pixels (indices k, l) each, see (b). Within each tile, individual fibers or small bundles of fibers appear as faint dark or bright streaks. Hence, the fluctuation of the gray value along the fiber direction is of much lower frequency than the frequency perpendicular to it. This observation can be exploited to automatically find the locally predominant fiber direction within each tile. The easiest way to do so is to transform the tile image to frequency domain where, greater fluctuation in fiber perpendicular direction results in a characteristic lobe of the spectral density perpendicular to the predominant fiber direction, see (c). The orientation of this lobe can be algorithmically found by maximizing an objective function $z(\tilde{\varphi}) = S[r, s]w[r, s](\tilde{\varphi})$ where $w[r, s]$ is a rotating mask of weights, see (d) and (e). Eventually the predominant fiber direction is found as the angle φ where z attains a maximum, see (f).

This method can be repeated for every tile K, L in the larger raw image (a). Several such images can be joined together to cover an extensive 2d-domain. The method is very robust and is not susceptible to other flaws or imaging artefacts like the black dot apparent in (b) Moreover, it succeeds even the tile is partially covered by the stitching yarn that has its own predominant fiber direction different from the roving's fiber direction, see Fig. V.2. In (b) the tiles intersected by the stitching yarn stand out due to

their much larger orientation angle $\varphi[K, L]$. In most applications, the stitching yarn orientation will not be relevant and will be filtered out. The gaps left by the filtering were filled in by interpolation from the neighbor tiles, see (c).

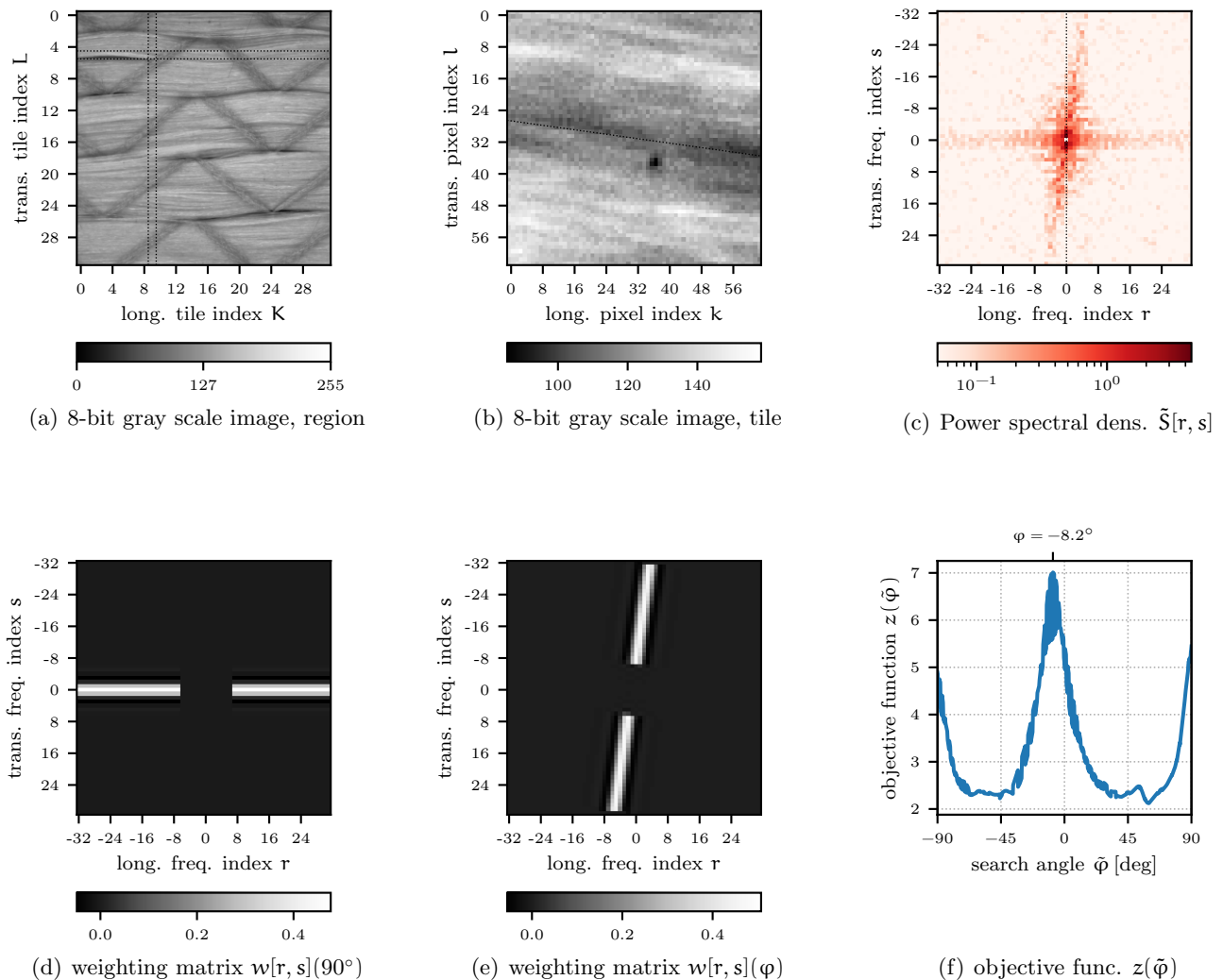


Figure V.1.: An extended image processing technique on the same material as shown in Chapter III, Fig. 1. Image (a) shows a region sized about 40 mm by 40 mm at a resolution of 2048 by 2048 pixels. It is subdivided into 32 by 32 tiles of 64 by 64 pixels each. One row and column of tiles is outlined by the 4 dotted lines. The image is encoded in the 8-bit gray scale format, where black corresponds to a numeric value of 0 and white to a value of 255. In (b) the tile $K = 9, L = 5$ is shown, see intersection of dotted lines in (a). The spectral density of this tile is shown in (c), notice the inclined lobe. The weighting matrix is shown in (d) and (e), and the objective function is shown in (f). A parallel to the identified fiber direction at -8.2° is drawn in (b) as a dotted line.

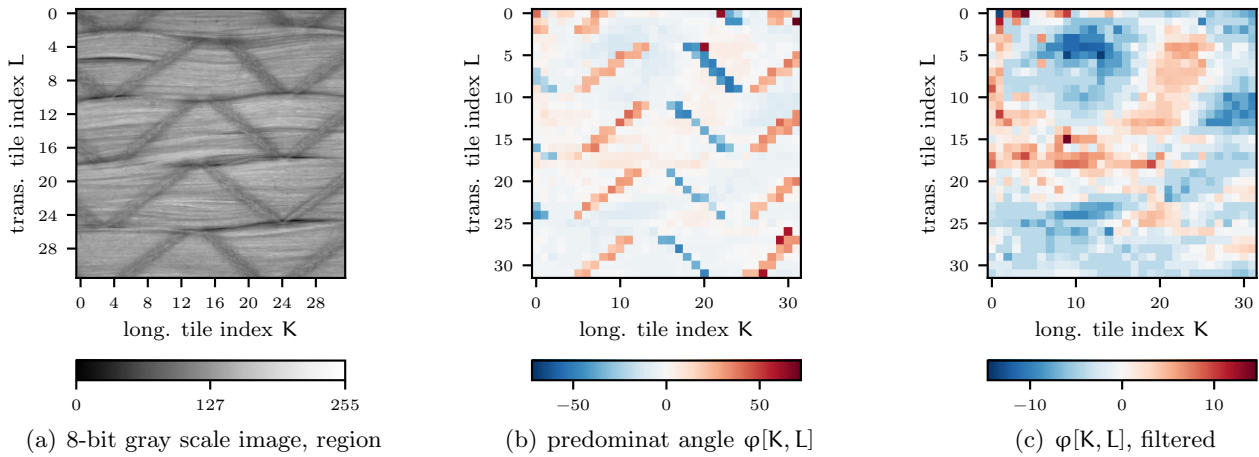


Figure V.2.: The same region as shown in Fig. V.1 is considered, and Subfigs. (a) are the same in both Figures. Subfig. (b) shows the raw result of the tile-wise application of the procedure to find the predominant angle $\varphi[K, L]$. The tiles covered by the stitching yarn stand out due to their large angle magnitude. In (c) all tiles with angles over 15° in magnitude were filtered out and replaced by values interpolated from the remaining tiles. The angle φ is measured from the nominal direction. The nominal direction is approximately, but not exactly, horizontal.

V.2. Surrogate modelling

Another avenue for further research follows the recent boom in machine learning techniques and regards their application as surrogate models. The basic concept is to employ the surrogate to quickly predict the expected strength from a measured misalignment topology, avoiding cumbersome discretization and numerical modelling. A prospective application would depend on large scale/low cost imaging technology similar to the one discussed in Sec. V.1 to acquire misalignment data, perhaps in a real-time industrial application integrated with the production process.

The basic concept is elaborated here by referring to a 2d-misalignment topology. The first step is to acquire a large set of training data of topologies $f[k, l]$, see Subsec. I.3.5, and their associated strength values. Since a huge data sets is required, the only feasible way of obtaining it is by numerical analysis. Moreover, if the number of input parameters is too large, the training effort will be excessive, hence, it is desirable to keep the number of input variables to a minimum. This may be accomplished by down-sampling the fully resolved misalignment topology $f[k, l]$ of size m by n to a coarser resolved topology $g[k, l]$ sized $p < m$ by $q < n$. The coarsest admissible resolution is given by the auto-correlation length. This matrix $g[k, l]$ then forms the input of the neuronal network which is to predict a real valued strength as the output, i.e. it is a model of the *regression* type. Problems where the input is provided via matrix values are common in image analysis, and for this purpose particular architectures of neural networks have emerged as pertinent. A common property of these architectures is that they involve one or several of *convolution* and *pooling* layers ahead of a fully connected network, see Fig. V.3. The main purpose of the convolution and pooling steps is to recognize particular features in the data, irrespective of the position of the feature within the data. In the present context, the features to look out for are regions of low local strength, either because of a large magnitude of misalignment at a particular location itself or because of constructive interaction of the location with its neighbors. Constructive interaction occurs when the direction of misalignment is the same within a local neighborhood, reducing the local strength, recall Subsec. I.3.3. In the convolution layer, the weights of a kernel matrix are trained so to extract the local severity. The size of this kernel determines how many neighbour pixels will be considered in this assessment.

For demonstration, a simple numerical example with a input matrix $g[k, l]$ of size $p = q = 9$ shall be considered. For simplicity, periodicity is assumed so that $g[k, l] = g[k + uq, l + vp]$ for any integers

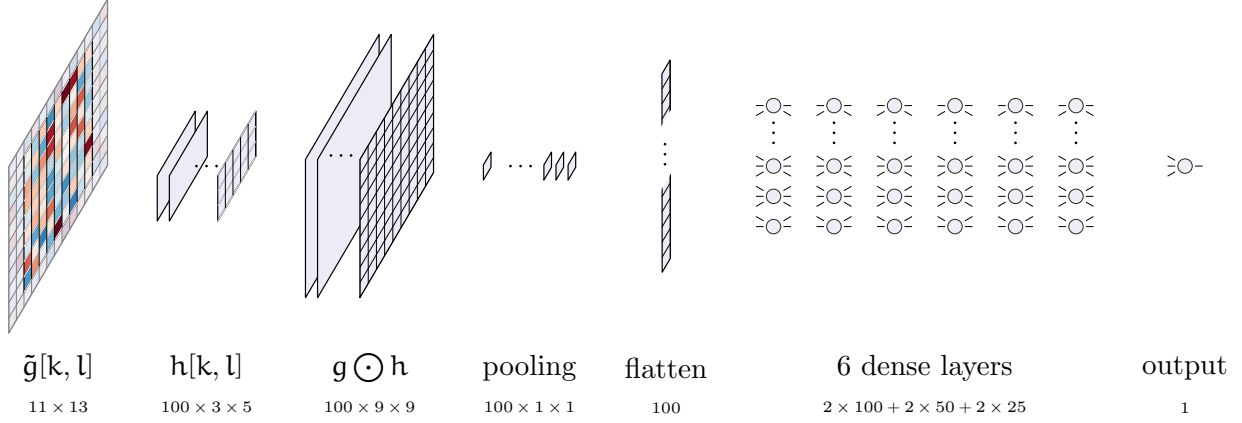


Figure V.3.: Convolutional network architecture; Symbols $g[k, l]$, $h[k, l]$, and $g \odot h$ stand for the padded input matrix, the kernel matrix, and their convolution, respectively. Network architectures specialized for image analysis often use several staged convolution and pooling layers. The particular network shown here was used in the numerical example and contains 31.251 parameters to be trained, in total.

u, v . The kernel $h[k, l]$ of the convolution layer was chosen to be of size 3 by 5, i.e. at each location two neighbors left/right and 1 neighbor up/down, respectively, will be considered for constructive/destructive interaction. In order to extend the convolution into the corners, the 9 by 9 matrix $g[k, l]$ was padded in a cyclic manner to render the 13 by 11 to matrix $\tilde{g}[k, l]$. In the first layer the convolution of $\tilde{g}[k, l]$ with 100 separate kernels $h[k, l]$ is performed, rendering the output $g \odot h$ of dimensions 100 by 9 by 9. Each of the 100 kernels is activated by a particular constellation of local interaction and the j^{th} -kernel maps the degree of severity of its constellation at a particular location k, l onto $(g \odot h)[j, k, l]$. A subsequent maximum pooling layer selects the location k, l of maximal activation for each kernel j , thus ensuring translation independence and reducing the output to a vector of length 100. This vector is then fed into a dense network of 6 layers that eventually produces a single output, the strength associated with the input topology $g[k, l]$. To train the network, a reference dataset of 67.5k misalignment topologies $g[k, l]$ with a standard deviation of 2 were generated. The corresponding strength to each topology was determined via finite element analysis. This dataset was then augmented by cyclic permutation and used to train the neural network. Subsequent validation shows that the demonstration network has learned to emulate the finite element reference model up to a mean absolute error of about 49.5 MPa, see Fig. V.4. Material parameters and shear nonlinearity are constant in the training data, and predictions refer to these material properties.

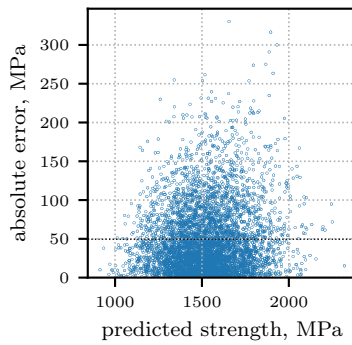


Figure V.4.: Scatter plot of absolute error overpredicted strength for 22.5k validation topologies. Each point represents a validation test. The mean absolute error is indicated by the dotted horizontal line at 49.5 MPa.

Bibliography of Chapters I and V

- [Argon, 1972] Argon, A. (1972). Fracture of composites, treatise of material science and technology (vol. 1, pp. 79-114).
- [Balacó De Morais, 1996] Balacó De Morais, A. (1996). Modelling lamina longitudinal compression strength of carbon fibre composite laminates. Journal of Composite Materials, 30(10):1115–1131.
- [Basu et al., 2006] Basu, S., Waas, A., and Ambur, D. (2006). Compressive failure of fiber composites under multi-axial loading. Journal of the Mechanics and Physics of Solids, 54(3):611 – 634.
- [Bednarczyk et al., 2014] Bednarczyk, B., Aboudi, J., and Arnold, S. (2014). The effect of general statistical fiber misalignment on predicted damage initiation in composites. Composites Part B: Engineering, 66:97 – 108.
- [Bishara et al., 2017] Bishara, M., Vogler, M., and Rolfes, R. (2017). Revealing complex aspects of compressive failure of polymer composites – part ii: Failure interactions in multidirectional laminates and validation. Composite Structures, 169(Supplement C):116 – 128. In Honor of Prof. Leissa.
- [Budiansky, 1983] Budiansky, B. (1983). Micromechanics. Computers & Structures, 16(1):3 – 12.
- [Budiansky and Fleck, 1993] Budiansky, B. and Fleck, N. (1993). Compressive failure of fibre composites. Journal of the Mechanics and Physics of Solids, 41(1):183 – 211.
- [Camarena et al., 2021] Camarena, E., Clarke, R. J., and Ennis, B. L. (2021). Development of a compressive failure model for carbon fiber composites and associated uncertainties. Composites Science and Technology, 211:108855.
- [Clarke et al., 1995] Clarke, A., Archenhold, G., Davidson, N., Slaughter, W., and Fleck, N. (1995). Determining the power spectral density of the waviness of unidirectional glass fibres in polymer composites. Applied Composite Materials, 2(4):233–243.
- [Evans and Adler, 1978] Evans, A. and Adler, W. (1978). Kinking as a mode of structural degradation in carbon fiber composites. Acta Metallurgica, 26(5):725 – 738.
- [Feld et al., 2011] Feld, N., Allix, O., Baranger, E., and Guimard, J.-M. (2011). Micro-mechanical prediction of ud laminates behavior under combined compression up to failure: influence of matrix degradation. Journal of Composite Materials, 45(22):2317–2333.
- [Fleck, 1997] Fleck, N. (1997). Compressive failure of fiber composites. In Hutchinson, J. and Wu, T., editors, Advances in applied mechanics, pages 43–117. New York, NY: Academic Press, 1948-.
- [Fleck et al., 1995] Fleck, N., Deng, L., and Budiansky, B. (1995). Prediction of kink width in compressed fiber composites. Journal of Applied Mechanics, 62(2):329–337.
- [Fleck and Shu, 1995] Fleck, N. and Shu, J. (1995). Microbuckle initiation in fibre composites: a finite element study. Journal of the Mechanics and Physics of Solids, 43(12):1887–1918.
- [Gutkin et al., 2010] Gutkin, R., Pinho, S., Robinson, P., and Curtis, P. (2010). Micro-mechanical modelling of shear-driven fibre compressive failure and of fibre kinking for failure envelope generation in cfrp laminates. Composites Science and Technology, 70(8):1214 – 1222.

- [Hasanyan and Waas, 2018a] Hasanyan, A. and Waas, A. (2018a). Compressive failure of fiber composites: A homogenized, mesh-independent model. Journal of Applied Mechanics, 85(9):091001–091001–15.
- [Hasanyan and Waas, 2018b] Hasanyan, A. D. and Waas, A. M. (2018b). Localization in anisotropic elastoplastic micropolar media: Application to fiber reinforced composites. Journal of the Mechanics and Physics of Solids, 121.
- [Hsu et al., 1999] Hsu, S.-Y., Vogler, T., and Kyriakides, S. (1999). On the axial propagation of kink bands in fiber composites : Part ii analysis. International Journal of Solids and Structures, 36(4):575 – 595.
- [Jelf and Fleck, 1994] Jelf, P. M. and Fleck, N. A. (1994). The failure of composite tubes due to combined compression and torsion. Journal of Materials Science, 29(11):3080–3084.
- [Jensen and Christoffersen, 1997] Jensen, H. and Christoffersen, J. (1997). Kink band formation in fiber reinforced materials. Journal of the Mechanics and Physics of Solids, 45(7):1121 – 1136.
- [Kratmann et al., 2009] Kratmann, K., Sutcliffe, M., Lilleheden, L., Pyrz, R., and Thomsen, O. (2009). A novel image analysis procedure for measuring fibre misalignment in unidirectional fibre composites. Composites Science and Technology, 69(2):228 – 238.
- [Kyriakides et al., 1995] Kyriakides, S., Arseculeratne, R., Perry, E., and Liechti, K. (1995). On the compressive failure of fiber reinforced composites. International Journal of Solids and Structures, 32(6):689 – 738. *Time Dependent Problems in Mechanics*.
- [Lemanski and Sutcliffe, 2012] Lemanski, S. and Sutcliffe, M. (2012). Compressive failure of finite size unidirectional composite laminates with a region of fibre waviness. Composites Part A: Applied Science and Manufacturing, 43(3):435 – 444.
- [Liu et al., 2004] Liu, D., Fleck, N., and Sutcliffe, M. (2004). Compressive strength of fibre composites with random fibre waviness. Journal of the Mechanics and Physics of Solids, 52(7):1481 – 1505.
- [Naik and Kumar, 1999] Naik, N. and Kumar, R. (1999). Compressive strength of unidirectional composites: evaluation and comparison of prediction models. Composite Structures, 46(3):299 – 308.
- [Newland, 2012] Newland, D. (2012). An Introduction to Random Vibrations, Spectral & Wavelet Analysis: Third Edition. Dover Civil and Mechanical Engineering. Dover Publications.
- [Niu and Talreja, 2000] Niu, K. and Talreja, R. (2000). Modeling of compressive failure in fiber reinforced composites. International Journal of Solids and Structures, 37(17):2405 – 2428.
- [Paluch, 1996] Paluch, B. (1996). Analysis of geometric imperfections affecting the fibers in unidirectional composites. Journal of Composite Materials, 30(4):454–485.
- [Piggott, 1981] Piggott, M. (1981). A theoretical framework for the compressive properties of aligned fibre composites. Journal of Materials Science, 16(10):2837–2845.
- [Pimenta et al., 2009] Pimenta, S., Gutkin, R., Pinho, S., and Robinson, P. (2009). A micromechanical model for kink-band formation: Part i — experimental study and numerical modelling. Composites Science and Technology, 69(7):948 – 955.
- [Prabhakar and Waas, 2013] Prabhakar, P. and Waas, A. (2013). Upscaling from a micro-mechanics model to capture laminate compressive strength due to kink banding instability. Computational Materials Science, 67(Supplement C):40 – 47.

- [Romanowicz, 2014] Romanowicz, M. (2014). Initiation of kink bands from regions of higher misalignment in carbon fiber-reinforced polymers. Journal of Composite Materials, 48(19):2387–2399.
- [Rosen, 1965] Rosen, B. (1965). Fiber composite materials. American Society for Metals, Metals Park, Ohio, page 37.
- [Safdar et al., 2022a] Safdar, N., Daum, B., and Rolfes, R. (2022a). A numerical prediction of failure probability under combined compression-shear loading for unidirectional fiber reinforced composites. Mechanics of Materials, 171:104352.
- [Safdar et al., 2020] Safdar, N., Daum, B., Rolfes, R., and Allix, O. (2020). The Representation of Fiber Misalignment Distributions in Numerical Modeling of Compressive Failure of Fiber Reinforced Polymers, pages 147–166. Springer International Publishing, Cham.
- [Safdar et al., 2022b] Safdar, N., Daum, B., Scheffler, S., and Rolfes, R. (2022b). Experimental determination of a probabilistic failure envelope for carbon fiber reinforced polymers under combined compression–shear loads. International Journal of Solids and Structures, 244-245:111585.
- [Schapery, 1995] Schapery, R. (1995). Prediction of compressive strength and kink bands in composites using a work potential. International Journal of Solids and Structures, 32(6):739 – 765. Time Dependent Problems in Mechanics.
- [Schuerch, 1966] Schuerch, H. (1966). Prediction of compressive strength in uniaxial boron fiber-metal matrix composite materials. AIAA journal, 4(1):102–106.
- [Schultheisz and Waas, 1996] Schultheisz, C. and Waas, A. (1996). Compressive failure of composites, part i: Testing and micromechanical theories. Progress in Aerospace Sciences, 32(1):1 – 42.
- [Skovsgaard and Jensen, 2018a] Skovsgaard, S. and Jensen, H. (2018a). Steady-state kink band propagation in layered materials. Journal of Applied Mechanics, 85(6).
- [Skovsgaard and Jensen, 2018b] Skovsgaard, S. P. and Jensen, H. M. (2018b). Constitutive model for imperfectly bonded fibre-reinforced composites. Composite Structures, 192:82 – 92.
- [Slaughter and Fleck, 1994] Slaughter, W. and Fleck, N. (1994). Microbuckling of fiber composites with random initial fiber waviness. Journal of the Mechanics and Physics of Solids, 42(11):1743 – 1766.
- [Sutcliffe, 2013] Sutcliffe, M. (2013). Modelling the effect of size on compressive strength of fibre composites with random waviness. Composites Science and Technology, 88(Supplement C):142 – 150.
- [Sutcliffe et al., 2012] Sutcliffe, M., Lemanski, S., and Scott, A. (2012). Measurement of fibre waviness in industrial composite components. Composites Science and Technology, 72(16):2016 – 2023.
- [Varandas et al., 2020] Varandas, L., Catalanotti, G., Melro, A., Tavares, R., and Falzon, B. (2020). Micromechanical modelling of the longitudinal compressive and tensile failure of unidirectional composites: The effect of fibre misalignment introduced via a stochastic process. International Journal of Solids and Structures, 203:157–176.
- [Vogler et al., 2001] Vogler, T., Hsu, S.-Y., and Kyriakides, S. (2001). On the initiation and growth of kink bands in fiber composites. Part II: analysis. International Journal of Solids and Structures, 38(15):2653–2682.
- [Wadee et al., 2012] Wadee, M., Völlmecke, C., Haley, J., and Yiatros, S. (2012). Geometric modelling of kink banding in laminated structures. Philosophical Transactions of the Royal Society of London A: Mathematical, Physical and Engineering Sciences, 370(1965):1827–1849.

- [Wilhelmsson and Asp, 2018] Wilhelmsson, D. and Asp, L. (2018). A high resolution method for characterisation of fibre misalignment angles in composites. Composites Science and Technology, 165:214 – 221.
- [Wilhelmsson et al., 2018] Wilhelmsson, D., Gutkin, R., Edgren, F., and Asp, L. (2018). An experimental study of fibre waviness and its effects on compressive properties of unidirectional ncf composites. Composites Part A: Applied Science and Manufacturing, 107:665 – 674.
- [Wind et al., 2014] Wind, J., Steffensen, S., and Jensen, H. (2014). Comparison of a composite model and an individually fiber and matrix discretized model for kink band formation. International Journal of Non-Linear Mechanics, 67:319 – 325.
- [Xu and Reifsnider, 1993] Xu, Y. L. and Reifsnider, K. L. (1993). Micromechanical modeling of composite compressive strength. Journal of Composite Materials, 27(6):572–588.
- [Yerramalli and Waas, 2004] Yerramalli, C. and Waas, A. (2004). The effect of fiber diameter on the compressive strength of composites-a 3d finite element based study. Computer Modeling in Engineering and Sciences, 6:1–16.
- [Yurgartis, 1987] Yurgartis, S. (1987). Measurement of small angle fiber misalignments in continuous fiber composites. Composites Science and Technology, 30(4):279 – 293.

Mitteilungen des Instituts für Statik und Dynamik der Leibniz Universität Hannover

1	R. Rolfes, C. Hühne	Eröffnungskolloquium (Tagungsband)	2005
2	H. Rothert, M. Kaliske, L. Nasdala	Entwicklung von Materialmodellen zur Alterung von Elastomerwerkstoffen unter besonderer Berücksichtigung des Sauerstoffeinflusses (DFG-Abschlußbericht)	2005
3	L. Nasdala	Simulation von Materialinelastizitäten bei Nano-, Mikro- und Makrostrukturen - Stabilitätsprobleme, Schädigungs- und Alterungsprozesse bei Kohlenstoffnanoröhren und Elastomerwerkstoffen (Habilitationsschrift)	2005
4	C. Hühne	Robuster Entwurf beulgefährdeter, unversteifter Kreiszyinderschalen aus Faserverbundwerkstoff (Dissertationsschrift)	2006
5	L. Nasdala, K.-U.Schröder	Finite Element Applications in Structural Analysis (Skript zur Hörsaalübung)	2006
6		Klausuraufgabensammlung, 4. Auflage	2007
7	R. Rolfes, W.-J. Gerasch, D. Rotert	Vorlesung Tragwerksdynamik	2007
8	K.-H. Elmer, K. Betke, Th. Neumann	Standardverfahren zur Ermittlung und Bewertung der Belastung der Meeresumwelt durch die Schallimmission von Offshore-Windenergieanlagen (Abschlussbericht zum BMU-Forschungsvorhaben)	2007
9	K.-U. Schröder	Zur nichtlinearen Berechnung von Stahlbeton- und Verbundbauteilen (Dissertationsschrift)	2007
10	G. Ernst	Multiscale Analysis of Textile Composites – Stiffness and Strength (Dissertationsschrift)	2008
11	G. Haake	Systemidentifikation mit Autoregressiven Modellen und Validierung numerischer Strukturmodelle bei Offshore-Windenergieanlagen (Dissertationsschrift)	2010
12	T. Griebmann	Dynamisches Tragverhalten von Stahlbetonbiegebalken im Experiment und in der Simulation (Dissertationsschrift)	2011
13	S. Zerbst	Global Approach for Early Damage Detection on Rotor Blades of Wind Energy Converters (Dissertationsschrift)	2011
14	N. Wieczorek	Semiaktive Schwingungsdämpfung leichter Fußgängerbrückenkonstruktionen (Dissertationsschrift)	2011
15	B. Kriegesmann	Probabilistic Design of Thin-Walled Fiber Composite Structures (Dissertationsschrift)	2012
16	J. Reetz	Schadensdiagnose an Tragstrukturen von Windenergieanlagen mit der Multiparameter-Eigenwertproblem-Methode (Dissertationsschrift)	2012
17	R. Rolfes, D. Rotert	Vorlesung Baustatik	2012
18	R. Rolfes, D. Rotert	Vorlesung Stabtragwerke	2012
19	H. Krüger	Ein physikalisch basiertes Ermüdungsschädigungsmodell zur Degradationsberechnung von Faser-Kunststoff-Verbunden (Dissertationsschrift)	2012
20	S. Czichon	Multi scale Failure Analysis of Fibre Reinforced Polymers with production induced Porosity Defects (Dissertationsschrift)	2013
21	T. Pahn	Inverse Load Calculation for Offshore Wind Turbines (Dissertationsschrift)	2013

22	M. Fricke, B. Neddermann, A. Lübben, J. Gabriel	Realistische Hydroschallszenarien auf der Basis von Prognosemodellen und Monitoring für den Bau von Offshore-Windparks in der deutschen Nordsee („HyproWind“) (Abschlussbericht zum BMU-Forschungsvorhaben)	2014
23	M. Vogler	Anisotropic Material Models for Fiber Reinforced Polymers (Dissertationsschrift)	2014
24	M. Fricke	Ein physikalisch basiertes Gesamtmodell für hydroakustische Immissionsprognosen bei Offshore-Pfahlrammungen (Dissertationsschrift)	2015
25	M. Häckell	A holistic evaluation concept for long-term structural health monitoring (Dissertationsschrift)	2015
26	J. Rustemeier	Optimierung von Blasenschleiern zur Minderung von Unterwasser-Rammschall (Dissertationsschrift)	2016
27	S. Hühne	A two-way loose coupling procedure for buckling and damage analysis of composite structures (Dissertationsschrift)	2016
28	A. Meurer	Filtering Geometric Imperfection Patterns for Analysis and Design of Composite Shell Structures (Dissertationsschrift)	2017
29	A. Dean	Material Modeling of Short Fiber Reinforced Polymeric Composites: Theory, Numerical Aspects, and Applications (Dissertationsschrift)	2017
30	M. Bishara	Compressive Failure of Polymer Composites Including Fiber Kinking and Interaction of Failure Mechanisms (Dissertationsschrift)	2017
31	K. Schröder	Advanced Model Updating Strategies for Structural Dynamic Systems (Dissertationsschrift)	2018
32	S. Tsiapoki	Transmissibility-Based Monitoring and Combination of Damage Detection Decisions within a Holistic Structural Health Monitoring Framework (Dissertationsschrift)	2018
33	S. R. Nabavi	Failure analysis of polycrystalline silicon-based photovoltaic modules considering the effects of residual stresses and mechanical loading (Dissertationsschrift)	2018
34	S. Scheffler	Ein neuer Modellierungsansatz zur systematischen numerischen Untersuchung des Versagensverhaltens von Verbindungen in FVK (Dissertationsschrift)	2018
35	J. Häfele	A numerically efficient and holistic approach to design optimization of offshore wind turbine jacket substructures (Dissertationsschrift)	2019
36	C. Hübler	Efficient probabilistic analysis of offshore wind turbines based on time-domain simulations (Dissertationsschrift)	2019
37	M. Akterskaia	Global-local progressive failure analysis of composite panels including skin-stringer debonding and intralaminar damage (Dissertationsschrift)	2019
38	C. Gebhardt	Robust computational procedures for the nonlinear dynamic analysis of beam and shell structures (Habilitationsschrift)	2020
39	A. Halder	Multistable morphing structures using variable stiffness laminates (Dissertationsschrift)	2020
40	R. Unger	Multi-scale constitutive modelling of nanoparticle/epoxy nanocomposites: Molecular simulation-based methods and experimental validation (Dissertationsschrift)	2020
41	J. Fankhänel	A Multi-Scale Framework for Nanocomposites including Interphase and Agglomeration Effects (Dissertationsschrift)	2020
42	N. Penner	Monitoring ambient angeregter baodynamischer Systeme durch mehrschichtige Perzeptren (Dissertationsschrift)	2021

43	C. Gerendt	A finite element-based continuum damage model for mechanical joints in fiber metal laminates under static and fatigue loading: Theory and experimental validation (Dissertationsschrift)	2022
44	M. Brod	Damage prediction of unidirectional fiber composites under cyclic loading with different amplitudes (Dissertationsschrift)	2022
45	R. Berger	Multi-Objective Structural Optimization of Repairs of Blisk Blades (Dissertationsschrift)	2022
46	G. Balokas	Metamodel-based uncertainty quantification for the mechanical behavior of braided composites (Dissertationsschrift)	2022
47	S. Wernitz	Damage Localization in Data-Driven Vibration-Based Structural Health Monitoring Using Linear Quadratic Estimation Theory (Dissertationsschrift)	2022
48	B. Daum	On the computational analysis of microbuckling via mesoscale approaches (Habilitationsschrift)	2022

Curriculum vitae

Personendaten

Vorname	Benedikt
Nachname	Daum
Geburtsdatum	06.10.1980
Geburtsort	Innsbruck
Staatsbürgerschaft	Österreich
Anschrift	Oberbach 7/3, A-6671 Weißenbach am Lech, Österreich

Beruflicher Werdegang

seit 05.2022	Berechnungsingenieur Plansee SE
05.2016-04.2022	Leiter der Forschungsgruppe Materialmodellierung am Institut für Statik und Dynamik der Leibniz Universität Hannover
02.2011-10.2015	Wissenschaftlicher Mitarbeiter und Doktorand am Institut für Leichtbau und Strukturbiomechanik der TU Wien
09.2001-02.2005	Konstrukteur Johann Rathgeber GmbH, Innsbruck
11.2000-06.2001	Grundwehrdienst

Ausbildung

02.2011-08.2015	Doktoratsstudium Technische Universität Wien
02.2005-10.2010	Diplomstudium Maschinenbau Technische Universität Graz
09.1995-06.2000	Oberstufe, Abschluss mit Matura (entspricht Abitur) HTL Innsbruck (berufsbildende höhere Schule)